THE ‘4D-EARTH-SWARM’ PROJECT:
RAPID GEOMAGNETIC FIELD CHANGES FROM SWARM

SCIENTIFIC REPORT
FINAL VERSION

a project supported by ESA

February 2022

list of partners:

- ISTerre, Grenoble, France (PI)
- ETH Zurich, Switzerland
- Univ. of Leeds, UK
- IPG Paris, France
- DTU Space, Copenhagen, Denmark

Contents

1 Scientific Requirement Consolidation (R-A.1) 1

A. Jackson[1], N. Gillet[2], J. Aubert[3], C. Finlay[4], D. Jault[2], P. Livermore[5], J. Noir[1] and N. Olsen[4]

[1] ETH Zurich, [2] ISTerre, [3] IPG Paris, [4] DTU Space, [5] University of Leeds

C. C. Finlay and M. D. Hammer

DTU Space, Technical University of Denmark

J. Aubert

IPG Paris

J. Aubert

IPG Paris

CHAPTER 1

Review of the state of the art in interannual core dynamics

4DEarth_Swarm_Core ESA project deliverable R-A.1

A. JACKSON[1], N. GILLET[2], J. AUBERT[3], C. FINLAY[4], D. JAULT[2], P. LIVERMORE[5], J. NOIR[1] AND N. OLSEN[4]
[1] ETH ZURICH, [2] ISTERRE, [3] IPG PARIS, [4] DTU SPACE, [5] UNIVERSITY OF LEEDS

1.1 Context of the 4D-Earth-Swarm activities

Our activities are broadly characterised by one scientific question, namely the physical modeling of rapid secular variation (SV, or rate of change of the magnetic field) changes. These are inter-annual changes with time scales of two years to several decades. The question will be tackled using several angles of investigation, including:

- the modeling of geomagnetic data by means of reduced stochastic models of the core surface dynamics, based on satellite observations through (stochastic) data assimilation algorithms;
- the physical modeling of such SV changes through reduced quasi-geostrophic (QG) models that describe the dynamics of axially invariant motions in the core in the presence of magnetic field;
- the comparison of SV changes observed through satellite (Swarm and others) data with outputs from three-dimensional computations.

These are further described in the sections below.

1.2 Background

Swarm data hold the prospect of illuminating interior properties of the core, such as the strength and distribution of magnetic fields and, potentially, the strength of buoyancy forces. The observed spatio-temporal changes can be related to a model of the electrically conducting core's interior dynamics, provided that a predictive dynamical model of those dynamics is available. However, only in very special circumstances is such a deterministic model already available. It is the case for torsional oscillations (namely the oscillations of cylinders of fluid coaxial with the rotation axis, where the restoring force is entirely magnetic), used by Gillet et al (2010) to determine one property of the interior magnetic field from interannual changes in the fluid flow over the last few decades. In no other case is a dynamical model available for the study of the rapid (i.e. decadal and shorter) geomagnetic field changes. The exploration of suitable strategies for the creation of a model applicable to Swarm data is one of the aims of the present proposal. The accepted state of the art for combining observations with a dynamical model is termed data assimilation (DA). At present there are two flavours of DA which are available to the geomagnetic community: probabilistic (here sequential) assimilation (SDA) and variational assimilation (VDA). The sequential approach in the context of primitive magneto-hydro-dynamic equations has been pioneered by A. Fournier & J. Aubert and colleagues at IPGP and W. Kuang & A. Tangborn at NASA. More and more groups are adopting this approach, including groups in Germany and Japan.

Recently, SDA was also considered to tackle questions posed by satellite observations by means of two pragmatic approaches: either through no-cast re-analyses (i.e. no time-stepping of the deterministic model) using three-dimensional geodynamo model cross-covariances (Aubert, 2015), or by considering instead a stochastic forecast model anchored to geodynamo spatial covariances and compatible with the occurrence of geomagnetic jerks (Barrois et al, 2017).

The variational approach has been applied to simplified problems by Li et al (2014). In principle, the mechanics of this approach are in hand, but there is a need to develop a suitable model to which this approach could be applied that does not suffer from the effects of overly-large viscosity. The idea for a variational approach was also set out in Canet et al (2009) and applied to the problem of torsional oscillations.

A number of potential avenues are open for the development of a new dynamical model. We believe that there are close parallels with similar problems in oceanography, whose community has worked for many years to develop models in which the effect of viscosity is not overbearing.

We mention promising avenues: Canet et al (2009) and Labbé et al (2015) have developed a QG model of core dynamics that holds the promise of development into a suitable dynamical model for assimilation. While most of the terms in the Navier-Stokes equation can be elegantly handled by these approaches, neither of the models are able to properly treat the magnetic terms in a rigorous manner. This family of approaches will be stepping-off points in our quest to develop a suitable dynamical core for assimilation.

In the following sections we discuss the pertinent observations and techniques that have been developed by the community, what they tell us, and what is the state of play.

1.3 Origin and observability of interannual motions observed

A consensus view of the 4D Earth team is that it is a regrettable situation that the 6 year torsional oscillations have only been observed by one team, namely the original discoverers (Gillet et al, 2010). Despite the strong evidence from the predicted length-of-day (LOD) changes that correspond well to the observed changes (Gillet et al, 2015), there is a need for an independent corroboration of these motions (even though the above observation has been confirmed with several rather distinct algorithms, see Gillet et al, 2019). This was never proposed as part of the WPs of the present proposal, but, considering the importance of the observation for core dynamics, it is to be hoped that a scientific team will take up the challenge. A key ingredient in the isolation of torsional oscillations at interannual periods by the Grenoble group is the inclusion of unmodelled SV sources associated with time-correlated subgrid processes. We believe any attempt at reproducing this result should involve this mechanism, in order to avoid either losing information by under-fitting SV data, or generating severely biased core flow models by over-fitting them.

The strongest repeating signal in LOD series is at 6 years (Abarca Del Rio et al, 2000; Chao et al, 2014; Holme and De Viron, 2013). Filtered around this period, core flow models inverted from SV models show an outward propagation of zonal motions. When interpreted as torsional Alfvén waves (Braginsky, 1970), the recovered wave form raises several geophysical issues. First the absence of noticeable reflexion at the equator may be interpreted in term of a relatively weak conductance of the lower mantle (of the order of $3\,10^7$ S), in a scenario where the core-mantle coupling is operated through an electro-magnetic stress (Schaeffer and Jault, 2016). However, there is still the possibility for a topographic torque to be responsible for the associated LOD changes (see §1.9).

Second, the propagation from the inner core (at least during the 1960-70's) has been first interpreted through a torque involving the inner core. This latter may be associated with Lorentz forces on the vicinity of the tangent cylinder (Teed et al, 2015), as it is the case in dynamo simulations (Schaeffer et al, 2017). Alternatively, it may involve a gravitational coupling between the inner core and the mantle (Mound and Buffett, 2006), although this scenario itself is debated (Davies et al, 2014; Chao, 2017). The possibility of an excitation induced by magnetospheric field changes has been proposed (Legaut, 2005), but there may not be enough energy there to excite torsional Alfvén waves (by definition equi-partitioned in kinetic and magnetic energies) with the observed amplitude. Finally, one cannot rule out the possibility of a forcing spread throughout the fluid core, as we have only access to the gravest of the torsional modes (Gillet et al, 2017). The question whether the better spatio-temporal resolution offered by Swarm data will give or not access to higher harmonics is open.

Regardless, one should keep in mind that the above zonal flows only represent a tiny contribution to interannual motions (Gillet et al, 2015; Kloss and Finlay, 2019), and that we still miss a conclusive interpretation of the more energetic non-zonal motions (see also §1.6). We also stress the limited access to interannual field changes, which are constrained by observations only for the largest length-scales in geomagnetic field models (Gillet, 2019).

1.4 Basic mechanisms for core-mantle coupling, and settled questions

Core-mantle coupling plays an important part in the time evolution of the LOD, with periods above 2 years, and in the dissipation of the annual retrograde nutation of the Earth's rotation axis. Changes of axial core angular momentum are estimated from models of the geostrophic motions in the Earth's fluid core and changes of axial mantle angular momentum are directly inferred from LOD observations. There is reasonable evidence that variations in the core and mantle axial angular momentum compensate although uncertainties remain significant (Gillet et al, 2015; Bärenzung et al, 2018). Curiously, the agreement appears less good during the satellite era, from $\approx$ 2003 onward (Gillet et al, 2019). The core-mantle coupling mechanism responsible for the exchanges of angular momentum between the fluid core and the solid mantle is still debated.

The most widely studied coupling mechanisms between core and mantle are viscous, gravitational, topographic and electromagnetic (EM). Unfortunately they all depend on poorly known properties of the lowermost mantle and core, respectively the effective core viscosity, geometry of the gravity equipotential surface next to the core-mantle boundary, topography of the core-mantle interface and the electrical conductivity of the lowermost mantle (Roberts and Aurnou, 2011). Of these, we briefly review EM coupling below as this is most relevant to the 4D-Earth-Swarm proposal.

Studies of EM sounding from Earth's surface based on external magnetic field fluctuations have poor sensitivity to the lowermost mantle, although typical values are 10 S/m (Constable, 2007). Yet due to inhomogeneities on the core-mantle boundary, these values may not be indicative of the conductivity at the interface itself. The difficulty in determining conductivity is further compounded by the fact that EM coupling mechanisms generally depend on conductance, the integrated conductivity over a layer (whose thickness is unknown), rather than the conductivity itself.

Independently, through respectively models of EM coupling and consideration of nutations, both Holme (1998) and Buffett et al (2002) propose a conductance of 10^8 S. One possibility is this is caused by a thin layer (of about 200 m) of material with the same conductivity of the core. The occurrence of a solid metallic layer at the lowermost mantle pressure and temperature is problematic and the mechanism of nutation dissipation remains an open question (Buffett, 2010). Even if the conducting materials are distributed over a thicker region, it is difficult to avoid a layer of relatively conductive material on the core-mantle boundary (CMB) interface as on treating the majority of the lowermost mantle as a single layer of depth 1000 km would yield a conductance of 10^7 S, inconsistent with other estimates. However, this reasoning does not hold if other mechanisms participate in the coupling of the core with the mantle as the required EM torque would be lower.

Another line of investigation comes from jointly considering dynamics in the core interior and interactions with the mantle. For example, torsional waves, which propagate as Alfv́en waves in the Earth's core, have periods about 6 years. Their reflection upon arrival at the core equator depends on the electrical conductance of the lowermost mantle (Schaeffer and Jault, 2016). They are completely absorbed for a mantle conductance of $1.6 \pm 0.3 \times 10^8$ S (error bar arising from uncertainties on the intensity of the radial magnetic field at the core equator). The apparently weak reflection of the waves leads to estimates of total mantle conductance in the range $3 \times 10^7 - -3 \times 10^8$S. All the above estimates offer consistent values of the conductance of about 10^8 S, although the actual electrical conductivity at the CMB is not well constrained.

Most dynamo simulations do not include magnetic core-mantle coupling. The recent geodynamo study of Aubert and Finlay (2019) dedicated to the rapid dynamics of the Earth's core however does include a thin mantle layer of conductance of about 2×10^8 S, *i.e.* comparable to the above values.

1.5 How good is the quasi-geostrophic assumption?

In rotating fluid dynamics, a geostrophic equilibrium is a balance between Coriolis and pressure forces. The only truly geostrophic motions in a rotating spherical shell are zonal (axisymmetric azimuthal) flows with axial invariance. All other flows (including convective poloidal motions) rather obey a degenerate form of geostrophy which is known as quasi-geostrophy (QG) at the condition that the first-order forces driving those flows are much weaker than the leading-order pressure and Coriolis forces. Because of the Taylor-Proudman theorem, QG flows generally acquire a quasi-invariant structure along the rotation axis when the first-order forces are sufficiently weak, leading to the possibility to formulate their dynamics in framework of reduced dimensionality (e.g. Gillet and Jones, 2006; Labbé et al, 2015; Calkins, 2018). This in turn enables important computer cost savings when performing numerical simulations, and the possibility to reach strongly turbulent regime that are appropriate for planetary cores (e.g. Gastine, 2019). QG has proven to be an efficient way to describe rapidly-rotating thermal convection (e.g. Gillet and Jones, 2006). In this non-magnetic case, the results compare favourably with three-dimensional reference models and laboratory experiments, particularly concerning the scaling behaviour in turbulent conditions (Aubert et al, 2003; Gastine et al, 2016; Guervilly et al, 2019) because the first-order buoyancy and inertial forces remain sufficiently subdominant relative to the leading-order QG equilibrium.

Systematic surveys of three-dimensional numerical dynamos (Schwaiger et al, 2019) performed over a wide range of the accessible parameter space (including conditions approaching those of the Earth's core, Aubert et al, 2017) have confirmed the existence of a leading-order QG equilibrium even in the presence of a self-sustained magnetic field. Magnetostrophy, where the magnetic force can reach leading order and balance the Coriolis and pressure forces, is never observed at system scale (because the system needs buoyant driving) and is usually deferred to scales of about 100 km, but can approach larger scales in selected regions of the parameter space where the convective forcing is low (Dormy, 2016; Schwaiger et al, 2019). In all simulations, the occurrence of local magnetostrophy corresponds to the Lorentz force being reduced to a magnetic pressure gradient without a dynamical influence, meaning that from a dynamical standpoint QG in fact holds at all scales. In the numerical dynamos, the first-order force balance coming after QG is between the Lorentz, buoyancy forces and the ageostrophic part of the Coriolis force. This balance is known as the MAC balance and the total (leading plus first) order force balance is referred to as the QG-MAC balance. The first-order MAC balance is additionally scale-dependent. At scales larger than about 1000 km the first-order balance is mainly of thermal wind nature (balance between the ageostrophic Coriolis and buoyancy forces), with the magnetic force being subdominant. The scale-dependence of the force balance can also be viewed as a frequency-domain dependence, where time scales longer than the secular overturn are mainly governed by thermal wind dynamics and the role of magnetic forces is deferred to faster, interannual to decadal dynamics (Schaeffer et al, 2017; Aubert, 2018). This corresponds to a minimisation of the interaction between the magnetic field and the flow if sufficient time is allowed for the moderating effects of Lenz' law to take place.

Unlike non-magnetic rotating convective systems, numerical dynamos frequently feature a first-order MAC balance less than an order of magnitude below the leading-order QG equilibrium (Schwaiger et al, 2019). Because of this, the slowly-varying (secular) flows can show departures from QG and axial invariance, and need to be removed in order to exhibit structures closer to QG that can be modelled as such in two space dimensions. Of particular importance are magneto-inertial waves such as interannual Alfvén waves, which have been observed in numerical simulations at the axisymmetric (e.g. Schaeffer et al, 2017) and non-axisymmetric (Aubert, 2018) levels. These latter QG, axially invariant, non-axisymmetric waves have been related to the occurrence of geomagnetic jerks (Aubert and Finlay, 2019), underlining the relevance of a QG framework to describe the geomagnetic signal at interannual time scales. The main difficulty is that the waves ride on a three-dimensional, strongly heterogeneous, slowly evolving thermal and magnetic background state that cannot readily be described within a QG framework, as stated above. This rationalises the general difficulty encountered by the community in obtaining working self-sustained dynamos that are purely QG, while more success has been obtained by studies where QG flows are produced within an imposed, rather than self-sustained, magnetic field (e.g. Labbé et al, 2015; More and Dumberry, 2017)

In summary, QG is a numerically efficient and easy to implement approximation, that has potential to describe some of the interannual core dynamics. The insight from current three-dimensional numerical dynamos however suggests that in the presence of a self-sustained magnetic field, a QG description of core dynamics most likely fails to describe the slowly-varying, buoyancy-driven secular evolution of the core that generates the field. The way to progress may therefore consist in an estimation of a three-dimensional background state (thermal, magnetic, kinematic) for the core at present (during the Swarm era), over which a QG model may be built to describe the rapidly-evolving part of the geomagnetic signal as an induced perturbation of an imposed background field.

1.6 Stochastic models anchored to geodynamo spatial covariances

There is currently a debate concerning the existence of a specific signal at 6 yr in the magnetic field. On the one hand, secular acceleration (SA) pulses, or maxima in the SA norm, seem to occur every 3 yrs (e.g. Finlay et al, 2016). This may either result from a SV signal specific to the 6 yr period (e.g. Soloviev et al, 2017), or be the consequence of the filtering in space and time when building global models (Gillet, 2019). The existence of jerks events isolated in time is particularly intriguing since we are aware of no other geophysical system displaying such a behavior. Alternatively, SA pulses could result from the spectral index $\alpha \simeq -2$ found for the temporal spectrum of SV Gauss coefficients at decadal to annual time-scales, $S(f) \propto f^{\alpha}$ (Lesur et al, 2017).

In this context, one expects the SA temporal spectrum to be flat from annual to decadal periods. The framework of stochastic processes has thus been considered for the integration of magnetic field evolution into SDA tools that only model the core surface dynamics, still incorporating geodynamo constraints by means of spatial and temporal cross-covariances (Barrois et al, 2017; Gillet et al, 2019). This approach presents the advantage of reducing considerably the dimension of the model state w.r.t. geodynamo driven DA algorithms (e.g. Fournier et al, 2013; Sanchez et al, 2019). It also extends down to annual periods the range of frequencies where the -2 spectral index operates (extreme 3D simulations, once scaled to geophysical units, lose this property at about 30 yr periods (Aubert, 2018), i.e. outside the very period range of interest for this proposal). The main current limitation of stochastic models is their inability to directly relate the observed SV changes to dynamical properties deep in the fluid core (though its products can be used as a constraint for subsequent dynamical analysis).

1.7 The role of buoyancy and of Lorentz forces

In geodynamo simulations run at high rotation rates (Schaeffer et al, 2017; Aubert et al, 2017), Lorentz forces appear to play a relatively minor role at large length-scales, and this despite a large magnetic field intensity (as measured by Elsasser numbers of order unity). Magnetic and velocity fields seem to self-organize so as to minimize induction as much as possible. The magnetostrophic equilibrium (where both Lorentz and Coriolis forces balance the pressure gradient) is thus expelled towards small length-scales (Aurnou and King, 2017), while geostrophy applies at the largest length-scale, at which departures from geostrophy are buoyancy-driven. If this scenario applies in the Earth's core, models based on magnetostrophy (see Hardy et al, 2018) might miss a crucial ingredient in order to model decadal field changes – one may think here in particular of QG models based on quadratic quantities of the magnetic field (see Jault and Finlay, 2015).

Numerical dynamos along the path are nevertheless run at parameters different from Earth-like, involving parameterizations of some nonlinear subgrid processes (Aubert et al, 2017). With lower values of the magnetic Prandtl number P_m (ratio of viscous to magnetic diffusivities), the larger magnetic diffusion may tend to enlarge the range of wave-numbers where magnetostrophy prevails. This issue is particularly important on the vicinity of the tangent cylinder. In this singular area of the core, simulations show intense magnetic fields in link with strong polar vortices (Schaeffer et al, 2017)

1.8 The prospects and applicability of the quasi-geostrophic hypothesis

We have seen in previous sections that the idea of quasi-geostrophy is attractive, as it captures much of the required physics. In the hydrodynamical case, where there are no magnetic forces, the approach can be readily used to model buoyancy-driven flows, to great effect (Guervilly et al, 2019). Presently what is missing is a theory that is able to handle the Lorentz forces that arise in the presence of magnetic fields.

A first attempt at the problem was made by Canet et al (2009). The approach to project the dynamical equations onto the equatorial plane involves an integration along the rotation axis from the lower to the upper boundary. This integration leads to boundary terms that are, unlike all other quantities, controlled by values of electrical currents that are not describable on the equatorial plane. It was initially envisaged that these boundary terms would be much smaller than the volumetrically averaged terms and thus could be neglected (Canet et al, 2009). Subsequent work by Maffei (2016), amongst others, showed the difficulties that this leads to: when one considers the normal mode problem of small oscillations around a background state, one finds that the surface terms are non-negligible, particularly close to the equator. This leads to an incorrectly-posed eigenvalue problem.

Recognising this issue, Labbé et al (2015) pioneered a new approach. They showed that if the magnetic field could be written in the same form as the QG velocity field, then the projection of all quantities onto the equatorial plane could be achieved. This is a great step forward. It comes at a price however. The system treated means that the field lines of the magnetic field close within the fluid, and no field emanates from the core. In some ways this is similar to the treatment of Canet et al (2009). More worrying is the likelihood that a magnetic field in the core can really be represented in this QG form. The QG form for the velocity field is well motivated, relying, as it does, on the underpinnings provided by the Proudman-Taylor theorem, which leads naturally to first-order geostrophy. There is no such theorem that suggest that the QG form can be used for the magnetic field. Thus one must wonder to what extent the results will depend on this assumption.

To summarise, there is no presently acceptable magnetohydrodynamical QG formulation, and it remains a challenge for the future to develop one. The attractiveness of the approach, if a self-consistent one can be found, lies in its use for the purposes of data assimilation.

The data assimilation problem is the following. One has high quality maps of the magnetic field at the core-mantle boundary for the last decades and centuries that have been created from measurements taken at the Earth's surface and above. These will subsequently be termed *observations*, despite the fact that the maps are actually derived quantities. The quest is to find a dynamical model of motions in the core (and their time variations) that can account for the observations. The problem requires a *dynamical core*, namely a version of the fluid mechanics in the core. With these two ingredients, the matching process can begin. The outcome of the matching process is twofold. In principle one can deduce properties of the core such as the time-dependent buoyancy field and the interior magnetic field strength and geometry. These quantities are such that they lead to a dynamical evolution in time of core quantities, such that the observations are honoured. But in addition, the time-evolution can be followed forwards beyond the time window of the observations, into a prediction. This comes naturally, for free.

The attractiveness of the QG approach as a version of the fluid mechanics is twofold. Firstly it can operate in regimes that three dimensional dynamo models cannot reach. In particular, it is able to reduce the effects of viscosity to levels that are close to those expected within the core (Guervilly et al, 2019). More important considerations, however, are probably associated with the inverse problem that is being solved. Quite likely it is only possible to recover some forms of "lumped parameters", rather than full 3-D information. Thus one may have to be satisfied with field strengths and geometries reduced by averaging, rather than full recovery of 3-D toroidal and poloidal magnetic fields. Put simply, 2-D observations in time (observations on the core-mantle boundary) are unlikely to be able to recover 3-D fields. These 2D fields may well be able to recover 2-D fields as a function of time. Thus the pure counting problem argues in favour of a theory like quasi-geostrophy. The problem was highlighted by Li et al (2014).

It should be said that there has been considerable success by using 3D dynamo models as dynamical cores for Ensemble Kalman filter schemes. However, these calculations have not been able to constrain the interior buoyancy and magnetic fields in the core.

It is our hope that the present 4DEarth activity might lead to further insights and experiences that will lay the path for future data assimilation activities.

1.9 Topographic torques on a non-spherical core

So far there is no certainty in the mechanism that transfers core's angular momentum to the solid mantle. Proposed mechanisms include electromagnetic coupling via electrically conducting lower mantle (see section 1.4 for more details), gravitational coupling via a gravitational torque between a deformed inner core and the mantle (Buffett, 1996a,b), or topographic coupling through a non-axisymmetric CMB.

For a spherical CMB the pressure torque on the mantle by any flow in the core vanishes exactly by definition. More precisely, for any CMB symmetric about the rotation axis, no changes in the LOD may be explained by the pressure torque. Investigating core flows in non-axisymmetric domains is challenging and has been limited to a few studies up until today (e.g. Kuang and Chao, 2001; Jault and Finlay, 2015; Vidal et al, 2019).

Torsional waves, with periods on the scale of a few years, have been proposed to be responsible for such changes in the LOD. Their periods have been used to infer the mean radial magnetic field strength in the core, a quantity otherwise inaccessible to observations (Gillet et al, 2010). In a sphere, the flow of these waves follow contours of constant column height. To investigate the flow structure of these waves for a non-axisymmetric domain and wether or not this flow is capable of exerting a pressure torque onto the solid boundary is the goal of this task. We aim to use a Cartesian monomial approach in the ellipsoid (Vidal et al, 2019) and curvilinear coordinates for any geometry beyond the ellipsoid.

It is unknown how important domains without closed geostrophic contours are for the topographic torque. Such domains are certainly present in the Earth's core. Understanding the influence of topography on the flow structure and periods of torsional waves is crucial to verify their robustness in predicting core quantities in any planetary or stellar core.

1.10 Conclusions

There have been spectacular achievements in core studies over the last decade. Not least is the observation of torsional oscillations. We have alluded to some of the open issues in preceding sections. Although much is understood, it has proven difficult to deduce concrete properties of the Earth. Tables 1 and 2 summarise the state of play on the most important issues.

State of the art on lower mantle electrical conductivity σ
From observed lack of reflected torsional oscillations: Only bounds are on conductance $G = \sigma H$, where H is the depth of the conducting region. Constraint is on $Q = \sqrt{\frac{\mu_0}{\rho}} G B_r\vert_{z=0} \approx 10^{-5} G B_r\vert_{z=0} \ (SI)$ where $G = \int_{r_0}^{r_0+H} \sigma \, dr \approx \sigma H$. $Q \simeq 1$ is preferred.
Pros: This is the strongest constraint on conductance.
Cons: Need definitive bounds on reflection coefficient/reflected energy. Need bounds on radial field B_r at $z = 0$. Provides information on only one region of CMB, at the equator. Most of CMB entirely unconstrained. Conductance not required to be laterally homogeneous, could have isolated blobs. Theory for laterally heterogeneous conductance yet to be worked out.

Table 1.1: State of the art on lower mantle electrical conductivity σ at the base of the mantle.

State of the art on interior field strength
Gillet et al (2010,2015) provide a lower bound of 2-3mT in the cylindrically radial magnetic field strength. The profile of B_s shows weakening towards the CMB.
Pros: Almost exactly predicts the filtered length-of-day in the 5-8 year period range.
Cons: Has never been replicated.

Table 1.2: State of the art on interior field strength in the Earth's core.

Bibliography

Abarca Del Rio R, Gambis D, Salstein D (2000) Interannual signals in length of day and atmospheric angular momentum. In: Annales Geophysicae, Springer, vol 18(3), pp 347–364

Aubert J (2015) Geomagnetic forecasts driven by thermal wind dynamics in the Earth's core. Geophys J Int 203(3):1738–1751

Aubert J (2018) Geomagnetic acceleration and rapid hydromagnetic wave dynamics in advanced numerical simulations of the geodynamo. Geophys J Int 214(1):531–547

Aubert J, Finlay CC (2019) Geomagnetic jerks and rapid hydromagnetic waves focusing at Earth's core surface. Nature Geosci 12(5):393–398, DOI 10.1038/s41561-019-0355-1

Aubert J, Gillet N, Cardin P (2003) Quasigeostrophic models of convection in rotating spherical shells. Geophys Geochem Geosystems 4

Aubert J, Gastine T, Fournier A (2017) Spherical convective dynamos in the rapidly rotating asymptotic regime. J Fluid Mech 813:558–593

Aurnou J, King E (2017) The cross-over to magnetostrophic convection in planetary dynamo systems. Proceedings of the Royal Society A: Mathematical, Physical and Engineering Sciences 473(2199):20160,731

Bärenzung J, Holschneider M, Wicht J, Sanchez S, Lesur V (2018) Modeling and predicting the short-term evolution of the geomagnetic field. Journal of Geophysical Research: Solid Earth 123(6):4539–4560

Barrois O, Gillet N, Aubert J (2017) Contributions to the geomagnetic secular variation from a reanalysis of core surface dynamics. Geophys J Int 211(1):50–68

Braginsky S (1970) Torsional magnetohydrodynamics vibrations in the earth's core and variations in day length. Geomagn Aeron 10:3–12

Buffett BA (1996a) Gravitational oscillations in the length of day. Geophysical Research Letters 23(17):2279–2282, DOI 10.1029/96GL02083

Buffett BA (1996b) A mechanism for decade fluctuations in the length of day. Geophysical Research Letters 23(25):3803–3806, DOI 10.1029/96GL03571

Buffett BA (2010) Chemical stratification at the top of earth's core: Constraints from observations of nutations. Earth and Planetary Science Letters 296(3-4):367–372

Buffett BA, Mathews PA, Herring TA (2002) Modelling of nutation and precession: Effects of electromagnetic coupling. J Geophys Res 107(B4):5.1–5.15

Calkins MA (2018) Quasi-geostrophic dynamo theory. Phys Earth Planet Int 276:182 – 189

Canet E, Fournier A, Jault D (2009) Forward and adjoint quasi-geostrophic models of the geomagnetic secular variation. J Geophys Res: Solid Earth 114(B11)

Chao B (2017) Dynamics of axial torsional libration under the mantle-inner core gravitational interaction. Journal of Geophysical Research: Solid Earth 122(1):560–571

Chao BF, Chung W, Shih Z, Hsieh Y (2014) Earth's rotation variations: a wavelet analysis. Terra Nova 26(4):260–264

Constable S (2007) Geomagnetism. Treatise on Geophysics, ed Schubert, G, Elsevier

Davies CJ, Stegman DR, Dumberry M (2014) The strength of gravitational core-mantle coupling. Geophysical Research Letters 41(11):3786–3792

Dormy E (2016) Strong-field spherical dynamos. J Fluid Mech 789:500–513

Finlay CC, Olsen N, Kotsiaros S, Gillet N, Tøffner-Clausen L (2016) Recent geomagnetic secular variation from Swarm. Earth, Planets and Space 68(1):1–18

Fournier A, Nerger L, Aubert J (2013) An ensemble Kalman filter for the time-dependent analysis of the geomagnetic field. Geochem geophys geosyst 14(10):4035–4043

Gastine T (2019) pizza: an open-source pseudo-spectral code for spherical quasi-geostrophic convection. Geophysical Journal International 217(3):1558–1576, DOI 10.1093/gji/ggz103, URL `https://doi.org/10.1093/gji/ggz103`, `http://oup.prod.sis.lan/gji/article-pdf/217/3/1558/28225303/ggz103.pdf`

Gastine T, Wicht J, Aubert J (2016) Scaling regimes in spherical shell rotating convection. J Fluid Mech 808:690–732, DOI 10.1017/jfm.2016.659

Gillet N (2019) Spatial And Temporal Changes Of The Geomagnetic Field: Insights From Forward And Inverse Core Field Models. In: Geomagnetism, aeronomy and space weather: a journey from the Earth's core to the sun, URL `https://hal.archives-ouvertes.fr/hal-02042703`

Gillet N, Jones CA (2006) The quasi-geostrophic model for rapidly rotating spherical convection outside the tangent cylinder. J Fluid Mech 554:343–369

Gillet N, Jault D, Canet E, Fournier A (2010) Fast torsional waves and strong magnetic field within the Earth's core. Nature 465(7294):74

Gillet N, Jault D, Finlay C (2015) Planetary gyre, time-dependent eddies, torsional waves, and equatorial jets at the earth's core surface. Journal of Geophysical Research: Solid Earth 120(6):3991–4013

Gillet N, Jault D, Canet E (2017) Excitation of travelling torsional normal modes in an earth's core model. Geophysical Journal International 210(3):1503–1516

Gillet N, Huder L, Aubert J (2019) A reduced stochastic model of core surface dynamics based on geodynamo simulations. Geophys J Int 219(1):522–539

Guervilly C, Cardin P, Schaeffer N (2019) Turbulent convective length scale in planetary cores. Nature 570(7761):368–371

Hardy CM, Livermore PW, Niesen J, Luo J, Li K (2018) Determination of the instantaneous geostrophic flow within the three-dimensional magnetostrophic regime. Proceedings of the Royal Society A: Mathematical, Physical and Engineering Sciences 474(2218):20180,412

Holme R (1998) Electromagnetic core-mantle coupling ii: probing deep mantle conductance. The core-mantle boundary region 28:139–151

Holme R, De Viron O (2013) Characterization and implications of intradecadal variations in length of day. Nature 499(7457):202

Jault D, Finlay CC (2015) Waves in the core and mechanical core-mantle interactions. In: Schubert G, Olson P (eds) Treatise on Geophysics, Core Dynamics, 2nd edition, vol 8, Elsevier, Oxford, chap 8.09, pp 225–244

Kloss C, Finlay CC (2019) Time-dependent low-latitude core flow and geomagnetic field acceleration pulses. Geophysical Journal International 217(1):140–168

Kuang W, Chao BF (2001) Topographic core-mantle coupling in geodynamo modeling. Geophysical research letters 28(9):1871–1874

Labbé F, Jault D, Gillet N (2015) On magnetostrophic inertia-less waves in quasi-geostrophic models of planetary cores. Geophys Astrophys Fluid Dyn 109(6):587–610

Legaut G (2005) Ondes de torsion dans le noyau terrestre. PhD thesis, Univ. Joseph Fourier

Lesur V, Wardinski I, Baerenzung J, Holschneider M (2017) On the frequency spectra of the core magnetic field Gauss coefficients. Phys Earth Planet Int

Li K, Jackson A, Livermore PW (2014) Variational data assimilation for a forced, inertia-free magnetohydrodynamic dynamo model. Geophysical Journal International 199(3):1662–1676

Maffei S (2016) Quasi-geostrophic models for fast dynamics in the earth's outer core. PhD thesis, ETH Zurich

More C, Dumberry M (2017) Convectively driven decadal zonal accelerations in Earth's fluid core. Geophysical Journal International 213(1):434–446

Mound JE, Buffett BA (2006) Detection of a gravitational oscillation in length-of-day. Earth and Planetary Science Letters 243(3-4):383–389

Roberts PH, Aurnou J (2011) On the theory of core-mantle coupling. Geophys Astrophys Fl Dyn 106(2):157–230

Sanchez S, Wicht J, Bärenzung J, Holschneider M (2019) Sequential assimilation of geomagnetic observations: perspectives for the reconstruction and prediction of core dynamics. Geophysical Journal International 217(2):1434–1450

Schaeffer N, Jault D (2016) Electrical conductivity of the lowermost mantle explains absorption of core torsional waves at the equator. Geophysical Research Letters 43(10):4922–4928

Schaeffer N, Jault D, Nataf HC, Fournier A (2017) Turbulent geodynamo simulations: a leap towards Earth's core. Geophys J Int 211(1):1–29

Schwaiger T, Gastine T, Aubert J (2019) Force balance in numerical geodynamo simulations: a systematic study. Geophys J Int 219(S1):S101–S114

Soloviev A, Chulliat A, Bogoutdinov S (2017) Detection of secular acceleration pulses from magnetic observatory data. Physics of the Earth and Planetary Interiors 270:128–142

Teed RJ, Jones CA, Tobias SM (2015) The transition to earth-like torsional oscillations in magnetoconvection simulations. Earth and Planetary Science Letters 419:22–31

Vidal J, Cébron D, ud Doula A, Alecian E (2019) Fossil field decay due to nonlinear tides in massive binaries. Astronomy & Astrophysics 629:A142, DOI 10.1051/0004-6361/201935658

CHAPTER 2

Descriptions of the datasets

2.1 Geomagnetic Datasets

4DEarth_Swarm_Core ESA project deliverable D-B.1

C. C. Finlay and M. D. Hammer
DTU Space, Technical University of Denmark

2.1.1 Introduction

This report provides information on geomagnetic datasets and derivatives (including geomagnetic field models) produced by DTU for the Swarm+ 4D Deep Earth: Core project, as part of Task B and Work Package 1, and designed to be used for studies on core dynamics.

2.1.2 Geomagnetic Virtual Observatory datasets

Geomagnetic Virtual Observatory (GVO) datasets have been produced in a consistent fashion from the satellite missions CHAMP, Cryosat-2 and *Swarm*. In each case the same algorithm, recently developed in the context of the *Swarm* mission (Hammer et al, 2020a) was been employed.

Each GVO dataset involves time series of the vector magnetic field on a regular grid at satellite altitude. They were constructed by fitting a local potential to the data falling within cylinders centered on each target location (Mandea and Olsen, 2006; Olsen and Mandea, 2007). The geographical locations of the GVOs and associated cylinders (radius 700 km) used to construct the GVO datasets delivered here are shown in Fig. 2.1. This grid was generated using a recursive zonal approximate equal area partitioning algorithm (Leopardi, 2006).

Detailed tests of the GVO algorithm have recently been carried out in the context of the *Swarm* mission (Hammer et al, 2020a,b,d). Here we go further and apply the same data selection and processing procedure to data from the earlier CHAMP mission (Reigber et al, 2005) and the Cryosat-2 mission, where calibrated platform magnetometer data has recently become available (Olsen et al, 2020). Below we give a brief summary of the GVO processing algorithm, full details are given in the *Swarm* GVO product description of algorithm document (Hammer et al, 2020b).

GVO series are provided at 1 month and 4 month cadences. In each case estimates are provided for both the observed field (including all data sources) and the core field. 1 monthly GVOs are derived from 15 sec samples of *Swarm* L1b MAG-L data, from all three satellites, and 15 sec samples of L3 CHAMP data. 4 monthly GVOs are derived from 15 sec samples of *Swarm* L1b MAG-L data, 15

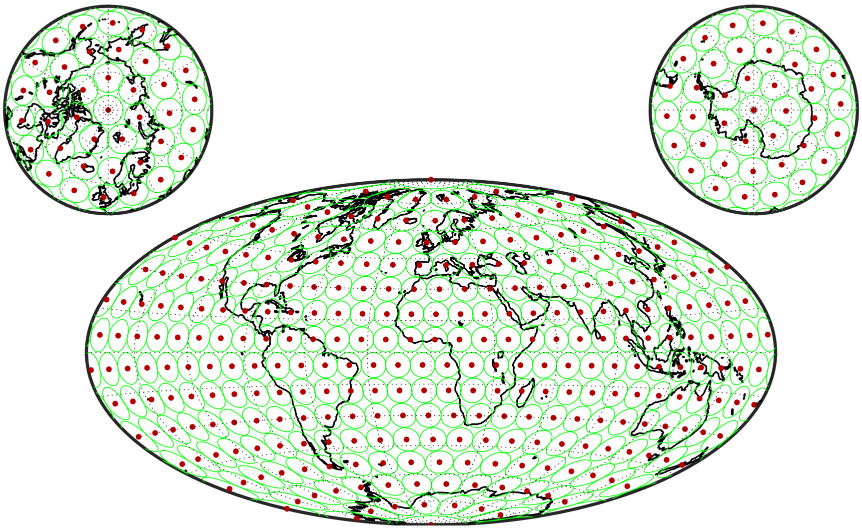

Figure 2.1: Geomagnetic Virtual Observatory (GVO) locations (red dots) along with associated regions where satellite data is collected (green circles). 300 locations in all, arranged in an approximately equal area grid.

sec samples of L3 CHAMP data, and 1 minute means of Cryosat-2 data, that satisfy the following dark and geomagnetically quiet time criteria:

- The sun is at least 10° below horizon
- Geomagnetic activity index $K_p < 3^\circ$
- Time change of Ring current (RC) index $|dRC/dt| < 3\text{nT/hr}^{-1}$, Olsen et al (2014)
- Merging electric field at the magnetopause $E_m < 0.8\text{mVm}^{-1}$, Olsen et al (2014)
- Interplanetary Magnetic Field (IMF) $B_z > 0\,\text{nT}$ and $|B_y| < 10\,\text{nT}$

where the latter two conditions are based on two hourly means of 1 min values from the OMNI data-base, `http://omniweb.gsfc.nasa.gov`, prior to the data timestamp.

Observed field GVO estimates are derived from sums and differences (along-track and also across track in the case of *Swarm* Alpha and Charlie) of the selected data, taking all data falling within 700 km of the GVO target location during the specified time window (1 or 4 months), fitting these by a local potential and then using this potential to estimate the vector field at the target location.

Core field GVO estimates are derived in the 1 monthly case by applying Principle Component Analysis (Cox et al, 2018) denoising to identify and remove local time and obvious external signals, then performing an epoch-by-epoch spherical harmonic analysis to identify and remove as far as possible remaining external and toroidal fields. For the 4 monthly datafiles, a-priori estimates of the magnetopheric field and associated induced field from the CHAOS model (Olsen et al, 2006; Finlay et al, 2020) and the ionospheric field and associated induced field from the CM4 model (Sabaka et al, 2004) were removed from the satellite data prior to fitting the potential and then epoch-by-epoch spherical harmonic analysis was applied to identify and remove remaining external and toroidal fields. Identical data selection and processing steps were applied to the *Swarm*, CHAMP and Cryosat-2 data (for a more detailed description of the algorithm, see Hammer et al, 2020a).

The GVO datasets for *Swarm*, CHAMP and Cryosat-2 have been archived online at:

`http://www.spacecenter.dk/files/magnetic-models/GVO/GVO_data_SWARM.zip`
`http://www.spacecenter.dk/files/magnetic-models/GVO/GVO_data_CHAMP.zip`
`http://www.spacecenter.dk/files/magnetic-models/GVO/GVO_data_CRYOSAT2.zip`

Each zip file contains the GVO datafiles (1 monthly or 4 monthly cadence) in the same .cdf format Hammer et al (2020c) along with a readme file summarizing the satellite data sources, selection criteria and processing steps applied. Filenames are of the form $YY\_OPER\_VOBS\_XM\_2\_\_20131215T000000\_20200315T000000\_0101.cdf$ where YY indicates the satellite (SW for *Swarm*, CH for CHAMP, CR for Cryosat-2) and X is either 1 or 4 indicating 1 monthly or 4 monthly cadence respectively. The variables provided in the .cdf file are Timestamp for the GVO field estimate; Geocentric Latitude (degrees); Geocentic Longitude (degrees); Geocentric Radius (km); GVO estimate of observed field (nT) including all sources; Error estimate of observed field GVO (nT), derived from the misfit to the contributing data; GVO estimate of Core field(nT), where selection and de-noising has been applied to isolate the core field as far as possible; Error estimate of core field GVO (nT) based on comparison to the CHAOS field model, Timestamp for SV, GVO Core Field Secular Variation (SV) Estimate (nT/yr) derived from annual differences of the GVO estimate of Core field, and Error estimates for Core field SV GVO (nT/yr) again based on comparisons with the CHAOS field model.

To illustrate the GVO secular variation time series, Figure 2.2 presents composite GVO time series for the radial, southward and eastward field components, mapped from their nominal altitude to 700 km using the CHAOS-7.2 field model in order to aid visualization.

Table 2.1 below presents for comparison the start time, end time, altitude, number of GVOs, data cadence, and mean estimated uncertainties for the observed field and core field GVOs from *Swarm*, CHAMP and Cryosat-2.

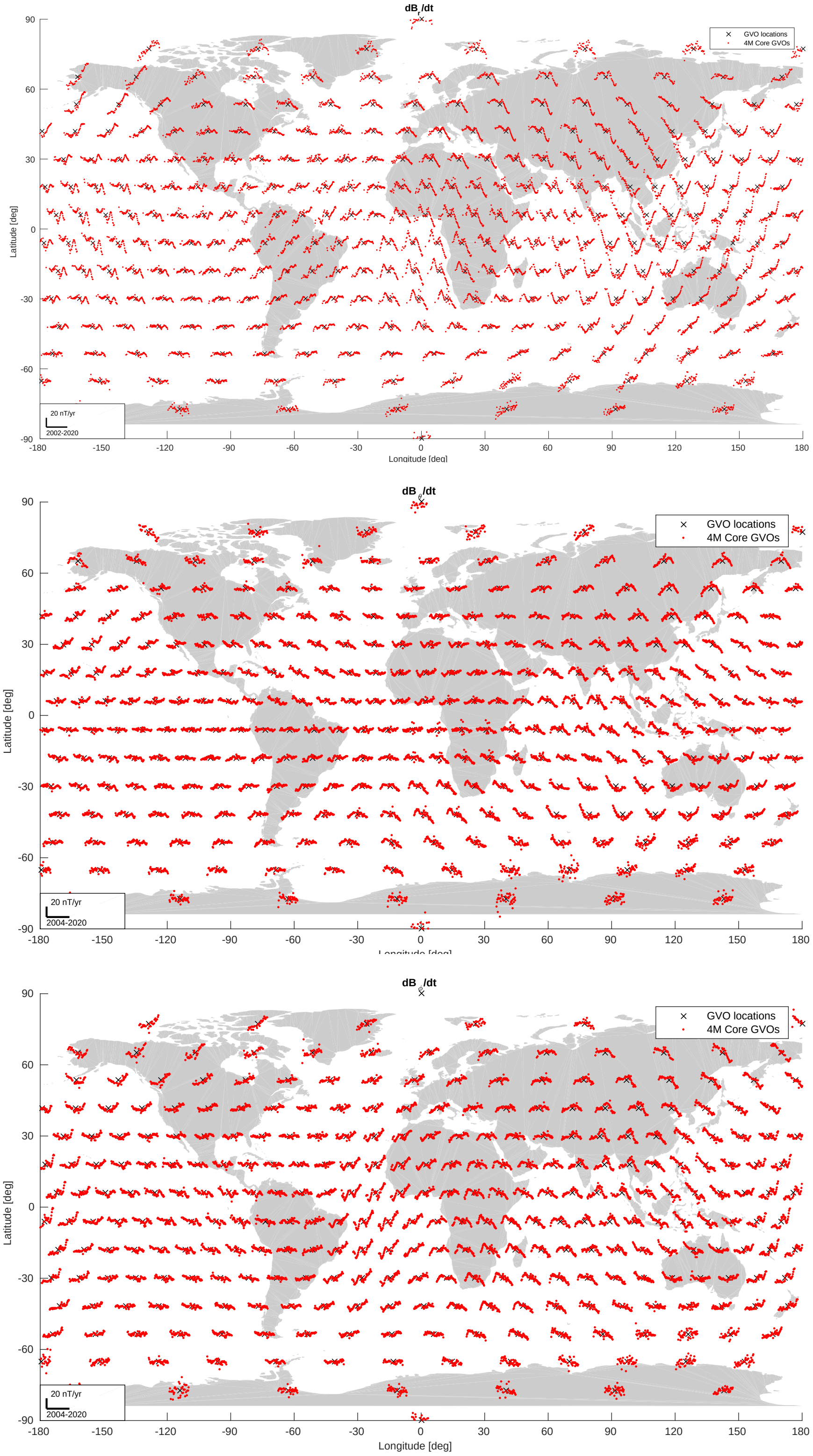

Figure 2.2: Composite GVO time-series of 4-monthly values of dB_r/dt (top), dB_θ/dt (middle) and dB_ϕ/dt (bottom) from CHAMP, Cryosat-2 and *Swarm*. For visualization this has been mapped to a common altitude of 700 km.

Table 2.1: Characteristics of GVO datasets from *Swarm*, CHAMP and Cryosat-2. σ^{Obs} denotes the mean over all GVO locations of the estimated uncertainties on the observed field GVOs, derived from their misfit to the contributing satellite data, σ^{SV} denotes the mean over all GVO locations of the supplied uncertainties on the core field SV, derived using comparisons to the CHAOS-7 field model.

	Start date	End date	Altitude [km]	GVOs	Cadence [months]	$\sigma^{Obs}_{B_r}$ [nT]	$\sigma^{Obs}_{B_\theta}$ [nT]	$\sigma^{Obs}_{B_\phi}$ [nT]	$\sigma^{SV}_{B_r}$ [nT/yr]	$\sigma^{SV}_{B_\theta}$ [nT/yr]	$\sigma^{SV}_{B_\phi}$ [nT/yr]
Swarm	2013.12.15	2020.03.15	490	300	1	4.17	7.18	6.92	1.62	1.66	1.32
Swarm	2014.03.01	2020.03.01	490	300	4	1.77	3.35	2.77	1.27	1.41	2.28
CHAMP	2000.08.15	2010.09.15	370	300	1	5.13	8.33	7.69	4.53	5.38	6.50
CHAMP	2001.03.01	2010.07.01	470	300	4	2.30	3.87	3.02	2.11	1.81	1.79
Cryosat-2	2010.07.01	2018.11.01	727	300	4	4.47	6.47	5.20	3.49	4.00	3.04

2.1.3 An update of the CHAOS field model and delivery of related datasets

The CHAOS (CHAMP, Ørsted, and *Swarm*) geomagnetic field model (Olsen et al, 2006, 2014; Finlay et al, 2020) is a time-dependent spherical harmonic model of the near-Earth geomagnetic field that aims to represent the internal field to high resolution in space and time. It has been developed at DTU over the past 15 years and is fitted directly to satellite data in the magnetometer frame, using vector field data (and along and cross track field differences) at non-polar latitudes and scalar data (and along and cross track differences) at polar latitudes, using data from dark and geomagnetically quiet time and co-estimating near-Earth magnetospheric sources. With support in part from the 4D Earth project it has recently been updated to CHAOS-7 using data the latest *Swarm* dta, as well as platform magnetometer from the Cryosat-2 mission whose use was made possible by co-estimating magnetometer calibration parameters (Finlay et al, 2020).

2.1.4 Satellite data

Here we provide details of the satellite data used to derive the latest update of the CHAOS model, CHAOS-7.3. These have been extracted for delivery as part of the 4D Earth project. Histograms showing the various data sets contributing to CHAOS-7.3 are presented in Fig. 2.3.

Table 2.2: Characteristics of CHAOS-7.3 satellite datasets, vector field.

					rms misfit, CHAOS-7.3		
	Start date	End date	Mean Altitude [km]	No. triples	B_r [nT]	B_θ [nT]	B_ϕ [nT]
Ørsted	1999.03.16	2005.12.06	756	48109	4.03	4.68	4.76
CHAMP	2000.07.27	2010.09.03	357	227145	1.71	2.35	1.95
Cryosat-2	2010.08.01	2014.12.27	728	71151	4.98	6.00	6.67
Swarm A,B,C	2013.11.26	2020.07.20	473	197443	1.49	3.16	1.96

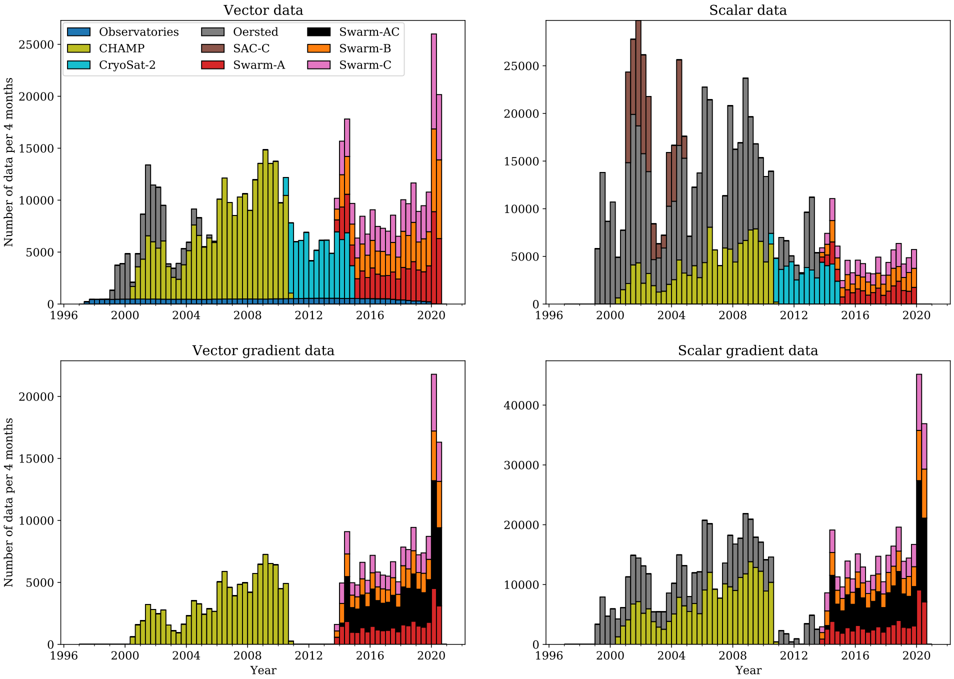

Figure 2.3: Histograms showing number of data of difference types used to construct the CHAOS-7.3 geomagnetic field model.

Table 2.3: Characteristics of CHAOS-7.3 satellite datasets, scalar field.

	Start date	End date	Mean Altitude [km]	No. triples	rms misfit, CHAOS-7.3 *F* [nT]
Ørsted	1999.03.15	2013.06.25	750	352232	2.23
CHAMP	2000.07.27	2010.09.03	357	227145	1.71
SAC-C	2001.01.23	2004.12.03	711	76104	2.96
Cryosat-2	2010.08.01	2014.12.30	726	48679	7.66
Swarm A,B,C	2013.11.26	2019.12.31	474	80190	3.42

A .zip file containing the various satellite data used in building CHAOS-7.3, labelled by data mission and type is available at:

`http://www.spacecenter.dk/files/magnetic-models/CHAOS-7/CHAOS-7_3_data.zip`

2.1.5 Ground observatory data

Here we provide brief details of the ground observatory data set used in CHAOS-7.3, that has also been extracted and delivered as part of the 4D Earth project.

Annual differences of revised observatory monthly means (Olsen et al, 2014) for the time interval January 1997 to July 2020 were used to provide additional constraints on the secular variation. Revised monthly means were derived from the hourly mean values at the 183 observatories shown in Fig. 2.4 (including 11 with minor site changes during the considered time interval) which were checked for trends, spikes and other errors (Macmillan and Olsen, 2013). Monthly means were calculated by a robust method based on Huber weights (Huber, 2004), from all local times at all latitudes. We removed estimates of the ionospheric (plus induced) field as predicted by the CM4 model (Sabaka et al, 2004) and the large-scale magnetospheric (plus induced) field, predicted by a preliminary field model, CHAOS-7.2.

A .zip file containing the ground observatory revised monthly mean data as used to build CHAOS-7.3 has been made available at:

`http://www.spacecenter.dk/files/magnetic-models/GOBS/GO_V33_1monthly.zip`

A version of the ground observatory data, based on the same hourly mean data but with revised means computed over 4 month windows is available at:

`http://www.spacecenter.dk/files/magnetic-models/GOBS/GO_V33_4monthly.zip`

Finally a version of the ground observatory data, based on the same hourly mean data but computing simple annual means to allow comparison with historical observatory annual means, is available at:

`http://www.spacecenter.dk/files/magnetic-models/GOBS/GO_V33_1yr.zip`

Examples of one monthly revised monthly means, with the CHAOS-7.3 model shown for reference are presented in Fig. 2.5.

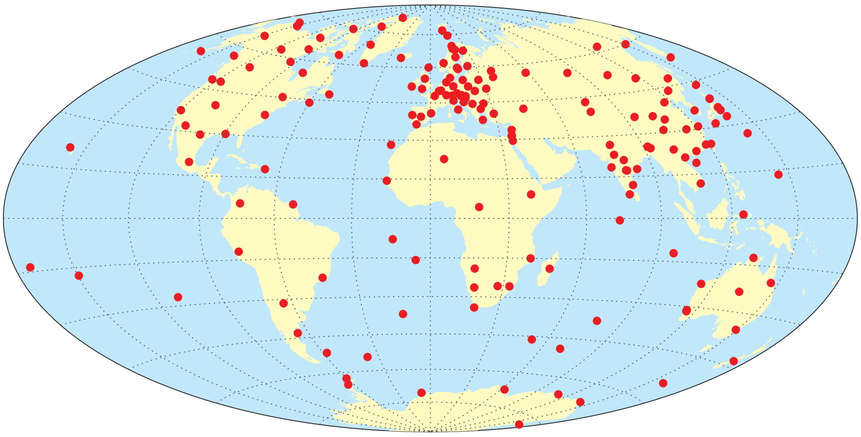

Figure 2.4: Map showing positions of ground observatories. IAGA codes for the stations are: AAA0, AAE1, ABG0, ABG1, ABK0, AIA0, ALE0, AMS0, AMT0 , API0 , API2, AQU0, ARS0, ASC0, ASP0, BDV0, BEL0, BFE0, BFO0, BGY1, BJN1, BLC0, BMT1, BNG0, BOU0, BOX0, BRW0, BSL0, BSL1, CBB0, CBI0, CDP0, CDP2, CKI0, CLF0, CMO3, CNB0, CNH3, COI0, CPL0, CSY0, CSY1, CTA0, CTS0, CYG0, CZT0, DED0, DLR0, DLT0, DOB1, DOU0, DRV0, EBR0, ELT0, ESA0, ESK0, EYR0, FCC0, FRD0, FRN0, FUQ0, FUR0, GAN0, GCK0, GDH2, GLM0, GNA0, GNG0, GUA0, GUI0, GUI3, GZH2, HAD0, HBK0, HER0, HLP0, HON3, HRB0, HRN0, HTY0, HUA0, HYB0, IPM0, IQA0, IQA1, IRT2, IZN0, JAI0, JCO0, KAK0, KDU0, KEP0, KHB0, KIR0, KIV2, KMH0, KMH1, KNY0, KNZ0, KOU0, KSH0, KSH1, LER0, LIV0, LMM0, LNP0, LON0, LOV0, LRM0, LRV0, LVV2, LYC0, LZH1, MAB0, MAW0, MBO0, MCQ0, MEA0, MGD0, MIZ0, MMB0, MNK0, MOS0, MZL0, NAQ0, NCK0, NEW0, NGK0, NGP1, NMP1, NUR0, NVS0, OTT0, PAF2, PAG0, PBQ0, PEG2, PET2, PHU0, PHU1, PIL0, PND0, PPT0, PST0, QGZ1, QIX0, QIX1, QSB0, QZH0, RES0, SBA0, SBL0, SFS2, SHE0, SHL0, SHU0, SIL0, SIT2, SJG2, SOD3, SPT0, SSH0, STJ0, SUA0, SUA, TAM0, TAN0, TDC0, TEO0, TFS0, THJ0, THL0, THY0, TIR0, TIR1, TND0, TRO0 , TRW0, TSU0, TUC2, UJJ0, UPS0, VAL0, VIC0, VNA0, VSK0, VSK1, VSS0, WHN0, WIC0, WIK0, WNG0, YAK1, YKC2.

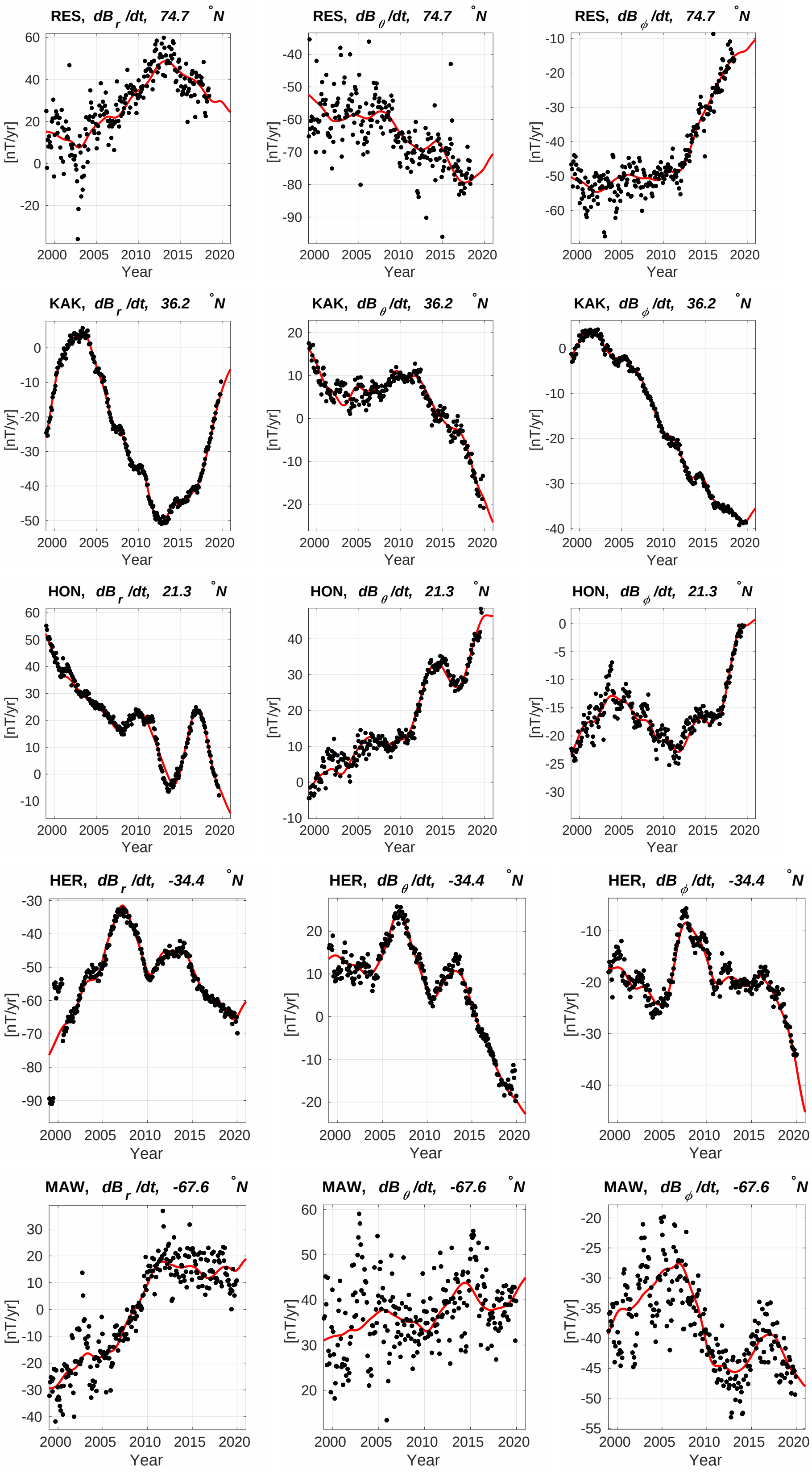

Figure 2.5: Fit of the CHAOS-7.3 model (red line) to secular variation data, annual differences of revised monthly means (black dots), at example ground observatories.

2.1.6 The CHAOS-7.3 model

The CHAOS-7.3 model was derived in August 2020 using the modelling approach as for CHAOS-7 (Finlay et al, 2020) but with updated *Swarm* and ground observatory data and slightly increased regularization of time-dependent core field and much stronger regularization of the Cryosat-2 s_1 magnetometer sensitivities. Details of the model parameterization is given in Table 2.4.

Table 2.4: Summary of parameters defining the model setup in CHAOS-7.3.

Setup Parameter	Description	
N_{tdep}	Maximum SH degree of time-dependent internal field	20
J	Order of B-Splines	6
Δt_k	B-spline knot spacing	0.5 yr
t_{start}	Start time of spline basis	1997.1
t_{end}	End time of spline basis	2021.1
N_{int}	Maximum SH degree of static internal field	185
N_{SM}	Maximum SH degree of SM external field	2
ΔT_{SM1}	Bin size for degree 1 SM offsets	30 days
N_{GSM}	Maximum SH degree of GSM external field	2 (only $m = 0$ terms)
ΔT_{Euler}	Bin size for Euler angle determination	10 days
ΔT_{CAL}	Bin size for calibration parameters	21 days

The time-dependent internal field part of CHAOS-7.3 model has been archived in .mat, .shc and in spline coefficient formats at:

http://www.spacecenter.dk/files/magnetic-models/CHAOS-7/CHAOS-7.3.mat
http://www.spacecenter.dk/files/magnetic-models/CHAOS-7/CHAOS-7.3_core.shc
http://www.spacecenter.dk/files/magnetic-models/CHAOS-7/CHAOS-7.3_spline-coefficients.d

The latest version of the *chaosmagpy* python forward package, that can be used to evaluate CHAOS-7.3, is available from

https://pypi.org/project/chaosmagpy/

Fig. 2.6 below shows maps of the radial component of the magnetic field, and its first and second time-derivatives (the secular variation and secular acceleration) downward continued to the core-mantle boundary in 2020.0. Note the enhanced amplitudes of secular variation and secular acceleration at low latitudes and in the northern polar region. Fig. 2.7 presents time series of the secular variations of selected spherical harmonic coefficients, along with two other recent models constructed with different modelling methods, CM6 (Sabaka et al, 2020) and model MCO_SHA_2Y, an early model derived using the approach of Ropp et al (2020).

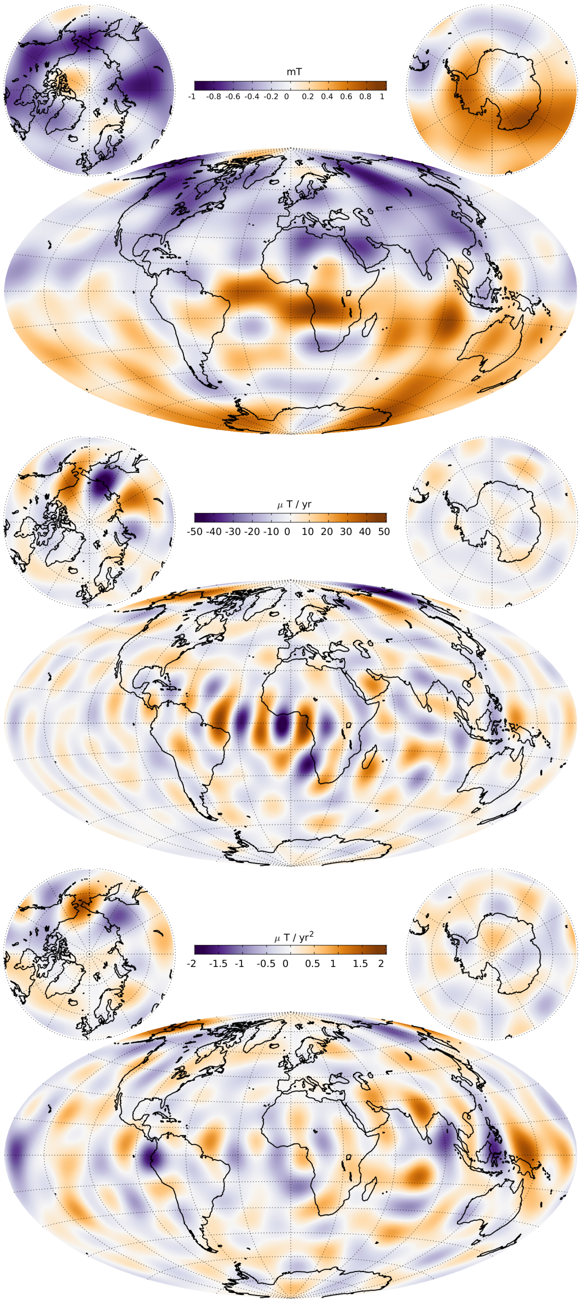

Figure 2.6: Maps from CHAOS-7.3 of the radial magnetic field (MF, top row), its first time derivative (SV, middle row) and second time derivative (SA, bottom row) at the core-mantle boundary in 2020.0, Truncation degrees are 13, 17 and 15 respectively for the MF, SV and SA.

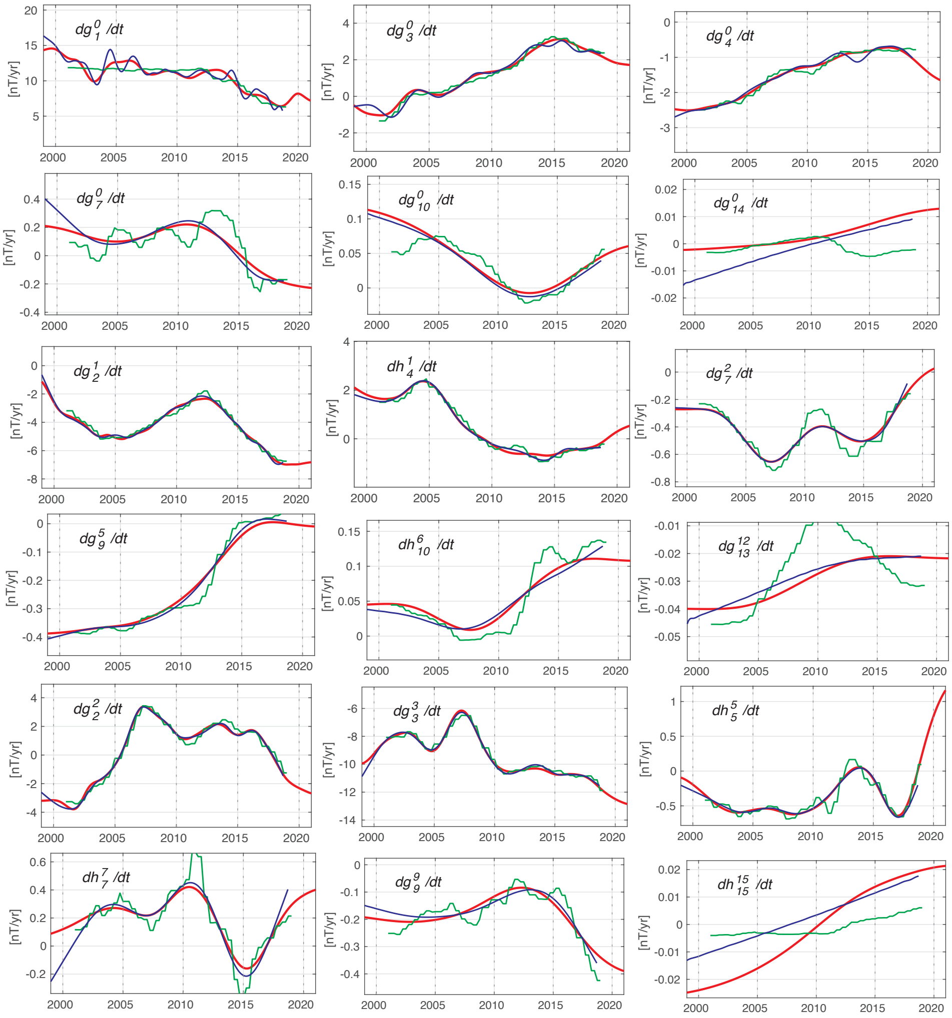

Figure 2.7: Time-dependence of example spherical harmonic coefficients of the internal field SV from CHAOS-7.3 (solid red line). Also shown are the CM6 model of Sabaka et al (2020)(blue line) and model MCO_SHA_2Y, an early model derived using the approach of Ropp et al (2020) (green line). Top two rows are zonal coefficients, bottom two rows are sectoral coefficients, middle two rows are tesseral coefficients.

2.1.7 Summary

This report has described initial deliveries for the 4D Deep Earth:Core project of GVO datasets from *Swarm*, CHAMP and Cryosat-2, constructed using identical processing schemes; an update of the CHAOS field model to version 7.3 using the latest *Swarm* and ground observatory data, and related satellite and ground observatory datasets. These constitute delivery D-B.1 by DTU.

Links to all the datafiles described above will be available on the 4D Earth webpage:

`https://4d-earth-swarm.univ-grenoble-alpes.fr/`

Bibliography

Cox G, Brown WJ, Billingham L, Holme R (2018) MagPySV: A Python package for processing and denoising geomagnetic observatory data. Geochemistry, Geophysics, Geosystems 19(9):3347–3363

Finlay CC, Kloss C, Olsen N, Tøffner-Clausen L, Grayver A, Kuvshinov A (2020) The CHAOS-7 geomagnetic field model and observed changes in the South Atlantic Anomaly. Earth Planets Space 72, DOI 10.1186/s40623-020-01252-9

Hammer MD, Cox GA, Brown WJ, Beggan C, Finlay CC (2020a) Geomagnetic Virtual Observatories: Monitoring geomagnetic secular variation with the Swarm satellites. Earth Planets Space xx:(in prep)

Hammer MD, Cox GA, Brown WJ, Beggan C, Finlay CC (2020b) Swarm data, innovation, and science cluster, geomagnetic virtual observatory project: Description of algorithm. Available at `http://www.spacecenter.dk/files/magnetic-models/GVO/GVO_Product_Algorithm.pdf`(2020/09/14)

Hammer MD, Cox GA, Brown WJ, Beggan C, Finlay CC (2020c) Swarm data, innovation, and science cluster, geomagnetic virtual observatory project: Product definition document. Available at `http://www.spacecenter.dk/files/magnetic-models/GVO/GVO_Product_Definition.pdf`(2020/09/14)

Hammer MD, Cox GA, Brown WJ, Beggan C, Finlay CC (2020d) Swarm data, innovation, and science cluster, geomagnetic virtual observatory project: Validation document. Available at `http://www.spacecenter.dk/files/magnetic-models/GVO/GVO_Validation.pdf`(2020/09/14)

Huber PJ (2004) Robust statistics. Wiley

Leopardi P (2006) A partition of the unit sphere into regions of equal area and small diameter. Electronic Transactions on Numerical Analysis 25(12):309–327

Macmillan S, Olsen N (2013) Observatory data and the Swarm mission. Earth, Planets and Space 65:1355–1362

Mandea M, Olsen N (2006) A new approach to directly determine the secular variation from magnetic satellite observations. Geophys Res Lett 33:L15,306, DOI 10.1029/2006GL026616

Olsen N, Mandea M (2007) Investigation of a secular variation impulse using satellite data: The 2003 geomagnetic jerk. Earth Planet Sci Lett 255:94–105, DOI 10.1016/j.epsl.2006.12.008

Olsen N, Lühr H, Sabaka TJ, Mandea M, Rother M, Tøffner-Clausen L, Choi S (2006) CHAOS – a model of Earth's magnetic field derived from CHAMP, Ørsted, and SAC-C magnetic satellite data. Geophys J Int 166:67–75, DOI 10.1111/j.1365-246X.2006.02959.x

Olsen N, Lühr H, Finlay CC, Tøffner-Clausen L (2014) The CHAOS-4 Geomagnetic Field Model. Geophys J Int 1997:815–827

Olsen N, Albini G, Bouffard J, Parrinello T, Tøffner-Clausen L (2020) Magnetic observations from CryoSat-2: calibration and processing of satellite platform magnetometer data. Earth, Planets and Space 72

Reigber C, Lühr H, Schwintzer P, Wickert J (2005) Earth Observation with CHAMP, Results from Three Years in Orbit. Springer Verlag, Berlin

Ropp G, Lesur V, Baerenzung J, Holschneider M (2020) Sequential modelling of the earth's core magnetic field. Earth, Planets and Space (in press)

Sabaka TJ, Olsen N, Purucker ME (2004) Extending comprehensive models of the Earth's magnetic field with Ørsted and CHAMP data. Geophys J Int 159:521–547, DOI 10.1111/j.1365-246X.2004.{02421}.x

Sabaka TJ, Tøffner-Clausen L, Olsen N, Finlay CC (2020) CM6: A comprehensive geomagnetic field model derived from both champ and swarm satellite observations. Earth, Planets and Space 72, DOI 10.1186/s40623-020-01210-5

2.2 Long time series of outputs from a geodynamo model approaching Earth's core conditions

4DEarth_Swarm_Core ESA project deliverable D-C.1

J. Aubert
IPG Paris

2.2.1 General description

This document refers to publicly available output data from a geodynamo simulation that approaches closely to the physical conditions of Earth's core. In the model parameter space, this model is part of a series that defines a path connecting the conditions where classical dynamo models are found to those of the Earth's core. The theoretical definition of this path may be found in Aubert et al (2017), and the model described here is located at 71% of this path (path parameter $\epsilon = 10^{-5}$). The outputs that are made available here consist in coefficients describing the poloidal magnetic field outside the core, the diffusive part of the poloidal magnetic field temporal rate-of-change (the secular variation), and the coefficients describing the velocity field at the core surface. The model operates with stress-free boundary conditions, which implies that Ekman boundary layers are not described and that the core surface directly corresponds to the free stream. Table 2.5 lists the key time scales and associated dimensionless numbers of this model together with those expected at Earth's core conditions.

From the dimensionless outputs of the numerical model, the values of the velocity and magnetic field coefficients presented in the data file are **already scaled to dimensional values**, in nanoteslas for the magnetic field, nanoteslas per year for the diffusive part of the secular variation, and kilometers per year for the velocity field. Here I mention some details for the re-scaling procedure that has been applied. Re-scaling can be done in a completely self-consistent manner only once the model conditions reach those of the Earth's core. The path theory serves to rescale these quantities in a way that rationalizes the gap that still exists between those two conditions (Aubert, 2018, 2020). For the time series presented here, the time basis is provided by the choice of the magnetic diffusivity η in table 2.5. From there and the value of the magnetic Reynolds number Rm immediately follow the determination of the core overturn time τ_U involving the root-mean-squared flow velocity U in the shell and the re-scaling of the velocity field. The value of the Lundquist number gives access to the Alfvén time τ_A, which however differs from its target Earth value as we are not yet at the end of the path. The r.m.s dimensional magnetic field amplitude B can therefore be obtained by considering that the density ρ of the simulated fluid shell is $(5.8/2)^2$ time stronger than its Earth counterpart $\rho = 11000\ \mathrm{kg/m^3}$, this former factor accounting for the differences in the model

Quantity	Definition	71% of path model	Earth's core
Earth radius	a	6371.2 km	6371.2 km
core surface radius	r_o	3485 km	3485 km
outer core thickness	D	2260 km	2260 km
magnetic diffusivity	η	1.2 m^2/s	$\approx$ 1.2 m^2/s
magnetic diffusion time	$\tau_\eta = D^2/\eta$	135000 yr	$\approx$ 135000 yr
planetary rotation period	$2\pi\tau_\Omega = 2\pi/\Omega$	12 days	1 day
Alfvén time	$\tau_A = \sqrt{\rho\mu}D/B$	5.8 yr	$\approx$ 2 yr
1D Alfvén speed	$D/\sqrt{3}\tau_A$	225 km/yr	$\approx$ 650 km/yr
core overturn time	$\tau_U = D/U$	118 yr	$\approx$ 120 yr
1D convective speed	$D/\sqrt{3}\tau_U$	11 km/yr	$\approx$ 11 km/yr
Magnetic Ekman number	$E/Pm = \tau_\Omega/\tau_\eta$	$3.8\ 10^{-8}$	$\approx 3.2\ 10^{-9}$
Magnetic Reynolds number	$Rm = \tau_\eta/\tau_U$	1140	$\approx$ 1100
Lundquist number	$S = \tau_\eta/\tau_A$	23300	$\approx$ 68000

Table 2.5: Key parameters for the model, presented together with their model values and values expected at Earth's core conditions. B and U are root-mean-squared amplitudes of the magnetic field inside the simulated core.

and Earth Alfvén times.

Figure 2.8 presents temporal sequences of the core-mantle boundary secular acceleration energy (as defined in Aubert, 2018) and Earth-surface jerk energy (as defined in Aubert and Finlay, 2019). The sequence contained in the data files starts at timestamp 4200 years. The preceding temporal sequence is not proposed as it contains a number of changes in model resolution, output resolution, time step that have followed from the need to tackle numerical instabilities and from discussions within the consortium, which make this earlier part of the model unsuitable for public release. The duration of the released sequence is currently 8811.3 years. The numerical time step used for the computation is 0.3 hours. Outputs have been recorded at a sampling rate of 30 hours. The sampling rate selected for public release is 0.2 years. The consortium is free to discuss whether a faster delivery sampling rate is needed, but it should be kept in mind that this comes at the cost of file size. Furthermore, we have previously shown (Aubert, 2018) that the signal contains almost no energy at periods shorter than the planetary rotation period $2\pi\tau_\Omega$ = 283 hours = 11.8 days = 0.03 years. The time stamps for notable jerk events are reported in table 2.6.

2.2.2 Data format and description

The file format is MATLAB `.mat`.

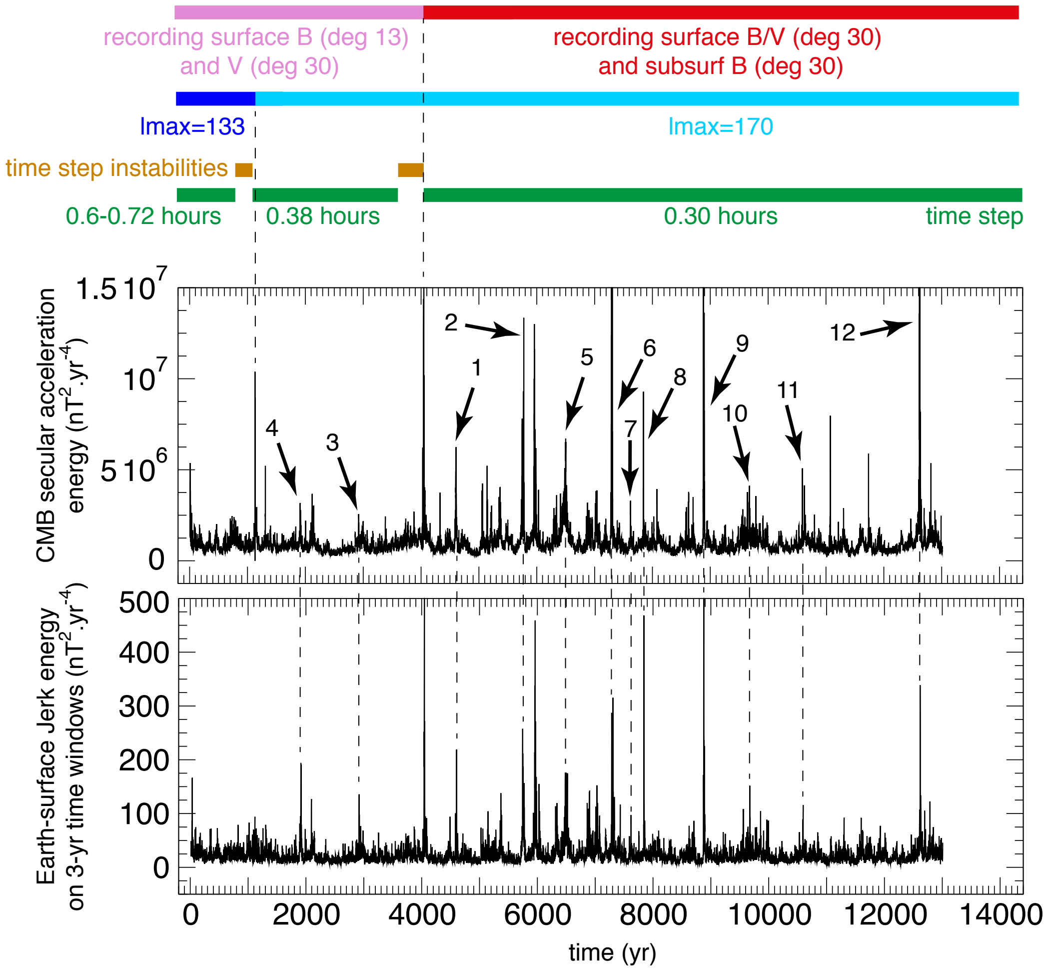

Figure 2.8: Core-mantle boundary (CMB) secular acceleration energy (top) and Earth-surface jerk energy (bottom), as functions of the dimensional simulation time. See Aubert (2018); Aubert and Finlay (2019) for definitions. The outputs have been truncated here at spherical harmonic degree and order 13 (which is the minimum spatial resolution for outputs of the whole sequence), but the publicly available outputs are supplied up to a higher spherical harmonic resolution of 30. The colored bands above the graphs locate notable events in the simulation concerning the nature and maximum spherical harmonic degree of outputs (pink/red), the native spherical harmonic degree $\ell_{\max}$ of the computation (blue/cyan), the computation time step values (green) and encountered instabilities thereof (brown).

Jerk No.	timestamp (years)
1	4600
2	5750
5	6490
6	7300
7	7620
8	7840
9	8880
10	9673
11	10590
12	12620

Table 2.6: Approximate timestamps for notable jerks in the publicly available part of the sequence.

2.2.3 Magnetic field coefficients

To describe the magnetic field at and above the core surface, we adopt the classical Gauss coefficient description for the magnetic field. Denoting the colatitude as θ and the Greenwich-centered longitude as φ, the poloidal field at a radius r above the core-mantle boundary may be written

$$\mathbf{B}_{\boldsymbol{p}}(r,\theta,\varphi,t) = -\boldsymbol{\nabla} V \tag{2.1}$$

where

$$V(r,\theta,\varphi,t) = a \sum_{l=1}^{30} \left(\frac{a}{r}\right)^{l+1} \sum_{m=0}^{l} \left[g_l^m(t)\cos m\varphi + h_l^m(t)\sin m\varphi\right] P_l^m(\cos\theta). \tag{2.2}$$

Here t is time, $a = 6371.2$ km is Earth's magnetic radius of reference, P_l^m is the Schmidt-seminormalised Legendre function of degree l and order m.

The file `gauss_Bsurf.mat` comprises the dimensional timestamp vector `timers` containing the discrete values of t and an array `gnm` containing the coefficients $g_l^m(t)$, $h_l^m(t)$ arranged according to:

$$
\begin{aligned}
\texttt{gnm}(:,1) &= g_1^0(t)\\
\texttt{gnm}(:,2) &= g_1^1(t)\\
\texttt{gnm}(:,3) &= h_1^1(t)\\
\texttt{gnm}(:,4) &= g_2^0(t)\\
\texttt{gnm}(:,5) &= g_2^1(t)\\
\texttt{gnm}(:,6) &= h_2^1(t)\\
\texttt{gnm}(:,7) &= g_2^2(t)\\
\texttt{gnm}(:,8) &= h_2^2(t)\\
&\ldots\\
\texttt{gnm}(:,959) &= g_{30}^{30}(t)\\
\texttt{gnm}(:,960) &= h_{30}^{30}(t)
\end{aligned}
$$

Note that the sinus coefficients corresponding to $m = 0$ are not stored as they vanish identically. There are therefore 960 coefficients corresponding to a description of the output up to spherical harmonic degree and order 30. The core surface poloidal magnetic field is then obtained by setting r to $r_o = 3485$ km in equation (2.2).

In file `gauss_Magdiff.mat` the Gauss coefficients corresponding to the diffusive part $\eta\nabla^2\mathbf{B_p}$ of the secular variation $\partial\mathbf{B_p}/\partial t$ below the core surface are encoded in the variable `dgnm` together with the time stamp `timers`. The advective part of the secular variation can then be obtained by taking the centered finite differences of variable `gnm` from file `gauss_Bsurf.mat` and subtracting `dgnm` to the result. The magnetic diffusion obviously does only make sense at the core surface i.e. by setting r to $r_o = 3485$ km in equation (2.2), but its representation in terms of the same Gauss coefficients as those used for the poloidal field allows to quickly apprehend its contribution to the total secular variation, and also to quickly convert the output to a radial magnetic field, which is the representation that is usually preferred to cast the magnetic induction equation at the core surface.

2.2.4 Velocity field coefficients

The core surface velocity field coefficients are described using the spheroidal-toroidal formalism. The θ and φ components of the core surface velocity vector $\mathbf{u}$ are written

$$
\mathbf{u} = \begin{pmatrix} u_\theta = \dfrac{1}{\sin\theta}\dfrac{\partial T}{\partial\varphi} + \dfrac{\partial S}{\partial\theta} \\ u_\varphi = -\dfrac{\partial T}{\partial\theta} + \dfrac{1}{\sin\theta}\dfrac{\partial S}{\partial\varphi} \end{pmatrix} \tag{2.3}
$$

The spectral decomposition of T, S obeys

$$T = \sum_{l=1}^{30} \sum_{m=0}^{l} \left[tc_l^m(t) \cos m\varphi + ts_l^m(t) \sin m\varphi \right] P_l^m(\cos\theta) \tag{2.4}$$

$$S = \sum_{l=1}^{30} \sum_{m=0}^{l} \left[sc_l^m(t) \cos m\varphi + ss_l^m(t) \sin m\varphi \right] P_l^m(\cos\theta) \tag{2.5}$$

The file `gauss_Vsurf.mat` contains the timestamp `timers` together with two arrays `tnm` and `snm` where the coefficients tc_l^m,ts_l^m and sc_l^m,ss_l^m are respectively stored. The ordering follows that of the magnetic field Gauss coefficients i.e.

$$\begin{aligned}
\texttt{tnm}(:,1) &= tc_1^0(t)\\
\texttt{tnm}(:,2) &= tc_1^1(t)\\
\texttt{tnm}(:,3) &= ts_1^1(t)\\
\texttt{tnm}(:,4) &= tc_2^0(t)\\
\texttt{tnm}(:,5) &= tc_2^1(t)\\
\texttt{tnm}(:,6) &= ts_2^1(t)\\
\texttt{tnm}(:,7) &= tc_2^2(t)\\
\texttt{tnm}(:,8) &= ts_2^2(t)\\
&\dots\\
\texttt{tnm}(:,959) &= tc_{30}^{30}(t)\\
\texttt{tnm}(:,960) &= ts_{30}^{30}(t)
\end{aligned}$$

Note that the sinus coefficients corresponding to $m = 0$ are not stored as they vanish identically. As for the magnetic field coefficients above there are 960 coefficients for each scalar, corresponding to a description of the output up to spherical harmonic degree and order 30.

Links to all the datafiles described above will be available on the 4D Earth webpage:

https://4d-earth-swarm.univ-grenoble-alpes.fr/

Bibliography

Aubert J (2018) Geomagnetic acceleration and rapid hydromagnetic wave dynamics in advanced numerical simulations of the geodynamo. Geophys J Int 214(1):531–547

Aubert J (2020) Recent geomagnetic variations and the force balance in Earth's core. Geophys J Int DOI 10.1093/gji/ggaa007, doi: 10.1093/gji/ggaa007

Aubert J, Finlay CC (2019) Geomagnetic jerks and rapid hydromagnetic waves focusing at Earth's core surface. Nature Geosci 12(5):393–398, DOI 10.1038/s41561-019-0355-1

Aubert J, Gastine T, Fournier A (2017) Spherical convective dynamos in the rapidly rotating asymptotic regime. J Fluid Mech 813:558–593

2.3 A catalogue of simulated jerks from a geodynamo model approaching Earth's core conditions

4DEarth_Swarm_Core ESA project deliverable D-E.1

J. Aubert
IPG Paris

2.3.1 General description

This document refers to publicly available output data from a geodynamo simulation that approaches closely to the physical conditions of Earth's core. In the model parameter space, this model is part of a series that defines a path connecting the conditions where classical dynamo models are found to those of the Earth's core. The theoretical definition of this path may be found in Aubert et al (2017), and the model described here is located at 71% of this path (path parameter $\epsilon = 10^{-5}$). This model is fully described in Aubert and Gillet (2021). Table 2.7 lists the key time scales and associated dimensionless numbers of this model together with those expected at Earth's core conditions.

From the dimensionless outputs of the numerical model, the provided data files are **already scaled to dimensional values**. Here I mention some details for the re-scaling procedure that has been applied. Re-scaling can be done in a completely self-consistent manner only once the model conditions reach those of the Earth's core. The path theory serves to rescale these quantities in a way that rationalizes the gap that still exists between those two conditions (Aubert, 2018, 2020). For the time series presented here, the time basis is provided by the choice of the magnetic diffusivity η in table 2.7. From there and the value of the magnetic Reynolds number Rm immediately follow the determination of the core overturn time τ_U involving the root-mean-squared flow velocity U in the shell and the re-scaling of the velocity field. The value of the Lundquist number gives access to the Alfvén time τ_A, which however differs from its target Earth value as we are not yet at the end of the path. The r.m.s dimensional magnetic field amplitude B can therefore be obtained by considering that the density ρ of the simulated fluid shell is $(5.8/2)^2$ time stronger than its Earth counterpart $\rho = 11000\ \mathrm{kg/m^3}$, this former factor accounting for the differences in the model and Earth Alfvén times. Finally, the density anomaly field is rescaled following Aubert and Gillet (2021), by expressing the dimensionless field in units of $\rho\Omega\eta/g_oD$ (where g_o is the gravity at the core surface), and multiplying the result with Earth's core dimensional estimate for $\rho\Omega\eta/g_oD$ obtained with $g_o = 10\ \mathrm{m/s^2}$, $\rho = 11000\ \mathrm{kg/m^3}$ and the other values from Table 2.7.

Figure 2.9 presents temporal sequences of the core-mantle boundary secular acceleration energy (as defined in Aubert, 2018) and Earth-surface jerk energy (as

Quantity	Definition	71% of path model	Earth's core
Earth radius	a	6371.2 km	6371.2 km
core surface radius	r_o	3485 km	3485 km
outer core thickness	D	2260 km	2260 km
magnetic diffusivity	η	1.2 m^2/s	$\approx$ 1.2 m^2/s
magnetic diffusion time	$\tau_\eta = D^2/\eta$	135000 yr	$\approx$ 135000 yr
planetary rotation period	$2\pi\tau_\Omega = 2\pi/\Omega$	12 days	1 day
Alfvén time	$\tau_A = \sqrt{\rho\mu}D/B$	5.8 yr	$\approx$ 2 yr
1D Alfvén speed	$D/\sqrt{3}\tau_A$	225 km/yr	$\approx$ 650 km/yr
core overturn time	$\tau_U = D/U$	118 yr	$\approx$ 120 yr
1D convective speed	$D/\sqrt{3}\tau_U$	11 km/yr	$\approx$ 11 km/yr
Magnetic Ekman number	$E/Pm = \tau_\Omega/\tau_\eta$	$3.8\ 10^{-8}$	$\approx 3.2\ 10^{-9}$
Magnetic Reynolds number	$Rm = \tau_\eta/\tau_U$	1140	$\approx$ 1100
Lundquist number	$S = \tau_\eta/\tau_A$	23300	$\approx$ 68000

Table 2.7: Key parameters for the model, presented together with their model values and values expected at Earth's core conditions. B and U are root-mean-squared amplitudes of the magnetic field inside the simulated core.

defined in Aubert and Finlay, 2019). The outputs that are made available here specifically focus on the 14 simulated geomagnetic jerk events marked with arrows in Figure 2.9. These ouputs first consist in high-resolution time series of the coefficents describing the poloidal magnetic field outside the core and the velocity field at the core surface. The time series cover a few decades before and after the approximate timestamps of jerks presented in Table 2.8. Their temporal resolution is set to 0.05 years i.e. four times finer than the long time series covering the entire sequence that were previously provided in deliverable D-C.1. The model operates with stress-free boundary conditions, which implies that Ekman boundary layers are not described and that the core surface directly corresponds to the free stream. For each jerk event, a collection of movies representing these time series is also provided. Finally, full three-dimensional states of the simulation at selected times are provided for a selection of jerks.

2.3.2 Data format and description

2.3.3 Magnetic field coefficients

To describe the magnetic field at and above the core surface, we adopt the classical Gauss coefficient description for the magnetic field. Denoting the colatitude as θ and the Greenwich-centered longitude as φ, the poloidal field at a radius r above the core-mantle boundary may be written

$$\mathbf{B}_p(r,\theta,\varphi,t) = -\nabla V \tag{2.6}$$

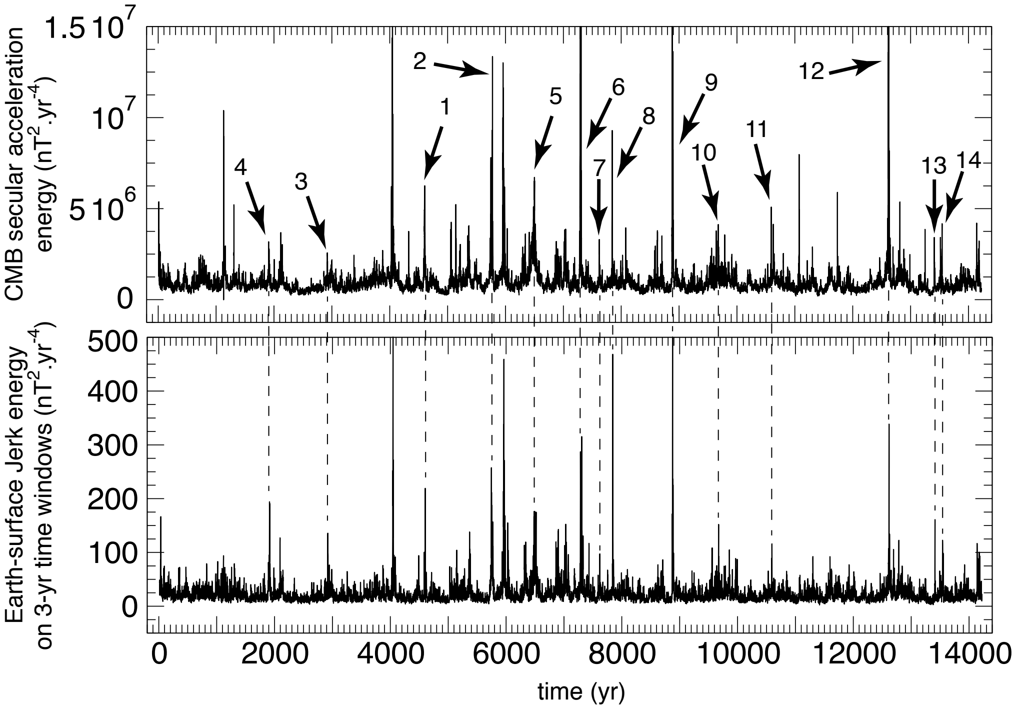

Figure 2.9: Core-mantle boundary (CMB) secular acceleration energy (top) and Earth-surface jerk energy (bottom), as functions of the dimensional simulation time. See Aubert (2018); Aubert and Finlay (2019) for definitions. Following these references, the outputs on this figure have been truncated at spherical harmonic degree and order 13, but the publicly available outputs are supplied up to a higher spherical harmonic resolution of 30.

Jerk No.	timestamp (years)	Jerk No.	timestamp (years)
1	4600	8	7840
2	5750	9	8880
3	2920	10	9673
4	1915	11	10590
5	6490	12	12620
6	7300	13	13411
7	7620	14	13546

Table 2.8: Approximate timestamps for simulated jerks in the catalog.

where

$$V(r, \theta, \varphi, t) = a \sum_{l=1}^{30} \left(\frac{a}{r}\right)^{l+1} \sum_{m=0}^{l} \left[g_l^m(t) \cos m\varphi + h_l^m(t) \sin m\varphi\right] P_l^m(\cos\theta). \tag{2.7}$$

Here t is time, $a = 6371.2$ km is Earth's magnetic radius of reference, P_l^m is the Schmidt-seminormalised Legendre function of degree l and order m.

For each jerk event, the file `Gauss_Bsurf.mat` (`MATLAB` data format) comprises the dimensional timestamp vector `timers` (in years) containing the discrete values of t and an array `gnm` containing the coefficients $g_l^m(t)$, $h_l^m(t)$ (in nanoteslas) arranged according to:

$$\begin{aligned}
\texttt{gnm}(:, 1) &= g_1^0(t) \\
\texttt{gnm}(:, 2) &= g_1^1(t) \\
\texttt{gnm}(:, 3) &= h_1^1(t) \\
\texttt{gnm}(:, 4) &= g_2^0(t) \\
\texttt{gnm}(:, 5) &= g_2^1(t) \\
\texttt{gnm}(:, 6) &= h_2^1(t) \\
\texttt{gnm}(:, 7) &= g_2^2(t) \\
\texttt{gnm}(:, 8) &= h_2^2(t) \\
&\dots \\
\texttt{gnm}(:, 959) &= g_{30}^{30}(t) \\
\texttt{gnm}(:, 960) &= h_{30}^{30}(t)
\end{aligned}$$

Note that the sinus coefficients corresponding to $m = 0$ are not stored as they vanish identically. There are therefore 960 coefficients corresponding to a description of the output up to spherical harmonic degree and order 30. The core surface poloidal magnetic field is then obtained by setting r to $r_o = 3485$ km in equation (2.7).

2.3.4 Velocity field coefficients

The core surface velocity field coefficients are described using the spheroidal-toroidal formalism. The θ and φ components of the core surface velocity vector $\mathbf{u}$ are written

$$\mathbf{u} = \begin{pmatrix} u_\theta = \dfrac{1}{\sin\theta}\dfrac{\partial T}{\partial\varphi} + \dfrac{\partial S}{\partial\theta} \\ u_\varphi = -\dfrac{\partial T}{\partial\theta} + \dfrac{1}{\sin\theta}\dfrac{\partial S}{\partial\varphi} \end{pmatrix} \tag{2.8}$$

The spectral decomposition of T, S obeys

$$T = \sum_{l=1}^{30} \sum_{m=0}^{l} \left[tc_l^m(t) \cos m\varphi + ts_l^m(t) \sin m\varphi \right] P_l^m(\cos\theta) \tag{2.9}$$

$$S = \sum_{l=1}^{30} \sum_{m=0}^{l} \left[sc_l^m(t) \cos m\varphi + ss_l^m(t) \sin m\varphi \right] P_l^m(\cos\theta) \tag{2.10}$$

For each jerk event, the file `Gauss_Vsurf.mat` (`MATLAB` data format) contains the timestamp `timers` (in years) together with two arrays `tnm` and `snm` (in km.rad/yr) where the coefficients tc_l^m,ts_l^m and sc_l^m,ss_l^m are respectively stored. The ordering follows that of the magnetic field Gauss coefficients i.e.

$$\begin{aligned}
\texttt{tnm}(:,1) &= tc_1^0(t)\\
\texttt{tnm}(:,2) &= tc_1^1(t)\\
\texttt{tnm}(:,3) &= ts_1^1(t)\\
\texttt{tnm}(:,4) &= tc_2^0(t)\\
\texttt{tnm}(:,5) &= tc_2^1(t)\\
\texttt{tnm}(:,6) &= ts_2^1(t)\\
\texttt{tnm}(:,7) &= tc_2^2(t)\\
\texttt{tnm}(:,8) &= ts_2^2(t)\\
&\dots\\
\texttt{tnm}(:,959) &= tc_{30}^{30}(t)\\
\texttt{tnm}(:,960) &= ts_{30}^{30}(t)
\end{aligned}$$

Note that the sinus coefficients corresponding to $m = 0$ are not stored as they vanish identically. As for the magnetic field coefficients above there are 960 coefficients for each scalar, corresponding to a description of the output up to spherical harmonic degree and order 30.

2.3.5 Movies

For each jerk event, a `.zip` archive is provided that contains the following `mp4` movie files:

- `Brcmb.mov` and `Brcmb13.mov`: core surface radial magnetic field (in mT), respectively at native (up to spherical harmonic degree 170) and truncated (up to spherical harmonic degree 13) resolutions,
- `Vpcmb.mov`: core surface azimuthal velocity field (in km/yr) at native resolution,
- `dVcmb.mov`: core surface azimuthal velocity acceleration (in km/yr^2) at native resolution,

- `SVcmb.mov`: core surface radial secular variation (first time derivative of the magnetic field, in $\mu\mathrm{T/yr}$) up to spherical harmonic degree 13,
- `SAcmb.mov` and `SAsurf.mov`: core surface and Earth surface radial secular acceleration (second time derivative of the magnetic field, in $\mathrm{nT/yr}^2$) up to spherical harmonic degree 13.

2.3.6 Full three-dimensional states

For jerks 1,3 and 9, two states of the simulations at native spatial resolution are provided as (very large) binary files `Gt1` and `Gt2`. The two states are closely spaced in time such that a time derivative can be reliably computed. The states can be loaded into computer memory by using the provided matlab script `parodyload_scaled.m`.

Once loaded, the following variables are present in `MATLAB` memory:

- the dimensional timestamp `timers` (in years),
- the numbers of grid points `nr=1248` in radius, `nt=256` in latitude and `np=512` in longitude, with longitude `np=1` referring to 180 degrees East in the Pacific.
- the vectors `r(1:nr)` of radii within the outer core (in km), `theta(1:nt)` of latitudes and `phi(1:np)` of longitudes (both in radians) defining the spherical coordinate frame,
- the three `(1:np,1:nt,1:nr)` arrays `Vr,Vt,Vp` of the outer core velocity field components (in km/yr),
- the three `(1:np,1:nt,1:nr)` arrays `Br,Bt,Bp` of the outer core magnetic field components (in mT),
- the `(1:np,1:nt,1:nr)` array `T` of the outer core scalar density anomaly field (in $\mathrm{kg/m}^3$).

Bibliography

Aubert J (2018) Geomagnetic acceleration and rapid hydromagnetic wave dynamics in advanced numerical simulations of the geodynamo. Geophys J Int 214(1):531–547

Aubert J (2020) Recent geomagnetic variations and the force balance in Earth's core. Geophys J Int DOI 10.1093/gji/ggaa007, doi: 10.1093/gji/ggaa007

Aubert J, Finlay CC (2019) Geomagnetic jerks and rapid hydromagnetic waves focusing at Earth's core surface. Nature Geosci 12(5):393–398, DOI 10.1038/s41561-019-0355-1

Aubert J, Gillet N (2021) The interplay of fast waves and slow convection in geodynamo simulations nearing earth‚Äôs core conditions. Geophys J Int DOI https://doi.org/10.1093/gji/ggab054

Aubert J, Gastine T, Fournier A (2017) Spherical convective dynamos in the rapidly rotating asymptotic regime. J Fluid Mech 813:558–593

2.4 Re-analysis of magnetic data under spatio-temporal dynamo constraints

4DEarth_Swarm_Core ESA project deliverables D-D.1 and R-D.1

N. Gillet, M. Istas, T. Schwaiger
ISTerre Grenoble

2.4.1 Introduction

The core surface flow re-analyses presented below are based on the inversion scheme developed by Gillet et al (2019), namely an augmented state ensemble Kalman filter. This algorithm has been implemented into the `pygeodyn` software (Huder et al, 2019). The forward model is based on spatio-temporal cross-covariances (extracted from geodynamo data series) of the flow, the radial magnetic field, and the unresolved induction at the core surface. It consists of a multivariate auto-regressive model of order 1 (AR-1). At each epoch t, these quantities are described through vectors (respectively $\mathbf{u}(t)$, $\mathbf{b}(t)$ and $\mathbf{e}(t)$) that contain the spherical harmonic representation of the fields. The main modifications, in comparison to previously published re-analyses, are the following:

- We consider here a priori cross-covariances from the 71%-path dynamo (Aubert and Gillet, 2021, see D-C.1 data products), which improves the time-scale separation between the turn-over time and the Alfvén time in comparison of the 50%-path dynamo that was previously available (Aubert et al, 2017).

- The re-analysis step of the Kalman filter used into `pygeodyn` has been improved, in particular the estimation of the forecast covariance matrix for the magnetic field. This point, particularly important when re-analyzing GVO data, is addressed in section §2.4.2.

- We consider several sets of magnetic data that allow a reanalysis until 2020: Gauss coefficients data from the COV-OBS-x2 (Huder et al, 2020) and CHAOS-7 (Finlay et al, 2020) field models, and GVO data (Hammer et al, 2021) – see also the D-B.1 data products.

On the one hand, a preliminary analysis of the resulting core flow models is provided in section §2.4.4. It shows hints for propagating flow patterns at sub-decadal periods, which may be interpreted in the framework of QG Alfvén waves of of QG-MC modes. Flow models derived from geomagnetic field models are delivered at

`https://geodyn.univ-grenoble-alpes.fr/`

On the other hand, the reanalysis of GVO data lead us to face an unpredicted difficulty. There remains unmodelled signals that leak into the core field model. We suspect these are mainly from ionospheric origin (i.e. internal to the satellite orbits). Simple pre-processing (filtering) is apparently not enough to erase them. This point is illustrated in section §2.4.3, and we propose a strategy to face this difficulty. We highlight that this issue constitutes a timely research area, as interannual ionospheric field changes are not well documented or understood yet.

Both the inversion of Gauss coefficient field models and of GVO data call for a better handling of some unmodelled signals at interannual time-scales. More detailed analyses of these results will lead to collaborative publications involving colleagues from DTU and IPGP.

2.4.2 Improvements of the core flow inversion scheme

We use the notations $\overline{\mathbf{x}} = E\left[\mathbf{x}\right]$ for the statistical expectation and $\mathsf{P}_{xx} = E\left[\delta\mathbf{x}\delta\mathbf{x}^T\right]$ for the cross-covariance matrix, with $\delta\mathbf{x} = \mathbf{x} - \overline{\mathbf{x}}$.

In the `pygeodyn` software the analysis is performed in 2 steps, first on main field (MF) data to get the Gauss coefficients, then on secular variation (SV) data to get the augmented state (flow and errors of representativeness). So far for the first analysis we considered as the forecast covariance matrix $\mathsf{P}^f_{bb} = E\left[\delta\mathbf{b}^f\delta\mathbf{b}^{f^T}\right]$ the cross-covariance matrix P^*_{bb} obtained from the entire series of available dynamo states (see Gillet et al, 2019). This behaves nicely when using Gauss coefficient data (Barrois et al, 2017), but we noticed that it allows a too large variability at the analysis step when using instead GVO data, inducing strong time changes in the analysed field $\mathbf{b}^a$ when the amount of observational constraints varies through time. This calls for improvements to be brought to the `pygeodyn` software.

We discretise the induction equation between two epochs using an Euler scheme:

$$\mathbf{b}_{t+\Delta t} = \mathbf{b}_t + \Delta t\left(\mathsf{A}_t\mathbf{u}_t + \mathbf{e}_t\right)\,, \tag{2.11}$$

where A_t depends on $\mathbf{b}_t$. If the flow is projected onto principle components (PC), it writes $\mathbf{u}_t = \mathbf{u}_0 + \mathsf{S}\mathbf{v}_t$, with $\mathbf{u}_0$ the background flow and $\mathbf{v}_t$ the PC representation of the flow. Then equation (2.11) becomes

$$\mathbf{b}_{t+\Delta t} = \mathbf{b}_t + \Delta t\left(\mathsf{A}_t\mathbf{u}_0 + \tilde{\mathsf{A}}_t\mathbf{v}_t + \mathbf{e}_t\right)\,, \tag{2.12}$$

with $\tilde{\mathsf{A}}_t = \mathsf{A}_t\mathsf{S}$. We consider N epochs between two analyses ($\Delta t_a = N\Delta t$), so that

$$\mathbf{b}_{t_a+\Delta t_a} = \mathbf{b}_{t_a} + \Delta t\sum_{i=1}^{N}\left(\mathsf{A}_{t_i}\mathbf{u}_0 + \tilde{\mathsf{A}}_{t_i}\mathbf{v}_{t_i} + \mathbf{e}_{t_i}\right)\,, \tag{2.13}$$

with $t_i = t_a + (i-1)\Delta t$. We look for $\mathsf{P}^f_{bb}(t_a + \Delta t_a) = E\left[\delta\mathbf{b}_{t_a+\Delta t_a}\delta\mathbf{b}^T_{t_a+\Delta t_a}\right]$. For the expectation term we make the approximation

$$\overline{\mathsf{A}_t\mathbf{u}_t} \simeq \mathsf{A}_t\overline{\mathbf{u}}_t = \mathsf{A}_t\mathbf{u}_0 + \tilde{\mathsf{A}}_t\overline{\mathbf{v}}_t\,, \tag{2.14}$$

i.e. most of the variability comes from the flow (in comparison with the magnetic field that is best constrained and varies less with time), so that

$$\overline{\mathbf{b}}_{t_a+\Delta t_a} = \overline{\mathbf{b}}_{t_a} + \Delta t\sum_{i=1}^{N}\left(\mathsf{A}_{t_i}\mathbf{u}_0 + \tilde{\mathsf{A}}_{t_i}\overline{\mathbf{v}}_{t_i} + \overline{\mathbf{e}}_{t_i}\right)\,, \tag{2.15}$$

and

$$\mathsf{P}^f_{bb}(t_a+\Delta t_a) = E\left[\left(\delta\mathbf{b}_{t_a} + \Delta t\sum_{i=1}^{N}\left(\tilde{\mathsf{A}}_{t_i}\delta\mathbf{v}_{t_i} + \delta\mathbf{e}_{t_i}\right)\right)\left(\delta\mathbf{b}_{t_a} + \Delta t\sum_{i=1}^{N}\left(\tilde{\mathsf{A}}_{t_i}\delta\mathbf{v}_{t_i} + \delta\mathbf{e}_{t_i}\right)\right)^T\right] \tag{2.16}$$

Considering deviations in $\mathbf{b}_{t_a}$, $\mathbf{e}$ and $\mathbf{u}$ as independent we then obtain

$$\mathsf{P}^f_{bb}(t_a+\Delta t_a) = \mathsf{P}^a_{bb}(t_a) + \Delta t^2\sum_{i=1}^{N}\sum_{j=1}^{N}\left(\tilde{\mathsf{A}}_{t_i}E\left[\delta\mathbf{v}_{t_i}\delta\mathbf{v}^T_{t_j}\right]\tilde{\mathsf{A}}^T_{t_j} + E\left[\delta\mathbf{e}_{t_i}\delta\mathbf{e}^T_{t_j}\right]\right)\,, \tag{2.17}$$

with $\mathsf{P}^a_{xx} = E\left[\delta\mathbf{x}^a_{t_a}\delta\mathbf{x}^{a\,T}_{t_a}\right]$ an analysis covariance matrix. On time increments short in front of the typical time-scales of the drift matrices for **v** and **e** (i.e. $\Delta t_a \ll 1/\lambda_{v,e}$, with $\lambda_{v,e}$ the eigen-values of the drift matrices), we have $\delta\mathbf{v}_{t_1} = \delta\mathbf{v}_{t_a}$ and

$$\text{for } i \geq 2,\ \delta\mathbf{v}_{t_i} \simeq \delta\mathbf{v}_{t_a} + \sqrt{\Delta t}\sum_{k=1}^{i-1}\mathbf{r}_{vk}\,. \tag{2.18}$$

$\mathbf{r}_v$ is the random forcing term that enters the AR-1 equation for **v** (i.e. most of the short term dispersion on the flow trajectories comes from the random walk term). A similar expression holds for $\delta\mathbf{e}_i$. Then

$$\begin{aligned} E\left[\delta\mathbf{v}_{t_1}\delta\mathbf{v}^T_{t_j}\right] &= \mathsf{P}^a_{vv}(t_a)\,, \\ \text{for both } i \text{ and } j \geq 2,\quad E\left[\delta\mathbf{v}_{t_i}\delta\mathbf{v}^T_{t_j}\right] &= \mathsf{P}^a_{vv}(t_a) + \Delta t\sum_{k=1}^{i-1}\sum_{k'=1}^{j-1}E\left[\mathbf{r}_{vk}\mathbf{r}_{vk'}\right]. \end{aligned} \tag{2.19}$$

Since $E\left[\mathbf{r}_{vk}\mathbf{r}_{vk'}\right] = \mathsf{P}_{rrv}\delta_{kk'}$, this last relation gives

$$\text{for both } i \text{ and } j \geq 2,\ E\left[\delta\mathbf{v}_{t_i}\delta\mathbf{v}^T_{t_j}\right] = \mathsf{P}^a_{vv}(t_a) + \Delta t\mathsf{P}_{rrv}\min(i-1, j-1)\,. \tag{2.20}$$

We now approximate A_t as being constant between two analyses (most of the time changes come from **v** and **e**). Using the relation

$$\sum_{i=2}^{N}\sum_{j=2}^{N}\min(i-1, j-1) = \frac{N}{6} - \frac{N^2}{2} + \frac{N^3}{3}\,, \tag{2.21}$$

and $N\Delta t = \Delta t_a$, equation (2.17) then becomes

$$\begin{aligned}\mathsf{P}^f_{bb}(t_a + \Delta t_a) \simeq \quad & \mathsf{P}^a_{bb}(t_a) + \Delta t_a^2 \left[\tilde{\mathsf{A}}_{t_a} \mathsf{P}^a_{vv}(t_a) \tilde{\mathsf{A}}^T_{t_a} + \mathsf{P}^a_{ee}(t_a)\right] \\ & + \frac{\Delta t_a^3}{3} \left(1 - \frac{3}{2N} + \frac{1}{2N^2}\right) \left[\tilde{\mathsf{A}}_{t_a} \mathsf{P}_{rrv} \tilde{\mathsf{A}}^T_{t_a} + \mathsf{P}_{rre}\right] . \end{aligned} \tag{2.22}$$

In a case with no uncertainty on the previous analysis state, the dispersion within the ensemble of $\mathbf{b}^f$ evolves $\propto \Delta t^{3/2}$ – from the last term in equation (2.22). Otherwise, if the dispersion in the fields $\mathbf{u}^a(t_a)$ and $\mathbf{e}^a(t_a)$ is important, the second term in (2.22) will dominate for short increments Δt_a, and the dispersion in $\mathbf{b}^f$ will evolve $\propto \Delta t$.

This new formulation has been introduced into `pygeodyn`, with some prerequisit:

- For calculating A_{t_a} in equation (2.22) we consider for the sake of simplicity $\mathsf{A}(\overline{\mathbf{b}}^a(t_a))$, where $\overline{\mathbf{b}}^a$ is the ensemble average of the MF analysis states – i.e. we consider that the MF does not evolves much between two analyses.

- To proceed with equation (2.22) at the 1st analysis step, the matrix P^a_{bb} must be initialized. A simple way would be to start with the dynamo prior P^*_{bb}, but this may generate large off-sets between the first analyses from the field model and from the GVO. The posterior covariance matrix P^a_{bb} after analysing a field model (warm-up) seems a more appealing choice. For the sake of simplicity, this P^a_{bb} is approximated as a diagonal matrix, with diagonal elements carrying the variance of the spread within the ensemble of $\mathbf{b}^a$ (from the warm-up) at the start time of the GVO re-analysis.

- As the ensemble size is not large enough to constrain well all off-diagonal terms of P^a_{bb}, we will consider only the diagonal elements of the empirically estimated P^a_{bb}. Similarly off-diagonal terms in P^a_{vv} and P^a_{ee} are considered as negligeable (which appears to be approximately true in practice).

- Equation (2.22) supposes that an analysis is performed every Δt_a. In some situations, the MF is not analysed at some analysis epochs (e.g. absence of GVO data between CHAMP and Swarm, or after Swarm, before CHAMP, etc.). We then replace in (2.22) Δt_a by $k\Delta t_a$, with k the number of analysis periods between two MF analyses.

An example of the effect of considering this new covariance matrix when considering GVO data is shown in Figure 2.4.2. In the next sections, the new implementation including equation (2.22) will be considered.

2.4.3 On the need for a more accurate processing of GVO data

Preliminary re-analyses using annual differences of 4-monthly means GVO as SV data show strong oscillations of the magnetic field field Gauss coefficients. We

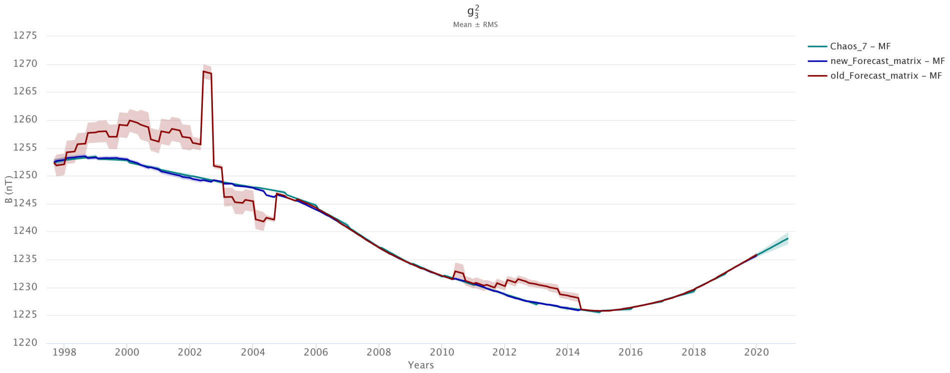

Figure 2.10: Impact of the use of the new derivation of P_{bb}^{f} on the Gauss coefficient g_3^2, for a re-analysis of GVO data from 1998 to 2020. In blue when using equation (2.22), in red with the ancient implementation (with the full dynamo covariances), and in Cyan with the CHAOS-7 model.

consider these are likely due to unmodelled ionospheric contributions, in particular because they mainly affect spherical harmonic orders $m = 0$ and $m = 1$ (see Figure 2.4.3, top). They subsequently imply spurious fluctuations in the core flow coefficients (Figure 2.4.3, middle). We do not know precisely down to which period observed field changes are mainly from internal origin.

As a first try to get around this difficulty, we built every 4 month sliding annual means from the 4-monthly GVO series. For all three components we then consider

$$\overline{Y}(t) = \frac{Y(t-1/2)}{6} + \frac{Y(t-1/6)}{3} + \frac{Y(t+1/6)}{3} + \frac{Y(t+1/2)}{6}, \tag{2.23}$$

where the time t is in years. This constitutes the filtered MF datasets, from which SV data are built every 4 months as centered differences of MF annual means:

$$\begin{aligned} \frac{d\overline{Y}}{dt}(t) = & \quad \overline{Y}(t+1/3) - \overline{Y}(t-1/3) \\ = & \quad \frac{Y(t+1/2) - Y(t-1/2)}{2} + \frac{Y(t+1/6) - Y(t-1/6)}{4} \\ & + \frac{Y(t+5/6) - Y(t-5/6)}{4} . \end{aligned} \tag{2.24}$$

Our preliminary analysis using `pygeodyn` shows that if oscillations of periods shorter than 2 years (the Niquyst frequency with annual data) are indeed filtered out, we see significant signals of period $\approx 3-4$ years that are not seen in CHAOS-7, and which induce large oscillations in core flow coefficients. These are unlikely realistic as they induce ways too large changes in the LOD (Figure 2.4.3, bottom).

We conclude for now that probably there remain unmodelled signals in the GVO datasets, internal to the satellites, which project onto the core field model. We favor a ionospheric source, as fields iunduced in the mantle are likely much

Figure 2.11: Re-analyses of the core-surface flow and magnetic field from 1998 to 2020, using several datasets: CHAOS-7 Gauss coefficients (cyan), 4-monthly GVO data (red) and annual means of 4-monthly GVO data (blue). top: SV coefficient g_8^1; middle: flow coefficient t_3^0; bottom: associated length-of-day (LOD) variations.

weaker for realistic Q-responses (e.g. Olsen, 1999). This precludes for now the investigation of core flow changes from GVO on periods shorter than 3-4 years. This unforeseen effect calls for further investigations of these signals, which shall be carried out in collaboration with DTU. A first simple solution to this issue has been investigated: we mapped core surface flows without accounting for data at high latitudes (or only considering Z data). It however led to similar results. We highlight that there has been so far very few studies of interannual changes of the ionospheric field. These are neither well mapped nor understood.

The next step will consist of jointly inverting from GVO data the core field plus a source at an altitude representative of the ionosphere (see Ropp et al, 2020). Given the geometry of the target, for these extra model parameters we will design the prior covariance matrix so as to favor near-zonal coefficients (i.e. spherical harmonic orders $m = 0$ and $m = 1$). As there will necessarily be ambiguities between the two sources, we will start with a study of the sensitivity to the prior information added on the ionospheric field model. We are also currently implementing into `pygeodyn` the use of robust norms (instead of L2) for the measure of the misfit to GVO data (Farquharson and Oldenburg, 1998). This should help reduce the sensitivity of the internal field model to irregular external fields.

2.4.4 Core flow re-analyses from Gauss coefficient geomagnetic observations

The models illustrated below have been inverted from Gauss coefficient data of the COV-OBS.x2 and CHAOS-7 field models. In order to compare with an independent field model constructed upon an alternative method (the correlation-based approach, see Holschneider et al, 2016), we also use data from the MCM field model of Ropp et al (2020). The latter two inversion have been warmed-up using COV-OBS.x2 data prior to 1999.

The slowly varying flow models are very similar to previous estimates, showing the westward gyre largely documented over the past years (e.g. Pais and Jault, 2008; Gillet et al, 2009; Aubert, 2014; Gillet et al, 2019). We thus focus here on interannual flow changes, for which the extension of the satellite era to at least 2020 offers a better constraint. Based on the above observation on ambiguous field changes of 2-3 yr periods, we show below flow models band-pass filtered between 4 and 9.5 years, using a Butterworth filter of order 4. We remind that the temporal spectrum of core flows shows more power towards short period, so that there exists decadal changes with intensities larger than what is reported below.

A preliminary analysis over the satellite era confirms some previous findings by Gillet et al (2019). In particular, focusing on sub-decadal flow changes, we see that the most intense dynamics takes place within the equatorial belt, with interannual velocities as large as 5 km/yr (Gillet et al, 2015; Finlay et al, 2016; Kloss and Finlay, 2019). Meanwhile, the accumulation of high quality satellite data through time allows a closer look at transient phenomena.

Our new models now covering over 20 yr of satellite data, we are able to more clearly isolate azimuthal flow patterns around the equator, with a periodicity of ≈ 7 yr. These features are seen from all three magnetic field models, with a reasonable coherence within the flow solutions – even though with MCM some more spatial compexity is observed, in particular in the Eastern hemisphere. The flow patterns seem to propagate Westward, starting from below the Greenwhich meridian to ≈ 150°E (see Figure 2.12). This would correspond to one circulation around the equator in about 14 yrs, i.e. a speed of ∼ 1500 km/yr at the core surface.

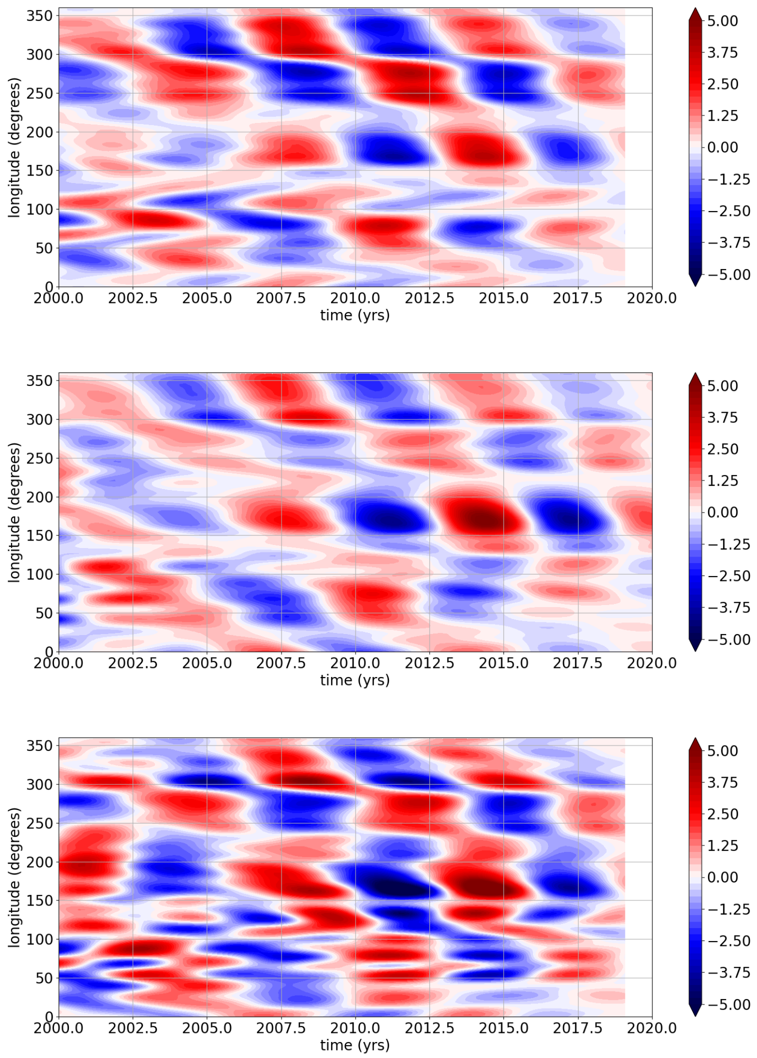

Figure 2.12: Time-longitude diagram of the azimuthal velocity (in km/yr) at the equator over 2000-2020, filtered at subdecadal periods, for the re-analysed core surface flow models over from Gauss coefficients of the MCM (bottom), CHAOS-7 (middle) and COV-OBS.x2 (top) field models.

Meanwhile, the equatorial belt is the area of the core surface the better covered by magnetic data. Furthermore, it is less sensitive to the complex separation of magnetic sources at high latitudes. Indeed, the coherence between the three flow models seems less when looking away from the equator. We show in Figures 2.13 and 2.14 time-latitude diagrams of the band-pass filtered ortho-radial and azimuthal velocities for longitudes 180°E and 90°E. For all three models, these transient flows are predominantly equatorially symmetric. Away from the equator, motions are somewhat less intense when inverted from the CHAOS-7 model, in comparison with COV-OB-x2 and MCM. This may be related to the stronger damping applied on near zonal Gauss coefficients used when building the CHAOS-7 model. In some occurences, there is some hint of latitudinal propagation of flow patterns from several field models, as for instance towards the equator (resp. the poles) on u_θ (resp. u_ϕ) at 90°E (although we cannot exclude an artificial effect of the filtering). These signals reach the tangent cylinder from the core equator (and vice-versa) in about 5 years, corresponding to a speed of $\approx$ 800 km/yr at the core surface. We emphasize that interannual motions are not restricted to the Atlantic hemisphere; strong transient flows also show up in the Pacific hemisphere (see also Barrois et al, 2018).

The speeds and time-scales estimated above are commensurate with the Alfvén speed $V_A = B/\sqrt{\rho\mu}$, which spans 800 to 1400 km/yr for a magnetic field intensity $B \in [3, 5]$ mT. It is thus tempting to interprete the features documented here in the framework of QG Alfvén waves (Aubert and Finlay, 2019; Aubert and Gillet, 2021), and of propagating interannual QG-MC modes (Gerick et al, 2021). The former propagate mainly in the cylindrical radial direction in the path geodynamo simulations (although some Westward propagation has also been detected in some rare events, when the magnetic field configuration is appropriate for this). The latter propose a natural set of Wetsward propagating modes. However, if combined to one another in an out-of-phase manner, they may also give rise to propagation in the ortho-radial direction at the CMB.

Bibliography

Aubert J (2014) Earth's core internal dynamics 1840–2010 imaged by inverse geodynamo modelling. Geophys J Int 197(3):1321–1334

Aubert J, Finlay CC (2019) Geomagnetic jerks and rapid hydromagnetic waves focusing at Earth's core surface. Nature Geosci 12(5):393–398, DOI 10.1038/s41561-019-0355-1

Aubert J, Gillet N (2021) The interplay of fast waves and slow convection in geodynamo simulations nearing earth,Äôs core conditions. Geophys J Int DOI https://doi.org/10.1093/gji/ggab054

Aubert J, Gastine T, Fournier A (2017) Spherical convective dynamos in the rapidly rotating asymptotic regime. J Fluid Mech 813:558–593

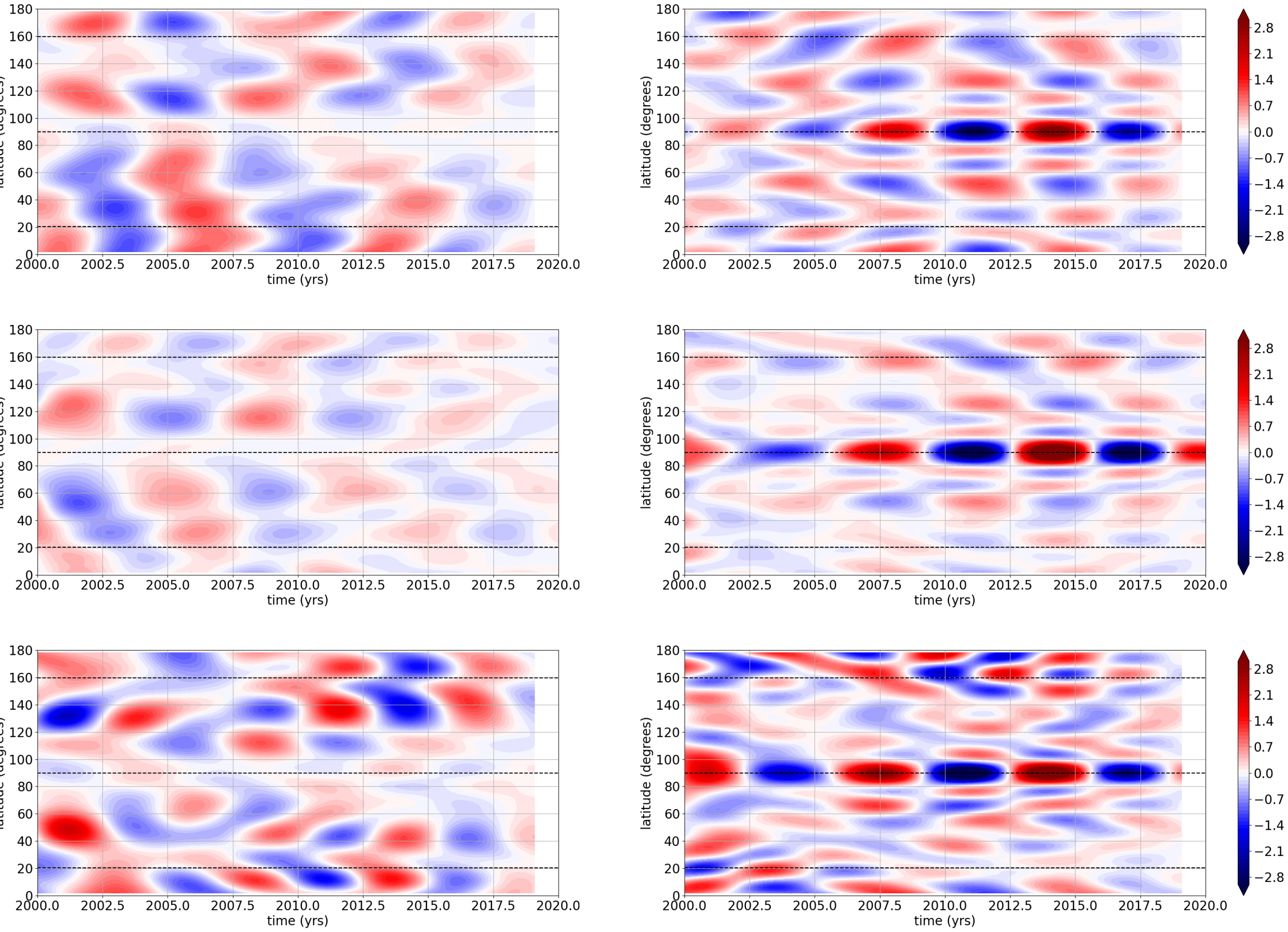

Figure 2.13: Time-latitude diagram of the orthoradial (left) and azimuthal (right) velocities (in km/yr) at 180°E over 2000-2020, filtered at subdecadal periods, for the re-analysed core surface flow models over from Gauss coefficients of the MCM (bottom), CHAOS-7 (middle) and COV-OBS.x2 (top) field models.

Barrois O, Gillet N, Aubert J (2017) Contributions to the geomagnetic secular variation from a reanalysis of core surface dynamics. Geophys J Int 211(1):50–68

Barrois O, Hammer M, Finlay C, Martin Y, Gillet N (2018) Assimilation of ground and satellite magnetic measurements: inference of core surface magnetic and velocity field changes. Geophysical Journal International 215(1):695–712

Farquharson CG, Oldenburg DW (1998) Non-linear inversion using general mea-

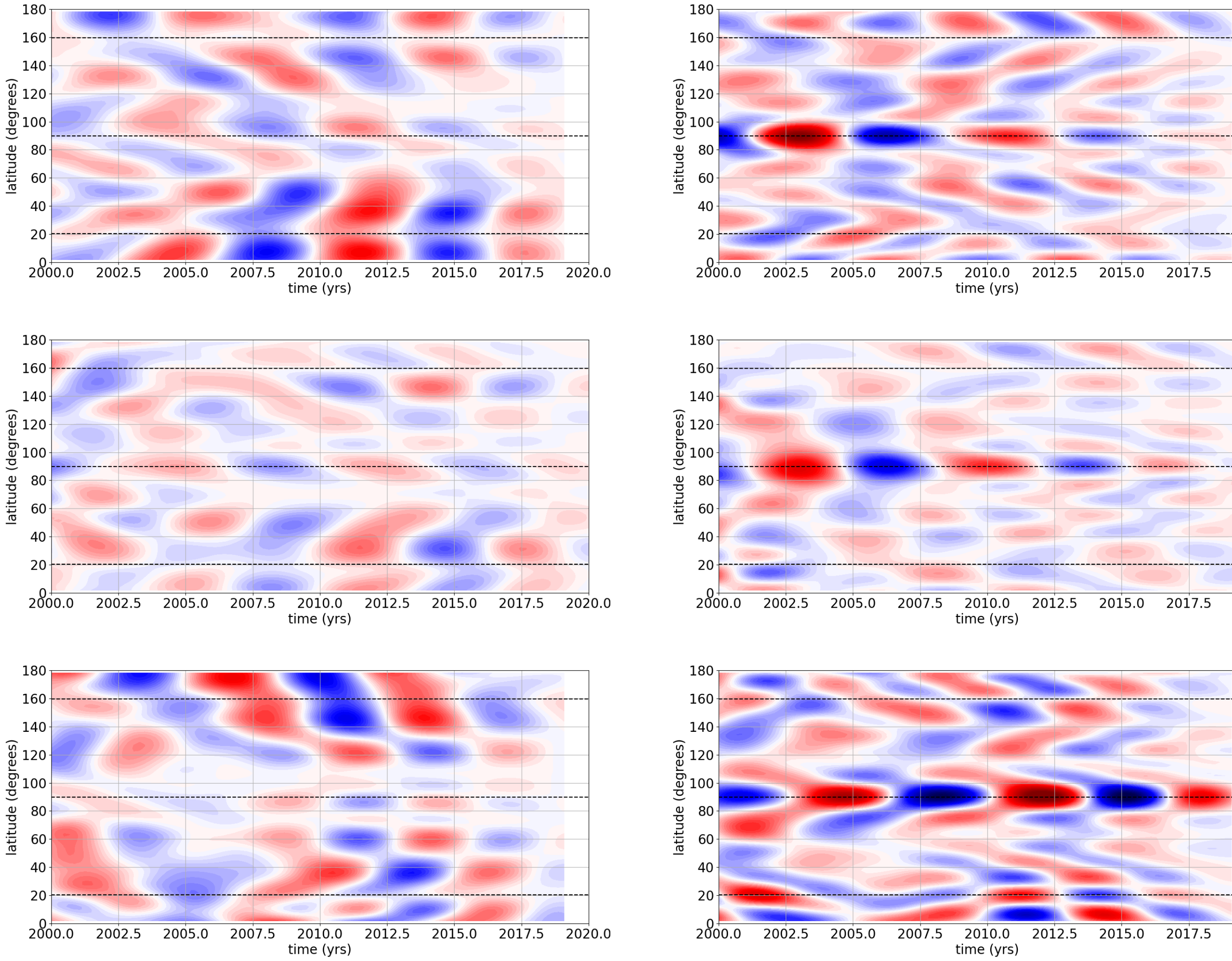

Figure 2.14: Time-latitude diagram of the orthoradial (left) and azimuthal (right) velocities (in km/yr) at 90°E over 2000-2020, filtered at subdecadal periods, for the re-analysed core surface flow models over from Gauss coefficients of the MCM (bottom), CHAOS-7 (middle) and COV-OBS.x2 (top) field models.

sures of data misfit and model structure. Geophysical Journal International 134(1):213–227

Finlay CC, Olsen N, Kotsiaros S, Gillet N, Tøffner-Clausen L (2016) Recent geomagnetic secular variation from Swarm. Earth, Planets and Space 68(1):1–18

Finlay CC, Kloss C, Olsen N, Hammer MD, Tøffner-Clausen L, Grayver A, Kuvshinov A (2020) The chaos-7 geomagnetic field model and observed changes in the south atlantic anomaly. Earth, Planets and Space 72(1):1–31

Gerick F, Jault D, Noir J (2021) Fast quasi-geostrophic magneto-coriolis modes in the earth’s core. Geophys Res Lett p 2020GL090803

Gillet N, Pais M, Jault D (2009) Ensemble inversion of time-dependent core flow models. Geochemistry, Geophysics, Geosystems 10(6)

Gillet N, Jault D, Finlay C (2015) Planetary gyre, time-dependent eddies, torsional waves, and equatorial jets at the earth’s core surface. Journal of Geophysical Research: Solid Earth 120(6):3991–4013

Gillet N, Huder L, Aubert J (2019) A reduced stochastic model of core surface dynamics based on geodynamo simulations. Geophys J Int 219(1):522–539

Hammer MD, Cox GA, Brown WJ, Beggan CD, Finlay CC (2021) Geomagnetic virtual observatories: monitoring geomagnetic secular variation with the swarm satellites. Earth, Planets and Space 73(1):1–22

Holschneider M, Lesur V, Mauerberger S, Baerenzung J (2016) Correlation-based modeling and separation of geomagnetic field components. J Geophys Res: Solid Earth 121(5):3142–3160

Huder L, Gillet N, Thollard F (2019) pygeodyn 1.1. 0: a python package for geomagnetic data assimilation. Geoscientific Model Development 12(8):3795–3803

Huder L, Gillet N, Finlay CC, Hammer MD, Tchoungui H (2020) Cov-obs.x2: 180 years of geomagnetic field evolution from ground-based and satellite observations. Earth, Planets and Space 72(1):1–18

Kloss C, Finlay CC (2019) Time-dependent low-latitude core flow and geomagnetic field acceleration pulses. Geophysical Journal International 217(1):140–168

Olsen N (1999) Induction studies with satellite data. Surveys in Geophysics 20(3):309–340

Pais M, Jault D (2008) Quasi-geostrophic flows responsible for the secular variation of the Earth’s magnetic field. Geophys J Int 173(2):421–443

Ropp G, Lesur V, Baerenzung J, Holschneider M (2020) Sequential modelling of the earth,Äôs core magnetic field. Earth, Planets and Space 72(1):1–15

Chapter 3

Analysis of the rapid field changes

3.1 QG-MAC inversion scheme from 3D simulations

4DEarth_Swarm_Core ESA project deliverable R-C.1

J. Aubert
IPG Paris

This deliverable is contained in the following publication: J. Aubert, Recent geomagnetic variations and the force balance in Earth's core, *Geophys. J. Int.*, 221(1), 2020, 378–393, https://doi.org/10.1093/gji/ggaa007

abstract:

The nature of the force balance that governs the geodynamo is debated. Recent theoretical analyses and numerical simulations support a quasigeotrophic (QG), magneto-Archimedes-Coriolis (MAC) balance in Earth's core, where the Coriolis and pressure forces equilibrate at leading order in amplitude, and where the buoyancy, Lorentz and ageostrophic Coriolis forces equilibrate at the next order. In contrast, earlier theoretical expectations have favoured a magnetostrophic regime where the Lorentz force would reach leading order at the system scale. The dominant driver (buoyant or magnetic) for the general circulation in Earth's core is equally debated. In this study, these questions are explored in the light of the high-quality geomagnetic data recently acquired by satellites and at magnetic ground observatories. The analysis involves inverse geodynamo modelling, a method that uses multivariate statistics extracted from a numerical geodynamo model to infer the state of Earth's core from a geomagnetic field model interpretation of the main field and secular variation data. To test the QG-MAC dynamic hypothesis against the data, the framework is extended in order to explicitly prescribe this force balance into the inverse problem solved at the core surface. The resulting inverse solutions achieve a quantitatively adequate fit to the data while ensuring deviations from the QG-MAC balance (which amount to an inertial driving of the flow) lower than each of the leading forces. The general circulation imaged within the core over the past two decades confirms the existence of a planetary-scale, eccentric, axially columnar gyre that comprises an intense, equatorially symmetric jet at high latitudes in the Pacific hemisphere. The dominant driver of this circulation is shown to be of buoyant nature, through a thermal wind balance with a longitudinally hemispheric buoyancy anomaly distribution. Geomagnetic forecasts initiated with the inverted core states are systematically more accurate against the true interannual geomagnetic field evolution when enforcing the QG-MAC constraint. This force balance is therefore consistent with the geomagnetic data at the large scales of Earth's core that can be imaged by the method.

3.2 Stochastic reanalysis of core surface flow motions

4DEarth_Swarm_Core ESA project deliverable R-D.1

N. Gillet[1], F. Gerick[2], D. Jault[1], T. Schwaiger[1], J. Aubert[3] & M. Istas[1]
[1]ISTerre Grenoble, [2] Royal Observatory of Belgium, [2]IPG Paris

This deliverable is contained in the following publication: N. Gillet, F. Gerick, D. Jault, T. Schwaiger, J. Aubert & M. Istas, Satellite magnetic data reveal interannual modes in Earth's core, *in revision at Proc. Natl. Acad. Sci. USA*

abstract:

The Earth magnetic field displays variations on a broad range of time scales from years to hundreds of millions of years. The last two decades of global and continuous satellite geomagnetic field monitoring have considerably enriched the knowledge on the rapid physical processes taking place in the Earth,Äôs outer core. Identification of axisymmetric torsional Alfvén waves with subdecadal periods from observatory and satellite data has given access to an averaged intensity of the magnetic field in the Earth's core interior. A significant part of the rapid signal, however, resides in non-axisymmetric motions. Their origin has remained elusive as previous studies of magnetohydrodynamic waves in the Earth's core mainly focused on their possible signature on centennial time scales. Here, we identify non-axisymmetric wavelike patterns in the equatorial region of the core surface from the observed geomagnetic variations. These wavelike features have large spatial scales, interannual periods in the vicinity of 7 years, amplitudes reaching 3 km/yr and coherent westward drift at phase speeds of about 1500 km/yr. We interpret and model these flows as the signature of Magneto-Coriolis (MC) modes. Their identification offers a way to probe the magnetic field structure inside Earth,Äôs core. It follows from our work that there is no need for a stratified layer at the top of the core to account for the rapid geomagnetic field changes.

3.3 A catalogue of simulated jerks from a geodynamo model approaching Earth's core conditions: preliminary analysis

4DEarth_Swarm_Core ESA project deliverable R-E.1

J. Aubert
IPG Paris

3.3.1 Introduction

This document presents a preliminary analysis of 14 notable jerk events selected in deliverable D-C.1 (Long time series of outputs from a geodynamo model approaching Earth's core conditions), the high-resolution output data from which has been made available in D-E.1 (A catalogue of simulated jerks from a geodynamo model approaching Earth's core conditions). Both deliverables can be found at https://4d-earth-swarm.univ-grenoble-alpes.fr/data or http://www.ipgp.fr/~aubert/4dearth. The analysis presented here will serve as a basis for a collaborative study to be submitted to *Geophysical Journal International* in the first half of 2022.

3.3.2 The 71% of path model sequence

The '71% of path' or 71p model is a numerical simulation of the geodynamo that is currently the closest to the physical conditions of Earth's core, regarding the realism and relative separation of four key time scales in this system: the magnetic diffusion time $\tau_\eta = D^2/\eta = 135000$ yr, the core overturn time $\tau_U = D/U = 119$ yr, the Alfvén time $\tau_A = D\sqrt{\rho\mu}/B = 5.8$ yr and the rotational time $2\pi\tau_\Omega = 2\pi/\Omega = 11.8$ days. Here $D = 2260$ km is the core thickness, η is the magnetic diffusivity, U and B are characteristic velocity and magnetic field amplitudes in the core, $\rho = 11000\ \mathrm{kg/m^3}$ is the reference core density $\mu = 4\pi.10^{-7}$ H/m is the vacuum magnetic permeability, and Ω is the rotation rate of the Earth. Full details about the model set-up and the extracted data can be found in Aubert and Gillet (2021). A number of definitions are recalled here for clarity.

We use a set of spherical coordinates (r, θ, φ) with unit vectors $\mathbf{e}_r, \mathbf{e}_\theta, \mathbf{e}_\varphi$. The inner core is a sphere of radius $r_i = 1220$ km. The outer core is a spherical shell between radii r_i and $r_o = 3485$ km, this latter radii being that of the core-mantle boundary (CMB). The Earth surface is located at radius $r_\mathrm{E} = 1.83 r_o$. Within the core, we define the velocity, magnetic field vectors and convective density anomaly scalars as $\mathbf{u}$, $\mathbf{B}$ and C. The first derivative with time t of the velocity field is the flow acceleration $\dot{\mathbf{u}} = \partial\mathbf{u}/\partial t$. The first and second time derivatives of the magnetic field are the secular variation (SV) $\dot{\mathbf{B}} = \partial\mathbf{B}/\partial t$ and acceleration (SA) $\ddot{\mathbf{B}} = \partial^2\mathbf{B}/\partial t^2$.

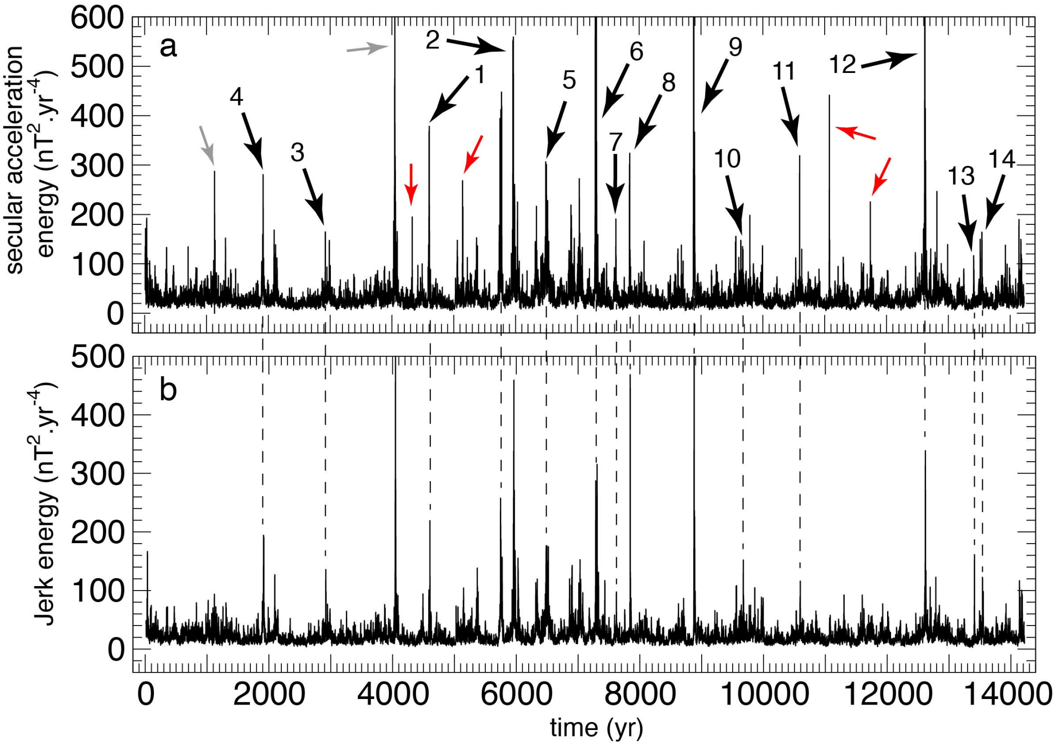

Figure 3.1: Earth secular acceleration energy E_{SA} (top) and jerk energy E_J (bottom), as functions of the dimensional simulation time. Numbered black arrows locate the 14 jerks analysed here. Red arrows locate jerks that have not been selected because they occur too fast to be discernable once the 3-year moving averaging is performed to compute E_J. Grey arrows locate numerical artifacts that have also been discarded in our selection.

Geomagnetic jerks are characterised with the help of the Earth-surface SA energy

$$E_{\mathrm{SA}}(t) = \frac{1}{S_{\mathrm{E}}} \int_{S_{\mathrm{E}}} \ddot{\mathbf{B}}^2(r_{\mathrm{E}}, \theta, \varphi, t)\, \mathrm{d}S, \tag{3.1}$$

where S_{E} is Earth surface at radius r_{E}, and the jerk energy (Aubert and Finlay, 2019)

$$E_{\mathrm{J}}(t) = \frac{1}{S_{\mathrm{E}}} \int_{S_{\mathrm{E}}} \left(\left[\ddot{\mathbf{B}}\right]_t^{t+\Delta t} - \left[\ddot{\mathbf{B}}\right]_{t-\Delta t}^{t} \right)^2 \mathrm{d}S, \tag{3.2}$$

where the square brackets stand for time averaging and $\Delta t = 3$ yr is a running averaging time meant to simulate the typical temporal resolution of satellite measurements of the geomagnetic acceleration (Aubert and Finlay, 2019). To compute these two quantities, the magnetic field is retained up to spherical harmonic degree and order 13, which captures most of the energy at Earth's surface. Figure 3.1 presents the time series of E_{SA} and E_{J} during the model run. An observable jerk is characterised by two rapid and simultaneous intensity surges in the quantities E_{SA} and E_{J}. This ensures that there is a step change in the secular acceleration that significantly exceeds the regular levels of this acceleration (the classical definition of a geomagnetic jerk), and that the secular acceleration itself also exceeds its typical level (as is the case for jerks in the satellite era). A set of 14 jerk events have been selected that way, containing events at least of typical satellite-era strength (i.e. $E_{\mathrm{J}} \sim 100\ \mathrm{nT}^2.\mathrm{yr}^{-4}$) as well as significantly stronger events. Events creating a SA pulse but no discernable pulse in E_{J} have been discarded because they would not correspond to observable events given the current temporal resolution of geomagnetic field monitoring. Events corresponding to numerical artefacts (change of time step or other numerical instability) have also been discarded.

3.3.3 Diagnostics

Table 3.1 summarises a set of quantitative and qualitative diagnostics obtained from examination of the model time series, described below:

- # is the jerk reference number, followed by its timestamp in the simulation.
- Duration is an approximate event duration based on observation of time series of E_{SA}.
- Lat. is the latitude at which focused SA pulses are found at the CMB, on a representation of radial SA up to spherical harmonic degree 13. 'high' means latitudes above 45 degrees, 'mid' means latitudes between 20 and 45 degrees, and low means latitudes below 20 degrees. The latitude distribution of the 14 selected jerk events is representative of the long-term distribution in the 71p model (Aubert and Gillet, 2021).
- Region provides the longitudinal localisation of SA pulses at the Earth surface during the event. The event is qualified as a multiple event in space

Table 3.1: Diagnostics of simulated jerks events 1-14 from the 71p model, of the AF19 event (Aubert and Finlay, 2019). See text for details. Owing to its complexity, event 5 is subdivided into three phases.

#	Time (yr)	Duration (yr)	Lat.	Region	Multi. (time)	Globality (%)	Drift	Trigger	W/C	$E_{\mathrm{J}}^{\max}$ $\left(\mathrm{nT}^2.\mathrm{yr}^{-2}\right)$	$\frac{E_{\mathrm{J}}^{\max}}{E_{\mathrm{SA}}^{\max}}$	SVS	MFS	LOD
1	4605	50	low	India	Y	56		DP, FE	1.6	232	0.56	1.0	1.2	
2	5750	60	low	India, America	Y	61	W	SC, FE	1.2	282	0.63	1.7	0.7	
3	2920	20	low	Africa, Pacific	Y	45	E/W	DP	1.7	143	0.86	0.3	0.1	
4	1915	30	low	India, Atlantic	Y	39	E/W	DP	2.2	201	0.71	1.0	0.0	
5a	6485		low	Africa			W	DP	1.6	202	0.64	-2.2	0.2	
5b	6500	a-c: 50	high	Antartica	a-c: Y	a-c: 54		SC	0.9	213	0.70	0.2	0.2	
5c	6520		low	India			E/W	SC, FE	1.1	204	0.86	0.6	0.2	
6	7295	40	low	Africa, Pacific	Y	75		SC, FE	1.6	344	0.10	2.9	1.6	Y
7	7620	10	low	India, Atlantic		26	W	SC, FE	1.3	122	0.60	0.3	0.1	
8	7844	20	high	Australia	Y	58		SC	1.2	495	1.49	0.4	0.1	
9	8878	30	low	India, Pacific	Y	70	W	SC, FE	1.3	806	0.28	3.2	1.0	Y
10	9673	20	high	Arctic		48		SC	0.8	162	1.12	-0.7	-0.1	
11	10593	10	mid	Pacific		33		SC, FE	1.5	129	0.39	0.7	0.1	
12	12619	50	low	India, Africa	Y	47		SC, FE	1.0	426	0.59	0.6	0.0	Y
13	13412	10	low	India		33		DP, FE	1.5	171	1.42	0.3	0.0	
14	13543	30	low	India	Y	54		DP	1.8	137	0.83	0.4	-0.2	
AF19		10	low	Africa		51	W	DP	1.9	103	0.88	0.2	0.0	

if there are two or more regions. This can also be mapped at the CMB for verification.

- Multi (time) is a binary qualifaction of whether the event has at least two peaks in E_J overcoming a threshold of 100 $\mathrm{nT}^2.\mathrm{yr}^{-4}$. When 'Y' this generally corresponds to SA changes of alternating polarity, at Earth or core surface. There are generally no multiple alternation in events with a duration shorter than 20 years.

- Globality is a quantitative measure of the visibility of jerks as a 'V-shape' structure in ground-observatory-like SV time series. The 'V-shapes' are characterised by a sudden change in the slope of the SV time series, separating two decadal intervals where the SV is piecewise linear. Globality is presented as a percentage of the surface of the Earth where East-component SV traces indeed present a clear structure of this type. To assess this, we define a local r.m.s Eastward SA based on smoothing with a 20-year moving average

$$SA_\varphi^{20}(\theta,\varphi) = \sqrt{\left[\left([\ddot{\mathbf{B}}\cdot\mathbf{e}_\varphi]_{t-10\text{ yr}}^{t+10\text{ yr}}\right)^2 (r_\mathrm{E},\theta,\varphi,t)\right]_\text{event}}, \tag{3.3}$$

and compare its r.m.s value during the event to maxima of the absolute jerk amplitude also retrieved during the event

$$J_\varphi^{20}(\theta,\varphi) = \max(\text{event})\left(\left|[\ddot{\mathbf{B}}\cdot\mathbf{e}_\varphi]_t^{t+10\text{ yr}} - [\ddot{\mathbf{B}}\cdot\mathbf{e}_\varphi]_{t-10\text{ yr}}^{t}\right|(r_\mathrm{E},\theta,\varphi,t)\right). \tag{3.4}$$

The jerk is deemed to present a distinct 'V-shape' at Earth surface location (θ,φ) if $J_\varphi^{20}(\theta,\varphi) > 3\ SA_\varphi^{20}(\theta,\varphi)$. As we shall see, this criterion also matches direct visual inspection reasonably well.

- Drift is a qualification of the direction (E or W, when present) of a coherent azimuthal drift of structures observed on time-longitude plots of the core surface radial SA up to spherical harmonic degree 9 and after filtering in time with a 3-year moving average. These two filtering steps are meant to mimic the typical spatio-temporal resolution of SA retrieved from satellite geomagnetic measurements.

- Trigger is a categorisation of the physical nature of the trigger of the jerk event. This is obtained in relationship with the W/C quantitative indicator (see next item) and visual inspection of movie sequences for flow acceleration, density anomaly, magnetic field inside the shell. DP stands for emission of QGA/QGMC waves in the cylindrical radial direction from a Deep convective Plume and subsequent propagation towards the CMB at equatorial position. SC stands for Shallow Convection, either as a plume reaching the CMB at low-latitude equatorial position and emitting QGA/QGMC waves close to the surface, or a high-latitude imprint of a deep convection column, where no wave emission is observed. FE stands for a significant small-scale magnetic flux expulsion event at the CMB near the equator that also emits QGA/QGMC waves. The visibility of flux expulsion at large-scale is separately characterised by the diagnostic MFS below.

- W/C is a quantitative indicator of the relative amplitude of the two leading contributors to the SA at the CMB. The magnetic induction equation at the core surface can be broken down according to

$$\ddot{\mathbf{B}} = \nabla \times (\dot{\mathbf{u}} \times \mathbf{B}) + \nabla \times (\mathbf{u} \times \dot{\mathbf{B}}) + \eta \boldsymbol{\Delta}(\dot{\mathbf{B}}), \tag{3.5}$$

  and W/C represents the mean squared ratio over the core surface and during the event of the two inductive radial components of equation (3.5) retained up to spherical harmonic degree 13:

$$\mathrm{W/C} = \frac{\left[\displaystyle\int_{r=r_o} (\nabla \times (\dot{\mathbf{u}} \times \mathbf{B}) \cdot \mathbf{e}_r)^2_{\ell \leq 13} \ \mathrm{d}S\right]_{\mathrm{event}}}{\left[\displaystyle\int_{r=r_o} (\nabla \times (\mathbf{u} \times \dot{\mathbf{B}}) \cdot \mathbf{e}_r)^2_{\ell \leq 13} \ \mathrm{d}S\right]_{\mathrm{event}}}. \tag{3.6}$$

  This quantity is meant to reflect the relative role of waves (W) and convection (C) in the jerk dynamics. Indeed $\dot{\mathbf{u}}$ contains a significant contribution of hydromagnetic waves (Aubert and Gillet, 2021), such that the numerator of equation (3.6) reflects the contribution of waves. Likewise, $\mathbf{u}$ and $\dot{\mathbf{B}}$ are dominated by the convective contribution to velocity and secular variation under the QG-MAC force balance. When $\mathrm{W/C} > 1$, this therefore also indicates an inertial deviation to this QG-MAC balance, while a regular QG-MAC operation of the dynamo usually implies $\mathrm{W/C} \approx 1$ (Aubert, 2018).

- $E_{\mathrm{J}}^{\max}$ is the maximum value of the jerk energy reached during the event.

- $E_{\mathrm{J}}^{\max}/E_{\mathrm{SA}}^{max}$ compares the maximum jerk energy to the maximum energy of SA pulses involved in the event.

- SVS is an indicator of the amplitude of possible surges in the SV associated to the jerk event. The r.m.s. Earth surface SV energy is computed as

$$A_{\mathrm{SV}}(t) = \sqrt{\frac{1}{S_{\mathrm{E}}} \int_{S_{\mathrm{E}}} \dot{\mathbf{B}}^2(r_{\mathrm{E}}, \theta, \varphi, t) \, \mathrm{d}S}, \tag{3.7}$$

  where the magnetic field is again truncated after spherical harmonic degree 13. the quantity SVS is defined as

$$\mathrm{SVS} = \frac{\Delta A_{\mathrm{SV}}}{\mathrm{std}(A_{\mathrm{SV}})}, \tag{3.8}$$

  where ΔA_{SV} is the amplitude variation observed during the event, and $\mathrm{std}(A_{\mathrm{SV}}) = 20.3$ nT/yr is computed for the whole time span of the 71p model.

- MFS is an indicator of the large-scale visibility of possible surges in the core surface magnetic field amplitude i.e. large-scale flux expulsion associated to jerk events. The r.m.s, large-scale core surface magnetic energy is computed as
$$A_{\mathrm{MF}}(t) = \sqrt{\frac{1}{S_{\mathrm{CMB}}} \int_{S_{\mathrm{CMB}}} \mathbf{B}^2(r_o, \theta, \varphi, t)\,\mathrm{d}S}\,, \tag{3.9}$$
where S_{CMB} is the spherical surface of the CMB and the magnetic field is truncated after spherical harmonic degree and order 13. The quantity MFS is defined as
$$\mathrm{MFS} = \frac{\Delta A_{\mathrm{MF}}}{\mathrm{std}(A_{\mathrm{MF}})}, \tag{3.10}$$
where ΔA_{MF} is the amplitude variation observed during the event, and $\mathrm{std}(A_{\mathrm{MF}}) = 0.034$ mT is computed for the whole time span of the 71p model.

- LOD is a binary indicator of whether there is a visible inflexion in the time series of $\mathrm{d(LOD)}/\mathrm{d}t$ at the time of the jerk event (see Aubert and Finlay, 2019), with LOD being the length-of-day variations produced by the 71p model. In the 71p model, the mantle axially rotates at rate Ω_{M} under the influence of the magnetic torque Γ_{M} felt by an insulating layer at its base, and the gravitational torque Γ_{G} exerted by the inner core, according to:
$$I_{\mathrm{M}} \frac{\mathrm{d}\Omega_{\mathrm{M}}}{\mathrm{d}t} = \Gamma_{\mathrm{M}} + \Gamma_{\mathrm{G}}, \tag{3.11}$$
with I_{M} the moment of inertia of the mantle. The corresponding rate of change $\mathrm{d(LOD)}/\mathrm{d}t$ in the length of the day is then
$$\frac{\mathrm{d(LOD)}}{\mathrm{d}t} = -\frac{2\pi}{\Omega^2} \frac{\mathrm{d}\Omega_{\mathrm{M}}}{\mathrm{d}t}, \tag{3.12}$$
The jerk events can cause pulses in $\mathrm{d}^2\Gamma_{\mathrm{M}}/\mathrm{d}t^2$ and hence rapid inflexions in $\mathrm{d(LOD)}/\mathrm{d}t$. The LOD indicator is 'Y' if these pulses exceed the level of $\mathrm{d}^2\Gamma_{\mathrm{G}}/\mathrm{d}t^2$.

3.3.4 Dynamical typology of jerks

Here we perform a first categorisation of jerk events, according to the latitude at which they occur and the role of hydromagnetic waves. A second subcategorisation is constructed for wave-driven jerks according to their dynamical triggers.

3.3.5 Low-latitude, wave-driven vs. high-latitude, convection-driven jerks

Jerk events can be classified according to the latitude at which they produce a SA pulse at the CMB, and the indicator W/C of the relative amplitude of waves and convection. A majority of events (13 out of 16, event 5 being subdivided into three

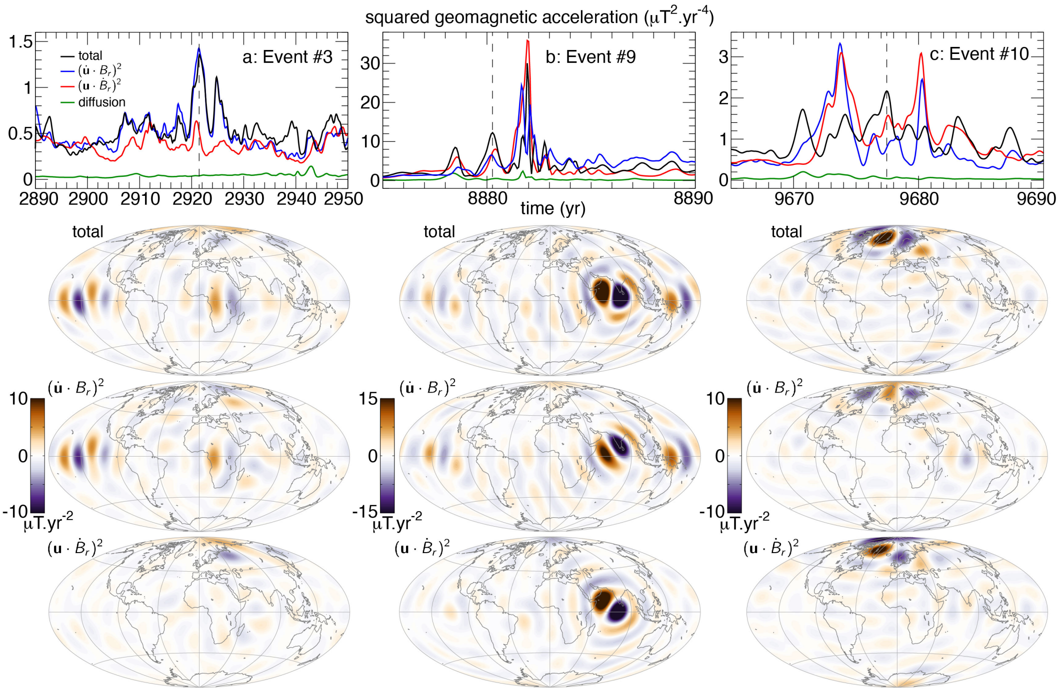

Figure 3.2: Contributors to the radial component of the secular acceleration according to equation (3.5), for the three jerk events 3,9 and 10 (columns a,b,c). Top row: time series of the total mean squared radial secular acceleration at the CMB (black), and of the contributions of the product of $\dot{\mathbf{u}}$ and $\mathbf{B}$ (blue), $\mathbf{u}$ and $\dot{\mathbf{B}}$ (red), and the subdominant magnetic diffusion (green). The vertical dashed line marks the reference time of the highest peak in E_{SA} observed during the event, that also corresponds to the time at which the analysis is carried out in the subsequent rows of the figure. The next rows successively represent hammer projections of the radial secular acceleration at the CMB for the total secular acceleration, contribution of the product of $\dot{\mathbf{u}}$ and $\mathbf{B}$, and of $\mathbf{u}$ and $\dot{\mathbf{B}}$ at this reference time, all truncated after spherical harmonic degree 13.

subevents) occurs at low to mid-latitude at the CMB (see latitude in table 3.1). Most of these events also feature values of W/C that deviate significantly above 1, indicating a primary role of SA induction caused by flow acceleration (or inertia) and a prominent role of hydromagnetic waves. The jerk simulation presented in Aubert and Finlay (2019) belongs to this category (table 3.1). Event 3 on Fig. 3.2a (see also Fig. 3.3 below) with W/C = 1.7 is characteristic of this group, with most of the induction originating from flow acceleration. The shallower event 9 in Fig. 3.2b (see also Fig. 3.4 below) with W/C = 1.3 also features a prominent role of waves but also a more balanced influence from the shallow convection.

The remaining 3 events (5b, 8 and 10) occur at high latitudes and feature values of W/C near or below 1. These belong to a different type where it is rapid convective advection of SV features near the core surface (and not interaction of magnetic field with an accelerating flow) that cause the SA pulses. The trigger of these events is therefore labelled as ’SC’ (Shallow Convection) in table 3.1. These events are fully of convective origin as hydromagnetic waves are not observed and do not appear to be involved in creating the jerk signals. It is expected that this second type of events forms a minority because buoyancy is neutral close to the CMB in the 71p model, and the perturbations there are not expected to primarily come from convection but rather from the energy carried by waves. Also, jerks of convective origin require the simultaneous presence of strong velocities and strong magnetic fields at the same location, which is against the distribution promoted by Lenz’ law in the system (Aubert, 2019). Event 10 in Fig. 3.2c illustrates the distribution of secular acceleration in one of these cases where W/C = 0.8. Here the jerk unfolds within one of the polar vortices, where the strongest core surface velocities are usually found in the 71p model.

3.3.6 Subcategorisation of low-latitude, wave-driven jerks

We now focus on the first and most frequently observed group of jerks, where the event is caused by flow acceleration, with a prominent role of inertia and waves. Values of W/C well in excess of unity also indicate that these jerks occur through a disruption of the QG-MAC balance (e.g. Schwaiger et al, 2019; Aubert and Gillet, 2021) that controls the slow convective evolution of the system. This disruption is necessarily balanced by inertia, which comes at the next level below the QG-MAC forces in the amplitude hierarchy of forces. The disruption can either come from a rapid evolution of the buoyancy, or the Lorentz force, with the Coriolis and pressure forces playing no dynamical trigger role as expected.

When caused by a buoyancy release at depth in the core, the jerk trigger is classified in table 3.1 as ’DP’, for ’Deep Plume’. The jerk simulation in Aubert and Finlay (2019) and event 3 in the present sequence (Fig. 3.3) are two examples of DP jerk events. Fig 3.3a depicts the structure of the buoyancy release near the inner core boundary in event 3, and associated hydromagnetic waves emitted from this boundary to the surface. Quasi-geostrophic Alfvén (QGA) waves are initially emitted at speeds close to the one-dimensional Alfvén speed of 225 km/yr in this

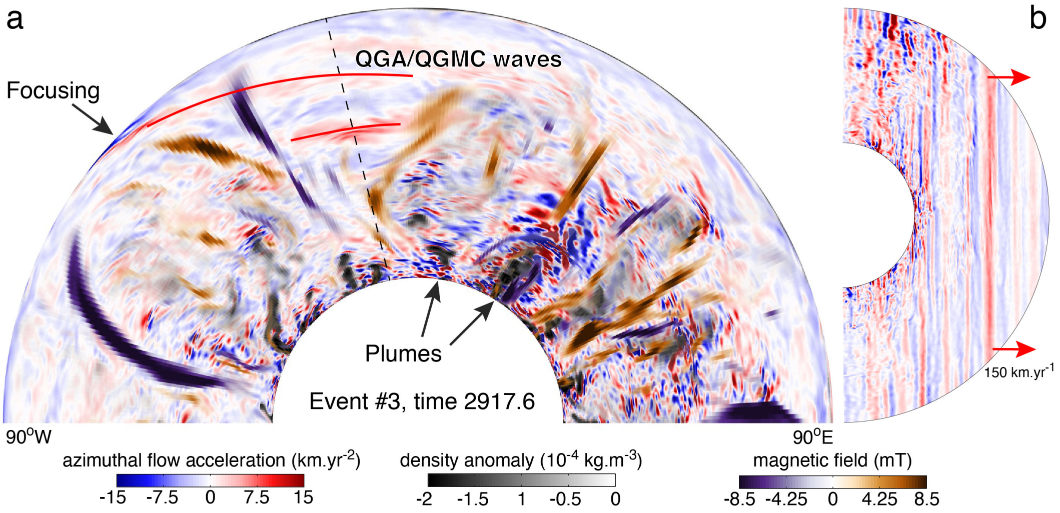

Figure 3.3: Structure of azimuthal flow acceleration (red/blue), density anomaly (shaded grey) and radial magnetic field (orange/purple) in a portion of the equatorial plane (a) and in a meridional plane (b) located by a dashed line in (a), during event 3 belonging to the DP type (see text), with waves being send out by buoyancy releases at the inner core boundary. The selected time is shortly before the SA pulse in the event (see Fig. 3.2a). The red curves in (a) locate QGA/QGMC wave fronts.

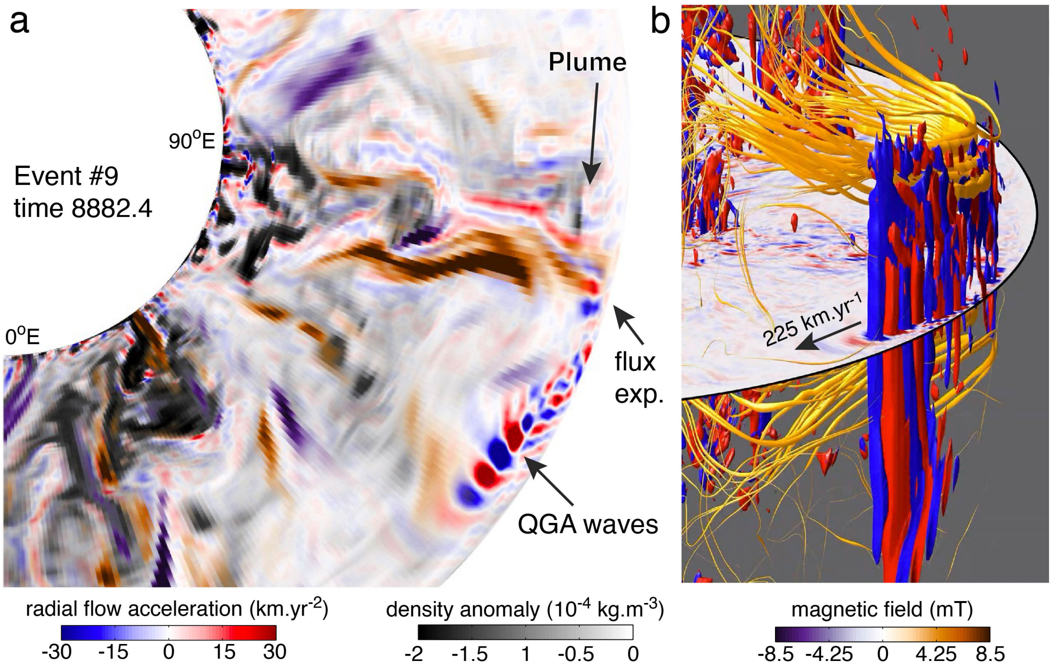

Figure 3.4: Structure of the cylindrical radial flow acceleration (red/blue), density anomaly (shaded grey) and radial magnetic field (orange/purple) in a portion of the equatorial plane (a) and in a three-dimensional rendering (b) during event 9 belonging to the SC+FE type (see text). The selected time is near the maximal SA pulse of the event (Fig. 3.5c). Here QGA waves are sent out here by a flux expulsion event at the CMB, following a shallow convective upwelling. In (b) three-dimensional magnetic field lines are represented with thickness proportional to the local magnetic energy, and two isosurfaces of cylindrical radial velocity have been represented at levels ±20 km/yr.

model, and then slow down as they ascend and convert to QGMC waves (Gerick et al, 2021) once the Coriolis force becomes more pregnant. These waves being transverse, they are best seen on the azimuthal component of velocity acceleration when propagating in the cylindrical radial direction. The waves undergo focusing mechanisms at equatorial position beneath the CMB, near the exit point of radial magnetic flux patches (Aubert and Finlay, 2019), causing the flow acceleration secular acceleration signals seen in Fig. 3.2a. The meridional structure of the waves (Fig. 3.3b) is highly columnar, as expected from the quasi-geostrophic framework upon which these evolve. DP events typically feature jerk events composed of one single wavetrain that causes multiple alternations in the core surface SA as the successive wavefronts arrive.

When hydromagnetic waves are triggered by a buoyancy release close to the CMB at equatorial position, the jerk trigger is classified in table 3.1 as ’SC’, for

'Shallow Convection'. In this case, the waves travel a shorter distance to the CMB. The presence of a convective upwelling close to the CMB can also lead to events of magnetic flux expulsion (FE), where it is this time the evolution of the Lorentz force that causes the inertial disruption to the QG-MAC balance. Neither the convective plume nor the flux expulsion directly cause the jerk signals because they evolve on the multidecadal time scale of secular variation. But it is the inertia-bearing hydromagnetic wave that they send out that are responsible for these signals. Event 9 (Fig 3.4) is characteristic of a situation where both SC and FE trigger the jerk. Here, an azimuthally-travelling QGA wave propagates at the one-dimensional Alfvén velocity of 225 km/yr from the tip of the location where the shallow plume expels magnetic flux. The transverse wave pattern is this time best seen in the cylindrical component of flow acceleration. Unlike the cylindrical-radially propagating case of Fig. 3.3, the propagation speed does not vary until the wave is dissipated because the nominal influence of the Coriolis force remains the same at a constant cylindrical radius. As in the DP case above, the QGA wave is the support of the rapidly alternating magnetic core surface acceleration signal that causes the jerk. The internal dynamical structures are again highly columnar and confirm quasi-geostrophy of the wave (Fig. 3.4b).

In all low-latitude, wave-driven jerks, regardless of their trigger mechanism, in addition to QGA and QGMC waves we also observe the emission of azimuthally-propagating longitudinal Rossby waves at speeds in excess of 1000 km/yr, which are the other category of waves that can arise from an inertial disruption of the QG-MAC balance (Aubert and Gillet, 2021). However, these do not bear a magnetic signature and do not play a role in the production of jerk signals as their magnetic energy is low and dominated by their kinetic energy.

3.3.7 Main spatio-temporal characteristics of low latitude, wave-driven jerk events

Fig. 3.5 reveals that low latitude, wave-driven jerk events can have highly variable signatures on the time series of SA and jerk energy. SC and FE events (e.g. events 2 and 9 depicted Figs. 3.5a,c, and events 1,6 and 12) frequently have long temporal baselines up to 60 years, as they unfold over a multidecadal duration linked to the convective and magnetic evolution of the system near the core surface. This creates a multiplicity of chaotic occurrences where the QG-MAC balance is disrupted and hydromagnetic waves causing the jerk signals are sent out. Such events tend to produce the strongest jerks of the database in terms of the SA energy E_{SA}. The peaks in E_{SA} are frequently too fast to be detectable once a 3-year moving average is applied to compute E_{J}, representing the typical temporal resolution of satellite measurements for geomagnetic acceleration. This results in $E_{\mathrm{J}}^{\max}/E_{SA}^{\max}$ well below unity, with values as low as 0.1 being for instance observed in event 6 (table 3.1). Three shorter events (7, 11 and 13 shown in Fig. 3.5d) somewhat differ from this trend, despite involving a FE trigger. These mostly carry the signature of a single, small-scale flux expulsion event.

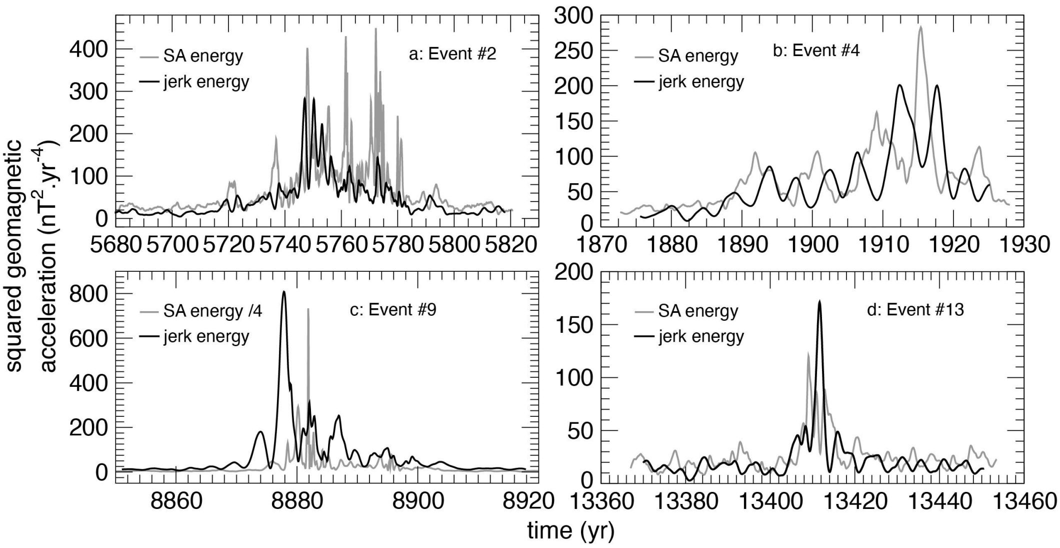

Figure 3.5: Time series of E_J (black) and E_SA (grey) during the four jerk events 2,4,9 and 13 (a-d).

In contrast, DP events (Fig. 3.5b) show a significantly more regular alternation of off-phase peaks in E_J and E_SA. Contrary to SC and FE jerks, the successive SA pulses observed during the unfolding of DP events can indeed be seen as belonging to the same wavetrain caused by a single convective trigger, which explains the regularity and alternation of the SA and jerk energy pulse sequence. The duration of the event is also shorter (up to 30 years) as it links with the limited life time of the wave. DP events typically feature lower SA energies than SC and FE events, but also achieve ratios $E_\mathrm{J}^\mathrm{max}/E_{SA}^\mathrm{max}$ closer to unity because of the regularity of the signal. It is therefore possible to obtain DP, SC and FE jerks of similar jerk energy.

The spatio-temporal characeteristics of the simulated jerk events are best explored by looking at time-longitude plots of radial SA at the equator of the CMB (Fig. 3.6). Compared to similar plots in Aubert and Finlay (2019), it is immediately apparent that the evolution from the Midpath (50% of path) to the 71p model leads to alternating SA pulses that are now significantly clearer, stronger and shorter. This is because the Alfvén time has shortened by a factor 2.5 relatively to the magnetic diffusion time. This also guarantees more polarity alternations in these SA pulses before the waves fade out, which are for instance clearly seen in the DP event 4 (Fig. 3.6a,b). The picture provided at native temporal resolution and up to spherical harmonic degree 13 (Fig. 3.6a) is not much affected by a filtering step down to degree 9 and with a 3-year moving average in time (meant to take the resolution of satellite geomagnetic observations into account). The coherent alternation of SA pulses reflects a wavetrain coming from a single trigger. The long azimuthal wavelength of the wavefronts (see e.g. Fig. 3.3) ensure temporal synchronisation of SA polarity changes at longitudinally remote locations (this is

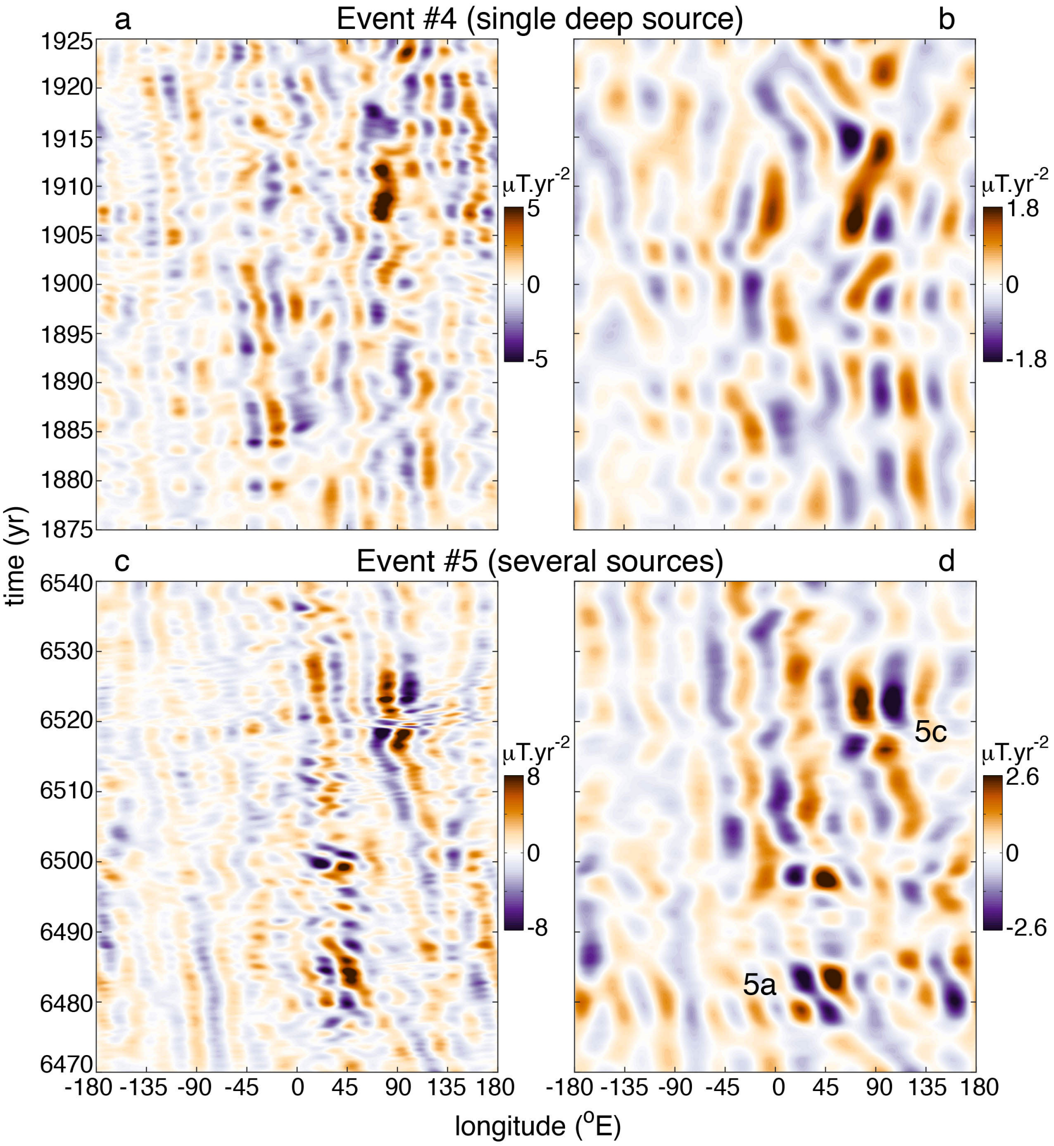

Figure 3.6: Time-longitude plots of equatorial, radial SA at the CMB for jerk events 4 (a,b) and 5 (c,d). SA is truncated after spherical harmonic degree 13 and presented at native temporal resolution in (a,c). In (b,d), spatial truncation is applied after degree 9 and a running average in time with window width 3 years is applied, to mimic the typical spatio-temporal resolution of SA satellite measurements.

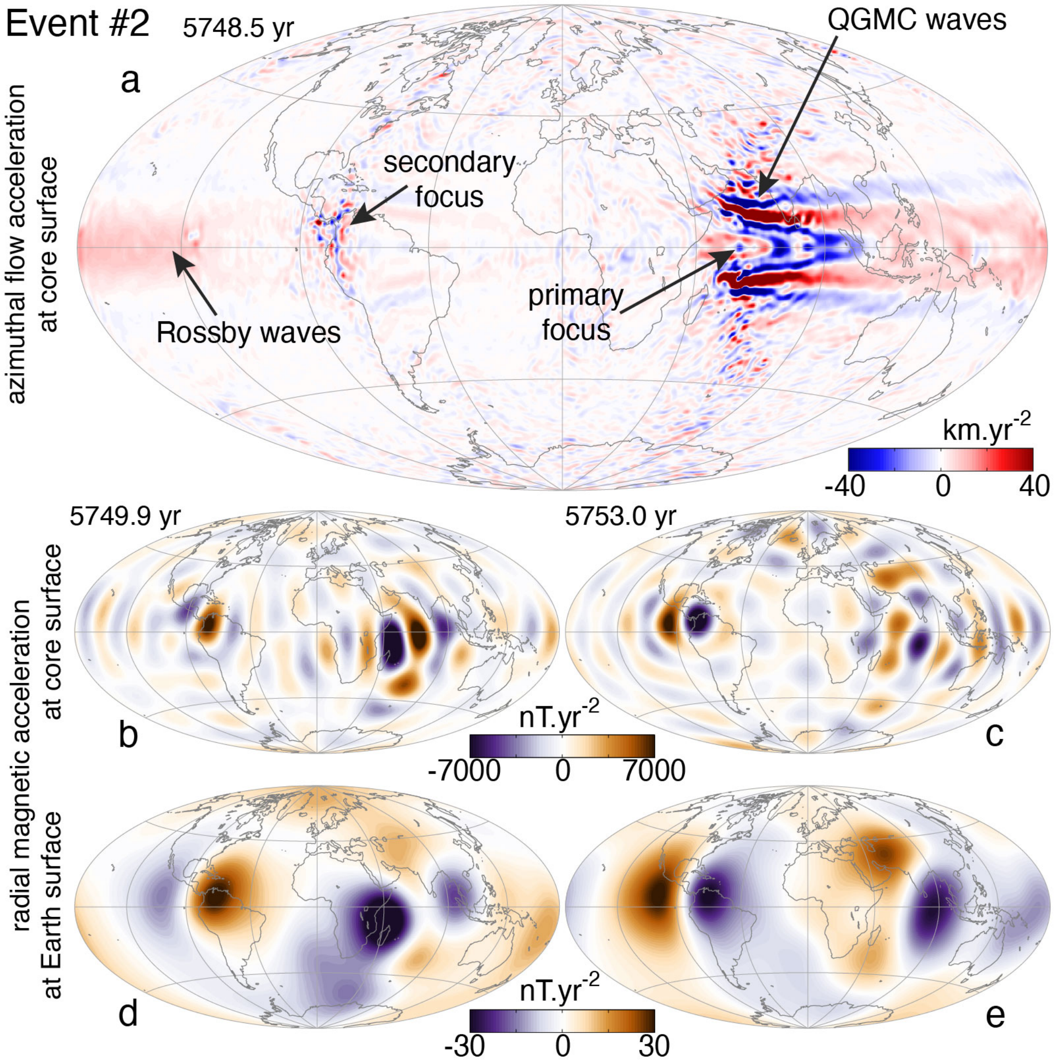

Figure 3.7: a: Hammer projection of azimuthal core surface flow acceleration during event 2, at the time of the strongest SA energy peak of the event (see Fig. 3.5a). b,c: Hammer projections of core surface radial SA at two closely spaced times during event 2, truncated after spherical harmonic degree 13, showing a synchronised polarity alternation of SA flux patches. d,e: Hammer projections of the Earth surface radial SA at the same times as b,c, showing two remote and temporally synchronised alternating dipolar structures.

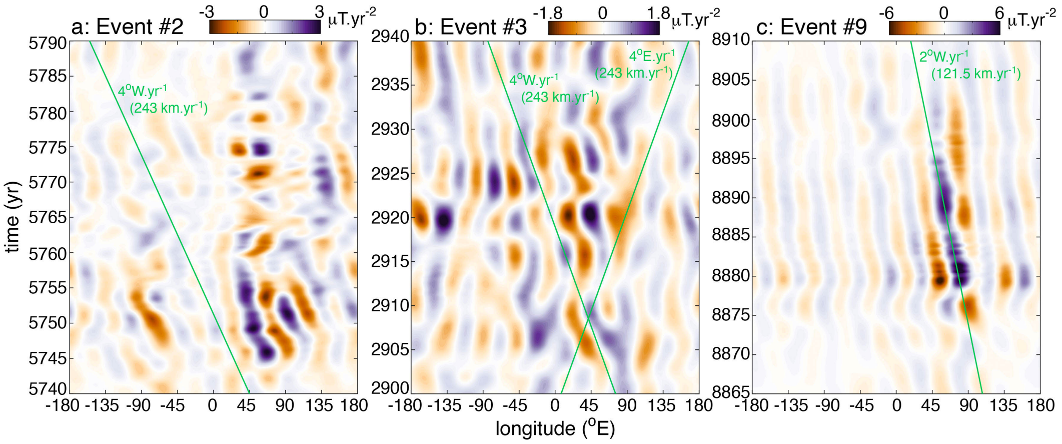

Figure 3.8: Time-longitude plots of equatorial, radial SA at the CMB for jerk events 2 (a), 3 (b) and 9 (c). SA is truncated after degree 9 and a running average in time with window width 3 years is applied. Green lines delineate east- and westward propagation at the reported angular and linear velocities.

explored in more detail in Fig. 3.6 below). Examining a more complex event with several different triggers (Fig. 3.6c,d) reveals several notable differences. While event 5a shares the feature of a DP event, event 5c (of SC and FE type) involves extremely short time scales at native temporal resolution that are filtered out once the temporal resolution degradation step is performed (Fig. 3.6c,d). In that case, the filtered view shows mostly periods of 3 years that are not representative of the rapidity of the event. The multiplicity of triggers is attested here by the unsynchronised longitudes and times at which the events occur, as well as the absence of temporal coherence along at a given longitude. Note that event 5b cannot be analysed on this equatorial view as it is a high-latitude event.

Event 2 most clearly illustrates the long-range longitudinal synchronisation that can arise because of the spatial structure of hydromagnetic waves involved in the jerk. Fig. 3.7a shows the structure of the QGMC wavefronts as they converges towards equatorial position at the core surface, at a time corresponding to the maximal SA pulse of the event (Fig. 3.5a). There are two convergence points in this case (India and America), where temporally alternating SA pulses can be seen at the core surface on Fig. 3.7b,c. Rapidly propagating Rossby waves sent eastwards along the azimuthally elongated QGMC wavefront from the primary (Indian) convergence point rapidly communicate the perturbation to the secondary (American) convergence point, such that the two small-scale flux expulsion events triggering the jerk signal (see also Fig. 3.10a below) are almost synchronised in time. At the Earth surface (Fig. 3.7e,f) the jerk event therefore comprises two longitudinally remote and local dipolar structures in the SA that quasi-simultaneously alternate their polarity in time.

About half of the analysed jerk events feature coherent azimuthal drift of SA

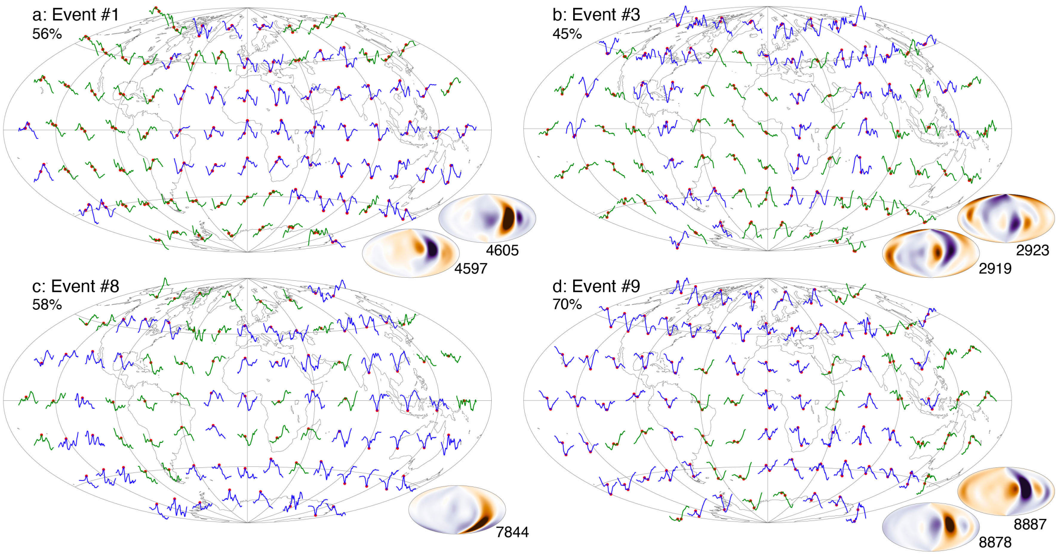

Figure 3.9: Time series of the east (φ) component of the SV presented over 50 years at regularly spaced locations of the Earth surface, during low-latitude, wave-driven jerk event 1 (a), 3 (b), 9 (d) and the high-latitude, convectively driven jerk 8 (c). The red dots locate the tips of 'V-shapes', or maxima J_{φ}^{20} in the smoothed eastward SA change (equation 3.4), imaged in the insets where the corresponding time at which they occur is also reported. The SV traces are colored in blue when the criterion $J_{\varphi}^{20}(\theta,\varphi) > 3\ SA_{\varphi}^{20}(\theta,\varphi)$ outlined in section 3.3.3 for detectability of the V-shapes is satisfied for at least one of the extrema at a given location, and in green otherwise. The percentage of Earth surface over which V-shapes are observed that way is also reported next to the jerk event number.

structures at speeds 100-200 km/yr far exceeding that (about 15 km/yr) of the convective westward drift. The drift can again be analysed on time-longitude plot of the equatorial radial SA (Fig. 3.8) presented at the 'satellite-like' resolution. Westward drift is mostly seen as it corresponds to the natural propagation direction of QGMC modes near the core surface (Gerick et al, 2021). The drift also caused by the strong Alfvén wave sent westward near the core surface during event 9 (Fig. 3.4) is only partially seen in this filtered view, as the speed retrieved from the time-longitude plot is below that of the wave. Eastward drift is also sporadically seen and less coherent than the westward drift (for instance in event 3, Fig. 3.8b). This cannot be attributed to Rossby waves such as those seen in Fig. 3.7a as these are too fast (speeds in excess of 1000 km/yr Aubert and Gillet, 2021) and carry too little energy to participate in the jerk signal. This likely result from SA flux patch alternations and rotations that are apparently seen as a drift.

The presence and geographical distribution of 'V-shapes' in time series of individual SV components in analysed in Fig. 3.9. While a given SV component is not particularly meaningful in the simulation context, the east component is chosen here for easier comparison with the Y component of observatory time series that tends to present the least noisy V-shapes during know observatory-era jerks (e.g. Wardinski and Holme, 2011). The properties of the kernel converting core surface to Earth surface SA signals are also of interest here as jerks occurring in the equatorial Asian region are best seen in Europe on the east component. Strong (in terms of jerk energy) wave-driven, low-latitude jerks like events 1 and 9 (Figs 3.9a,d), and also events 2 and 6 produce clear V-shapes that are generally widespread around the globe (with coverage ratings up to 75% according to the criterion outlined in section 3.3.3 and table 3.1). Weaker jerks tend to produce discernable V-shapes over less of the Earth surface. The tips of V-shapes are generally nearly synchronised around the globe, though with possible time delays not exceeding a few years. Jerks with multiple SA pulses in time present multiple V-shapes, that occur as a succession of 'V' and 'inverted V'-shapes, as expected from the polarity changes of the SA. Interestingly, it is not needed to have a jerk source at high latitude at the CMB (as for instance in jerk 8, Fig. 3.9c) to observe V-shapes at high latitudes at Earth surface. Indeed, the distance of Earth surface to the core surface where the jerk SA signals are localised suffices to propagate the perturbation over a wide region of Earth surface (see insets in Fig. 3.9). The creation of widespread and nearly synchronised V-shapes is therefore simply a geometrical result of the upward continuation step that converts core surface to Earth surface fields.

3.3.8 Other byproducts of jerk events

Expulsion of magnetic flux i.e. the appearance of new pairs of magnetic flux patches at the core surface is a frequent phenomenon during jerk events. As previously stated, this processes is itself not responsible for jerk signals but can trigger the wave dynamics that creates these signals (see Fig. 3.4). Fig. 3.10 presents radial magnetic flux structures expelled during jerk events 2 and 9. These structures are typically of small scale at native model spatial resolution (Fig. 3.10a,b) and are rarely seen at the typical resolution $\ell \leq 13$ of geomagnetic observations (Fig. 3.10c,d). This is confirmed by the nearly vanishing values of the diagnostic MFS in table 3.1 for most jerk events. Only events 1, 6 and 9 (imaged in Fig. 3.10d) have values of MFS exceeding unity (see table 3.1), meaning that the large-scale signature of the magnetic flux expulsion during the event clearly deviates from the normal creation process of flux patches at the CMB in the 71p model. Event 2 with MFS = 0.7 (Fig. 3.10c) has a barely visible large-scaled expelled patch in the Indian region, while the American patch is not visible at large scale.

In contrast to magnetic flux expulsion, surges of the SV energy at Earth surface are more common during jerk events, as witnessed by the values of the SVS indicator in table 3.1. Fig 3.11 shows time series of the r.m.s. SV amplitude at Earth surface that highlight four notable instances of this phenomenon. For the strong jerk events 1,6,9 (Fig. 3.11a,c,d) that produce visible core surface magnetic flux expulsion at large scale, it is natural to also observe surges in the Earth surface SV energy, with the corresponding signature at the core surface comprising the ap-

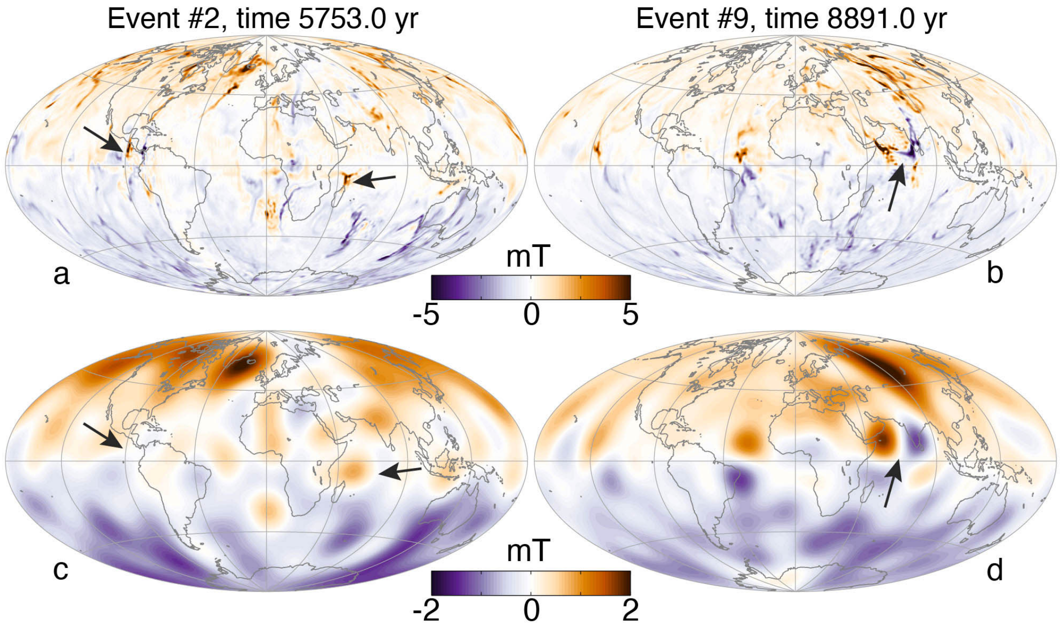

Figure 3.10: Hammer projections of the CMB radial magnetic field during jerk events 2 (a,c) and 9 (b,d). In (a,b) the field is presented at native model spatial resolution, and is truncated after spherical harmonic degree 13 in (c,d). Black arrows locate the magnetic flux structures that are expelled during the jerk events.

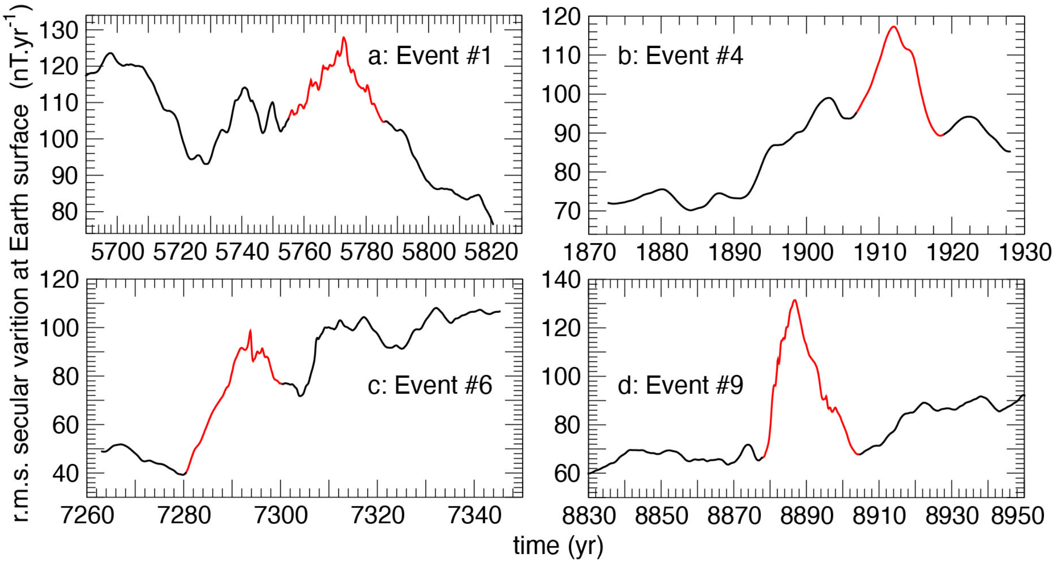

Figure 3.11: Time series of the Earth surface r.m.s. SV amplitude A_{SV}, during events 1 (a), 4 (b), 6 (c) and 9(d). The red portions of the curves delineate the surges occurring during the jerk events.

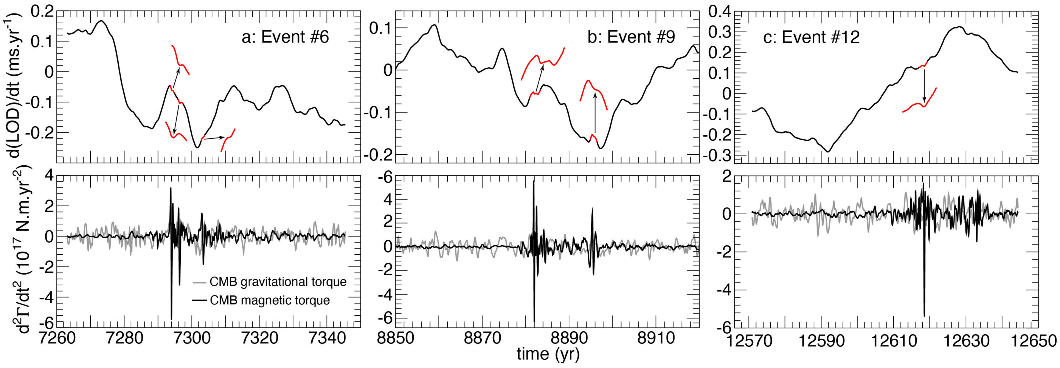

Figure 3.12: Top row: time series of the length-of-day rate of change d(LOD)/dt in the vicinity of jerk events 6 (a), 9 (b), and 12 (c). Bottom row: corresponding time series of the accelerations $d^2\Gamma_M/dt^2$ and $d^2\Gamma_G/dt^2$of the magnetic and gravitational torques, showing magnetic torque perturbations caused by the jerk that significantly exceed those of the gravitational torque. The corresponding inflexions in d(LOD)/dt are highlighted in red and magnified in the top row.

pearance of strong patches of SV as the flux is expelled. Interestingly, however, SV surges can also be observed without a specific signature large-scale magnetic flux expulsion, as for instance in event 4 (Fig. 3.11b). This indicates a notable increase in the variability of the largest-scale components of the magnetic field, without a clear signature in terms of small-scale SV patches at the core surface.

We finally analyse in Fig. 3.12 the length-of-day signature of jerk events produced in the simulation. Only the three strongest low-latitude, wave-driven jerks 6, 9 and 12 have been found to create distinct inflexions in d(LOD)/dt that can be clearly associated to the jerk-driven acceleration of the CMB magnetic torque $d^2\Gamma_M/dt^2$. Here, this phenomenon therefore appears to require jerks of sufficient amplitude, but it could occur more routinely at end-of-path conditions once the magnetic torque reaches a nominal amplitude about 7 times higher than at 71% of path conditions (according to the path scaling rules, Aubert et al, 2017), with the gravitational torque remaining constant along the path.

Bibliography

Aubert J (2018) Geomagnetic acceleration and rapid hydromagnetic wave dynamics in advanced numerical simulations of the geodynamo. Geophys J Int 214(1):531–547

Aubert J (2019) Approaching Earth's core conditions in high-resolution geodynamo simulations. Geophys J Int 219(S1):S137–S151, DOI 10.1093/gji/ggz232

Aubert J, Finlay CC (2019) Geomagnetic jerks and rapid hydromagnetic waves focusing at Earth's core surface. Nature Geosci 12(5):393–398, DOI 10.1038/s41561-019-0355-1

Aubert J, Gillet N (2021) The interplay of fast waves and slow convection in geodynamo simulations nearing earth,Äôs core conditions. Geophys J Int DOI https://doi.org/10.1093/gji/ggab054

Aubert J, Gastine T, Fournier A (2017) Spherical convective dynamos in the rapidly rotating asymptotic regime. J Fluid Mech 813:558–593

Gerick F, Jault D, Noir J (2021) Fast quasi-geostrophic magneto-coriolis modes in the earth's core. Geophys Res Lett p 2020GL090803

Schwaiger T, Gastine T, Aubert J (2019) Force balance in numerical geodynamo simulations: a systematic study. Geophys J Int 219(S1):S101–S114

Wardinski I, Holme R (2011) Signal from noise in geomagnetic field modelling: denoising data for secular variation studies. Geophys J Int 185(2):653–662, DOI 10.1111/j.1365-246X.2011.04988.x

3.4 Report on viability of using a Bayesian probabilistic method to detect spatially-local geomagnetic jerks

4DEarth_Swarm_Core ESA project deliverable R-E.1 (continued)

P. Livermore
University of Leeds

3.4.1 Rationale

Geomagnetic jerks, abrupt changes in the local dynamics of magnetic field generation, were first identified as 'V'-shaped changes in the slope of the secular variation at ground-based observatories, either by fitting piecewise linear functions and finding the interior knot points (e.g. Brown et al, 2013), or by wavelet analysis (Mandea et al, 2010). A change in the slope of a piecewise linear function is equivalent to a step function of the second time derivative, or an impulse in the third. An alternative definition therefore is based on the spatially-averaged temporal jump in the second time derivative of the magnetic field (Aubert and Finlay, 2019), E_J, whose peaks signify a (global) jerk. It is of interest to relate spikes in the global quantity E_J with the more widely used localised methods, because jerks may not occur everywhere on the Earth's surface, and even those that do occur may not be contemporaneous.

We explore the possibility of using a recently developed Bayesian method to find the localised 'V' shaped signature of jerks from the path geodynamo model (deliverable D-C.1). We compare the approach and results to the global diagnostics presented in the jerk catalogue (deliverable D-E.1) based on E_J. Although the path model is only an approximation to the dynamics of Earth's core, it provides a complete description of the internally generated field which enables us to apply the jerk-finding algorithm to data without contamination from external signals found in observational records. Ultimately, a better understanding of the surface signature of jerks, gleaned from numerical models, will allow more insight into core dynamics gleaned from geomagnetic data.

3.4.2 The Bayesian model

Fitting a 2-segment piecewise linear fit to secular variation has been used by many studies, but there are two difficulties with this direct method. The first is the selection of the data-window. In the majority of cases, the window is selected by eye, and the piecewise linear regression used to hone the exact time of the jerk. Yet this is not objective: there are cases where there may be multiple changes, or where the change in slope is marginal. The second difficulty is quantifying the fit (and the timing of the jerk) by a piecewise linear function. Many methods report only the fit with no uncertainty. Quantification of jerk uncertainty has been achieved in some probabilistic studies (Pinheiro et al, 2011; Brown et al, 2013) which sought peaks in the likelihood (the probability of the data given a model) of the jerk time, with some threshold needed to characterise a jerk. The spread of the peak gives some measure of uncertainty. Yet a Bayesian quantification, characterising the probability of the piecewise linear fit given the data set, may be a better tool.

Motivated by analysis of sparse, noisy archeomagnetic data, a reverse jump Monte Carlo Markov chain method has been developed to calculate the posterior distribution of magnetic field intensity with time (Livermore et al, 2018),

$$p(\mathbf{m}|\mathbf{d}) = C p(\mathbf{m})\, p(\mathbf{d}|\mathbf{m})$$

where $\mathbf{m}$ is the model description, $\mathbf{d}$ is the data and C is a normalising constant.

This method calculates a large ensemble of models using a guided random walk, whose statistics converge to the distribution sought. Of particular importance here is that each ensemble member is assumed to be piecewise linear and so the ensemble statistics of the interior change points can be used to quantify the posterior probability of a jerk at any time. Also of note is that the number and start/end points of the piecewise linear segments are not fixed, but rather they are unknown and are co-estimated as part of the distribution. All Bayesian models favour low-dimensionality if the data allows (Sambridge et al, 2006), because for the same likelihood a prior with fewer degrees of freedom is more concentrated and so the posterior distribution is higher. For the problem of finding jerks, this means that model complexity (i.e. inserting interior change points) is only increased if, and when, the data require. For any specific model (or the ensemble in general), the temporal distribution of changepoints then reflects the constraints of the data which are possibly on multiple timescales: faster dynamics require more changepoints, whereas slower dynamics require fewer. There is no need to impose any regularisation as the method naturally will always favour low-dimensionality.

Given the ensemble, it is straightforward to quantify the posterior probability of a jerk by counting the number of changepoints that fall within a given set of interval bins (e.g. spanning 1 year), with at most one count per bin for any given model, normalised by the number of models. If all models contain a changepoint within a certain interval, then the normalised probability is one and a jerk is certain. Note that if the data require that all models contain a changepoint in several bins, then the probability of a jerk within each bin is also one and so a possible output is multiple certain jerks. Usually however the normalised probability within a bin is not close to one, as it is in general possible to construct a range of models consistent with the data but with a variety of structures with change points spread over multiple bins.

The method requires specification of the prior probability $p(\mathbf{m})$ of the parameters needed to define a piecewise linear function. For simplicity we consider the that number of interior vertices and their values (change points) are uniformly distributed. It also requires specification of the likelihood, which is based on the assumption that each data point is normally distributed with common standard deviation σ and given simply as proportional to

$$\exp\left(-\sum(d_i - f_i)^2/(2\sigma^2)\right),$$

where d_i is the data and f_i the associated model values. The value of σ can be estimated from the data (Pinheiro et al, 2011) but here we treat it as a parameter. Note that this uncertainty really represents both data and model uncertainty: even with error-free data we don't expect that geomagnetic SV is exactly piecewise linear.

3.4.3 The code

Documented code that calculates the posterior distribution of jerks from timeseries of secular variation can be found in

`https://github.com/plivermore/jerk_finder`

The kernel of the Bayesian (Fortran 90) code has been rewritten with a Python interface (using f2py) making it callable from a Jupyter notebook. The repository includes Jupyter notebooks that document several introductory examples (see below) and an application to the path model output.

3.4.4 Example

Here we apply the method to a simple piecewise linear function over time $[0, 100]$ (fig 3.13(a)) containing a single change in slope at $t = 50.5$, the centre-point of the yearly bin 50–51. The timeseries has been sampled yearly and noise (distributed with mean zero and standard deviation 5) has been added (fig 3.13(b)). This is now the dataset which we pass to the jerk-finder.

Three parameters that control the efficiency of the random walk used to create the ensemble (giving the magnitude of the random perturbations) are $\sigma_{change} = 10$; $\sigma_{move} = 5$; $\sigma_{birth} = 10$. The model is run for 10000 iterations as burn-in before keeping the next 2,000,000 models, thinned to keep only every 100th model. The resulting posterior distribution is shown in fig 3.13(c), in which the mean, median and modal model agree very well. The 95% credible intervals are also drawn, but the uncertainty range is too thin to see visually. Lastly, figure 3.13(d) shows the discrete probability distribution of a jerk in yearly bins. The bin 50-51 years has the highest probability of all bins (of about 0.7) so that the analysis recovers the known jerk at $t = 50.5$; but interestingly the probability is not close to one even for this simple example. There is clearly some uncertainty in determining the change-point(s) due to the sparse data sampling and implicit uncertainty in the likelihood, reflected in the fact that the neighbouring bin, 51–52 years, has a probability of around 0.3.

In a second example (figure 3.14), we apply the method to a timeseries containing three jerks, associated with different slopes: the jerk at $t = 20.5$ has only a small change in slope, whereas that at $t = 40.5$ is severe and that at $t = 60.5$ is moderate. Adding the same amount of noise and sampling yearly gives the posterior probability of a jerk shown in figure 3.14(c). Jerk 2 has the highest probability, followed by jerk 3 and jerk 1. For jerk 1, the level of uncertainty is such that the corresponding change point identified by the method can fall into one of a number of yearly bins because a moderate error in changepoint timing results only in small error in fit of the piecewise linear time series. The figure shows that the pdf of a jerk is low but broad. For jerk 2, a moderate error in changepoint timing has a large effect on the predicted timeseries and so any misfit is higher and correspondingly has a small posterior probability: thus only small errors in jerk timing have a high posterior probability. Therefore the pdf for jerk 2 has a well defined narrow peak (attaining about 0.9).

Figure 3.14(d) shows the posterior distribution of the number of interior change points. The most likely value is (the correct value of) 3, but there is a short tail and higher values are possible. Recall that there is no regularisation: the natural parsimony of Bayesian methods favours small numbers of change points.

3.4.5 Application to the path model

The jerk catalogue includes 14 events identified as jerks using the global measure E_J. Here we focus on one of the strongest events (jerk 9) occurring at time $t = 8880$ of the model. The random walk parameters are fixed as before and we compute 20M iterations.

Figure 3.16 shows timeseries of the X, Y, Z components of secular variation at the modelled Earth's surface ($r = 6371$) at colatitude 90° and longitude 45°, approximately at the centre point of the positive patch of secular acceleration of the jerk event (see figure 3.15(b)). The discrete jerk pdf is shown by the histograms, assuming that, for each component, σ is 10% of the total variation (maximum – minimum) in SV over the window shown. A plot showing only the behaviour within 20 years of $t = 8880$ based on the same data is shown in figure 3.17.

Over the 400 years of modelled time shown, the jerk energy E_J takes a single prominent peak at around $t = 8877$. The local method finds, in all three components and over the same time window, that the jerk events of highest probability (about 0.3) are around $t = 8880$, agreeing well with the global analysis. However, the signature of the jerk in the local SV is far more complex. For each component there are two changes in slope: the first jerk in the X and Z components align well with the peak in E_J at $= 8878$, but the first jerk in Y is delayed by about 5 years to $t = 8882$. The second jerk occurs in the X and Z components at $t = 8884$, with that for the Y component about 10 years later at at $t = 8893$. Figure 3.16 also shows a number of other smaller peaks in jerk probability, for example, around $t = 8700$ in the Y component which has a probability of about 0.2. Interestingly, there is no peak in E_J that corresponds with these other events.

Taking $\sigma = 20\%$ of the total SV variation for each component gives figure 3.18, which shows a very similar behaviour (and relative timing), albeit slightly smoothed owing to the larger error budget.

For each of the histograms we can count the number of peaks over a given time window, subject to certain criteria, labelling those which qualify as ‘jerks’. To do this we can use the Python function find_peaks in scipy, and we set thresholds on the (a) probability threshold τ (i.e. the height of the bars in the histograms) and (b) the temporal distance between the peaks. Figure 3.19 shows the number of jerks detected on a 5x5 degree grid of discrete locations on Earth’s surface, corresponding to probability thresholds of 0.4, 0.3 and 0.2 for the histograms defined within $[8880 - 30, 8880 + 30]$ years, for a jerks spacing of at least 3 years.

As the threshold decreases, at all locations the number of events labelled as jerks increase. For the most stringent threshold considered, the locations which have a non-zero jerk count are localised where the SA is high, but the signal is patchy. Multiple jerks (0-4) can be found depending on location and threshold, despite only a single peak in E_J.

One region (around latitude 0, longitude 100) has 3 jerk events (the highest number for this case) identified in the Z component, but 3 jerks are identified at only one grid point in the Y component, and not at all in the X component. In all components the jerk signals are focussed around southern Asia. On lowering the threshold, 3 jerks appear in all components. Interestingly, at $\tau = 0.3$ there are 4 jerks are identified in the Y component (at around latitude 0, longitude 90E) but not at neighbouring longitudes showing that there is a large difference in signature within only a small change in spatial location.

Each plot has two counts in its title: Σ_{total} is the total number of jerks over all locations; Σ_{nz} is the number of locations with a non-zero jerk count. For the most stringent threshold, the Y component has the smallest signature, in terms of the number of non-zero locations (62) and total number of jerks (80), while the Z component has the most pronounced signature (with counts 112, 192). As the threshold decreases, we find similar statistics in the total number of jerks and non-zero locations in all three components (respectively about 1000 and 2000), although in this example the signature in the Y component has (marginally) the highest counts in both measures.

For this event, using a low threshold all components show similar jerk statistics but the Y component has marginally the largest signature. However, events with the very strongest local signature show predominantly in the Z component.

3.4.6 Conclusions

We have explored the possibility of using a transdimensional Bayesian method to analyse jerk signatures in the path dynamo model. The method appears to work well on based on timeseries centred around the largest event in the jerk catalogue, and finds local jerk events whose timing largely matches the peaks in the global diagnostic jerk energy E_J. There are several parameters that need to be chosen: the likelihood uncertainty, and a threshold on what qualifies as a jerk (e.g. probability threshold, and temporal distance between jerks).

A focus of the localised magnetic field around the time of jerk event 9 (from the catalogue) shows that

- A single peak in E_J can drive localised geomagnetic jerks with 0–4 events, whose signature depends strongly on location.
- The locations with the most number of jerks correspond to regions with strong SA.
- The Z (radial) component of field contains the highest number of strongest jerks.

Bibliography

Aubert J, Finlay CC (2019) Geomagnetic jerks and rapid hydromagnetic waves focusing at Earth's core surface. Nature Geosci 12(5):393–398, DOI 10.1038/s41561-019-0355-1

Brown W, Mound JE, Livermore PW (2013) Jerks abound: An analysis of geomagnetic observatory data from 1957 to 2008. Phys Earth Planet Int 223:62–76

Livermore PW, Fournier A, Gallet Y, Bodin T (2018) Transdimensional inference of archeomagnetic intensity change. Geophys J Int 215(3):2008–2034

Mandea M, Holme R, Pais A, Pinheiro K, Jackson A, Verbanac G (2010) Geomagnetic jerks: rapid core field variations and core dynamics. Space science reviews 155(1):147–175

Pinheiro K, Jackson A, Finlay C (2011) Measurements and uncertainties of the occurrence time of the 1969, 1978, 1991, and 1999 geomagnetic jerks. Geochemistry, Geophysics, Geosystems 12(10)

Sambridge M, Gallagher K, Jackson A, Rickwood P (2006) Trans-dimensional inverse problems, model comparison and the evidence. Geophys J Int 167(2):528–542

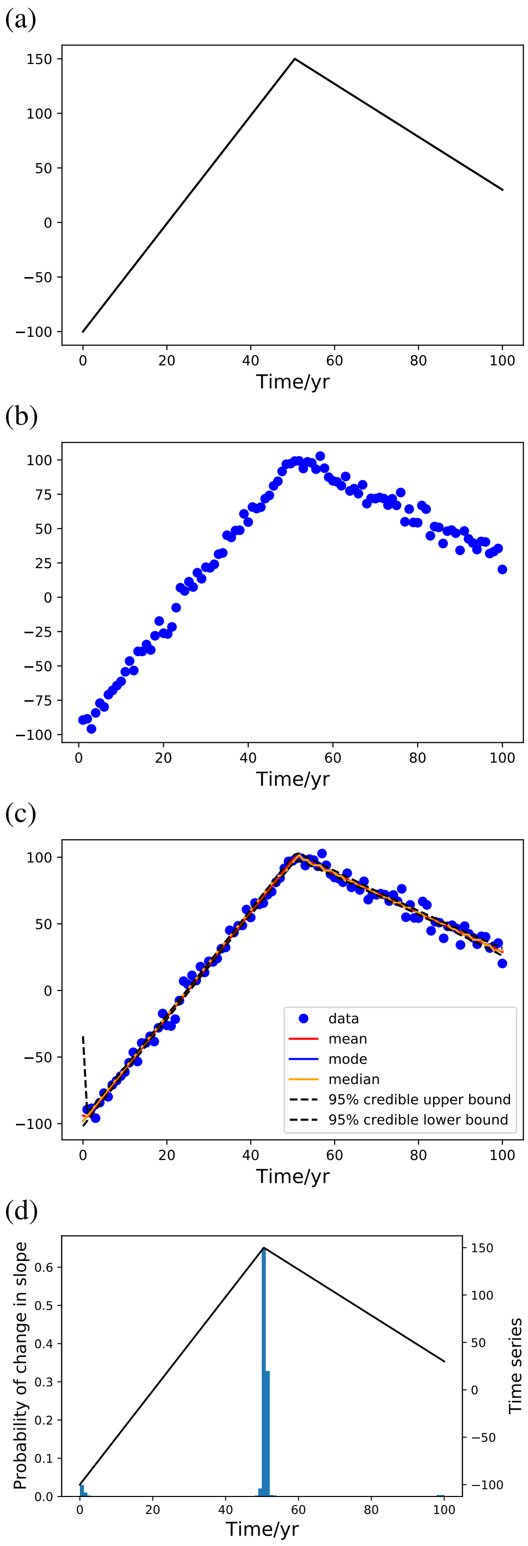

Figure 3.13: Determination of a jerk given a series of secular variation. The original noise-free timeseries (a) is sampled yearly and noise is added (b). The posterior distribution given this dataset is shown in (c), with the discrete probability of a jerk given in (d).

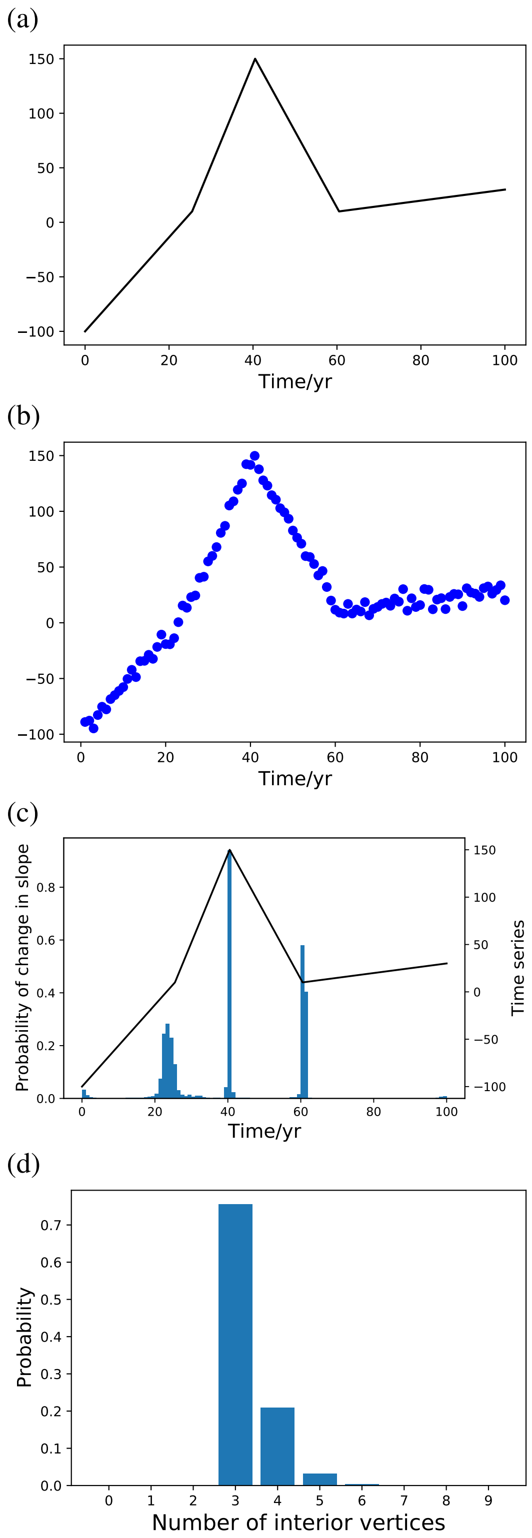

Figure 3.14: Determination of a jerk given a series of secular variation for an example with three known jerks. The original noise-free timeseries (a) is sampled yearly and noise is added (b). The discrete probability of a jerk is given in (c), while (d) shows the probability of the number of interior change points.

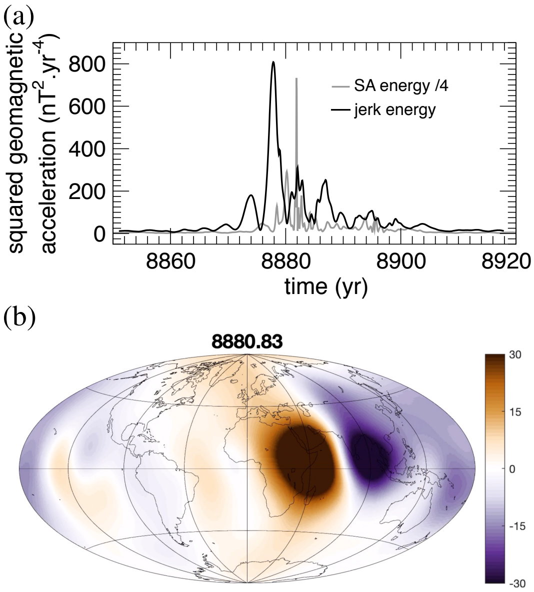

Figure 3.15: (a) Jerk diagnostics (jerk energy, secular acceleration) around the time of jerk 9 following Aubert and Finlay (2019); snapshot of the radial secular acceleration (nT/yr^2) around the time of jerk 9 showing where the event is located.

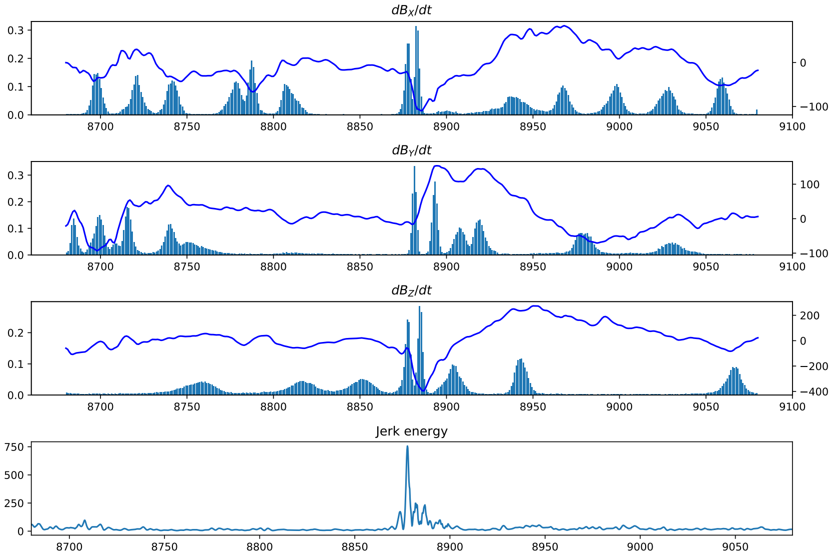

Figure 3.16: Composite plot of the X, Y, Z components of secular variation at the modelled Earth's surface at 45° longitude 0° latitude (right axis: nT/yr), and a histogram showing the discrete pdf of jerk occurrence (left axis). The jerk energy E_J is shown in the bottom panel for comparison. The value of σ is 10% of the total SV variation, for each component.

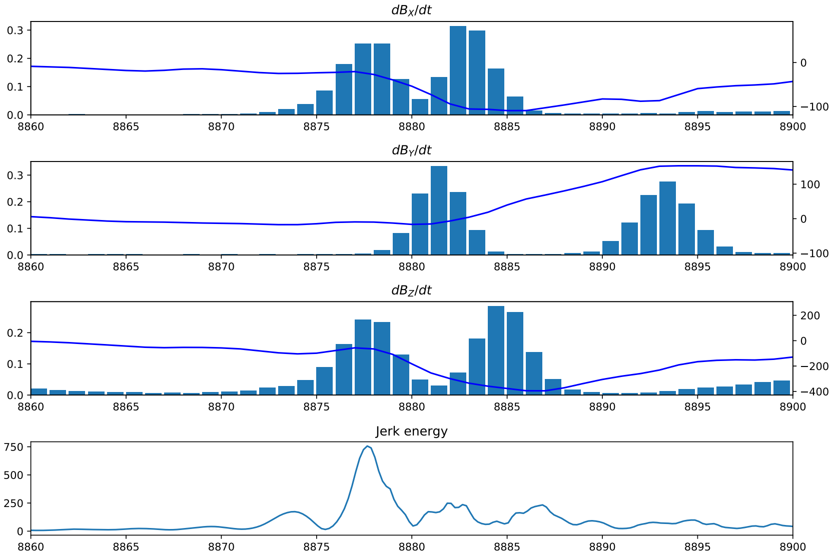

Figure 3.17: Composite plot of the X, Y, Z components of secular variation at the modelled Earth's surface at 45° longitude 0° latitude (right axis: nT/yr), and a histogram showing the discrete pdf of jerk occurrence (left axis). The jerk energy E_J is shown in the bottom panel for comparison. The value of σ is 10% of the total SV variation, for each component.

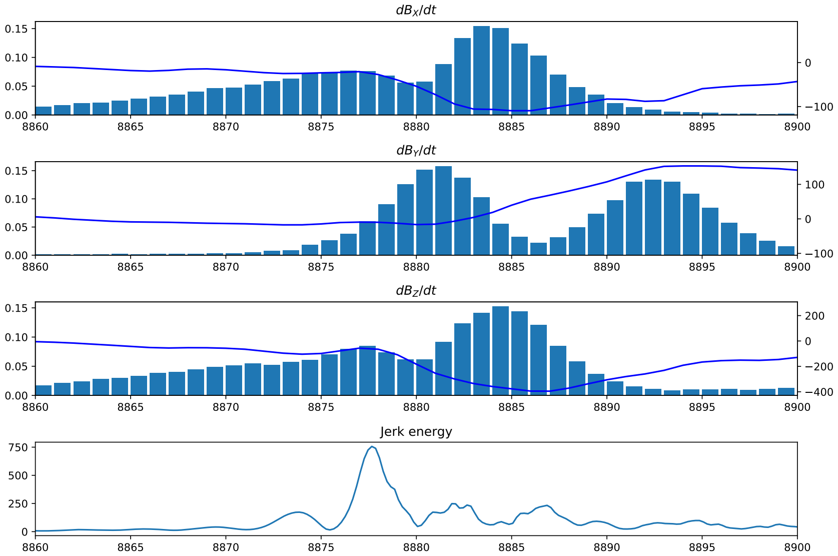

Figure 3.18: Composite plot of the X, Y, Z components of secular variation at the modelled Earth's surface at 45° longitude 0° latitude (right axis: nT/yr), and a histogram showing the discrete pdf of jerk occurrence (left axis). The value of σ is 20% of the total SV variation, for each component. The jerk energy E_J is shown in the bottom panel for comparison.

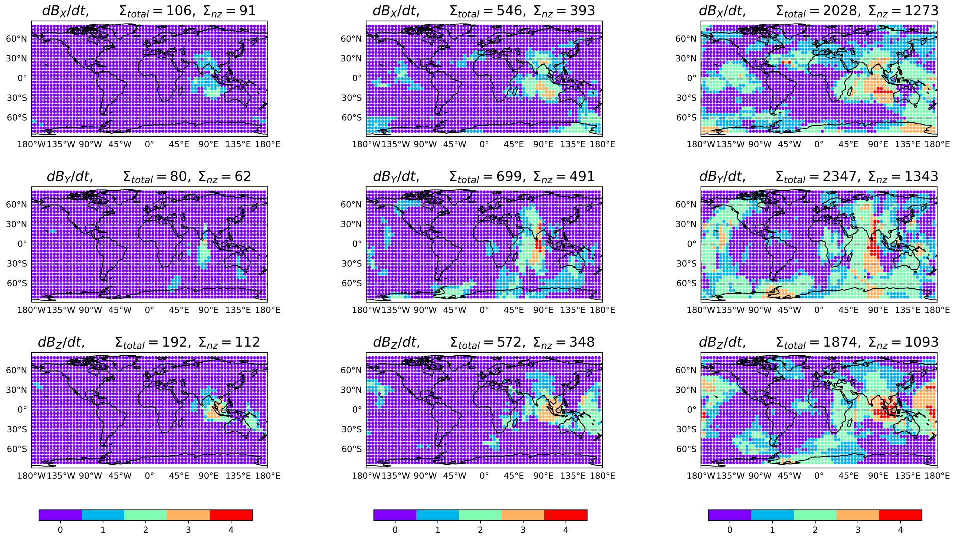

(a) $\tau = 0.4$ (b) $\tau = 0.3$ (c) $\tau = 0.2$

Figure 3.19: Numbers of jerks identified at discrete locations on the Earth's surface over the time window $[8880 - 30, 8880 + 30]$ years, for a jerk spacing of at least 3 years. The colourbar indicates what each colour represents. The columns show probability thresholds of $\tau = 0.4$, $\tau = 0.3$ and $\tau = 0.2$. In each plot title, Σ_{total} is the total number of jerks over all locations, while Σ_{nz} is the number of locations with a non-zero jerk count.

3.5 Dynamics of a high latitude jet

4DEarth_Swarm_Core ESA project deliverable R-H.1

P. LIVERMORE
UNIVERSITY OF LEEDS

The existence of a high latitude jet is motivated from the study of Livermore et al (2017), that suggests a jet can form at high latitude (about ±69° latitude) around the projection of the tangent cylinder. These dynamics are particular to the conditions of Earth's core, at vanishingly small inertia and viscosity, where the dynamics inside and outside the tangent cylinder may differ. Physically, any mismatch in flow across the tangent cylinder requires the excess to be redistributed locally (because of assumed incompressibility), which drives a strong azimuthal jet localised to high latitude. This can be seen simply in the equation describing incompressibility:

$$\frac{\partial}{\partial s}(s\,u_s) + s\frac{\partial}{\partial z}(u_z) + \frac{\partial u_\phi}{\partial \phi} = 0,$$

where rapid changes in u_s can only be accommodated by large azimuthal variations in the azimuthal flow, since the other term (involving z-derivatives) is assumed small in QG.

Here, we assess the fit of localised QG-flow with a strong localised azimuthal component (i.e. a jet) to the geomagnetic observations. To relate the changes in the radial geomagnetic field (B_r) on the CMB with the flow at the top of Earth's core, the induction equation under the frozen-flux assumption is:

$$\dot{B}_r = -\boldsymbol{\nabla}_H \cdot (\mathbf{u}_H\, B_r) \tag{3.13}$$

where $\mathbf{u}_H$ denotes the horizontal flow (Holme, 2015). We assume that the incompressible quasi-geostrophic flow, $\mathbf{u}$, can be written in terms of a stream function Ψ in the following form (Labbé et al, 2015)

$$u_s = \frac{1}{Hs}\frac{\partial \Psi}{\partial \phi}, \qquad u_\phi = -\frac{1}{H}\frac{\partial \Psi}{\partial s}, \qquad u_z = \frac{dH}{ds}\frac{z}{H^2 s}\frac{\partial \Psi}{\partial \phi}.$$

We have non-dimensionalised the core to have a radius of one (from 3480 km), and $H = \sqrt{1-s^2}$; (s,ϕ,z) are cylindrical coordinates.

To ensure that the flow is finite and satisfies the impenetrable condition $u_r = 0$ on the CMB, we require that $\partial\Psi/\partial\phi = 0$ at $s = 1$. This is because when $z = H$:

$$ru_r = su_s + zu_z = \partial\Psi/\partial\phi\left[\frac{1}{H} - \frac{1}{H}\right] = 0$$

except possibly at $s = 1$ when $H = 0$. When $s = 1$, $u_z = 0$ but u_s is undefined unless $\partial\Psi/\partial\phi = 0$ (and for which $u_s = 0$ there). This condition can also be derived through considerations of flux: a fluid that is incompressible must have the same azimuthal flux through any meridional slice. This follows simply by considering the (zero net) azimuthal flux into and out of an infinitesimal wedge of fluid, and noting that the boundaries are impenetrable. Thus

$$\frac{\partial}{\partial\phi}\int_0^1 \sqrt{1-s^2}u_\phi(s,\phi)ds = 0 \tag{3.14}$$

which recovers the previously derived condition.

In order to define a localised flow, as in Livermore et al (2017) we define Ψ by the real part of the modal sum

$$\Psi = \sum_{m=0}^{M} a_m\, e^{im\phi}\int_0^s \Phi_m(\rho)\,\sqrt{1-\rho^2}\,d\rho, \qquad \Phi_m(s) = \left[\sqrt{1-s^2}\,e^{-\beta^2} - c_m\right]s^{m+1}$$

where M is the maximum wavenumber, a_m are complex coefficients to be determined, β denotes $\frac{s-r_i}{\delta}$ where r_i is the non-dimensional inner-core radius $1221/3480$ and δ is the prescribed jet width.

The constants c_m are determined through imposition of the boundary condition on each Φ_m,

$$\int_0^s \Phi_m(\rho)\,\sqrt{1-\rho^2}\,d\rho = 0$$

for each Fourier mode individually. For convenience we also apply this to the $m = 0$ mode for which the boundary condition is actually automatically satisfied.

Each Fourier mode of flow then has an azimuthal component proportional to $\Phi_m(s)$ which is localised to the tangent cylinder. Note that there are two factors of $\sqrt{1-s^2}$ in the analytic prescription of the flow. One stems from the factor of H in the azimiuthal component of the QG flow, the other in the definition of Φ_m simply enables analytic integration to find Ψ which is convenient and does not affect the structure of the flow significantly. The factor of s^{m+1} ensures that the flow is regular on the rotation axis, and it can be shown that the flow is everywhere continuous.

The tangent cylinder is located at colatitude $90-\cos^{-1} r_i \approx 21°$, and we restrict our interest to 10°–30° colatitude (in the North) and correspondingly 150°–170° in the south that encompasses the important dynamics.

The target function is minimised over both northern (N) and southern (S) regions assuming that both δ and M are prescribed, which then determines the unknown modal coefficients by

$$\mathcal{R}_{\mathcal{N}+\mathcal{S}} = \int_0^{2\pi}\int_{10°}^{30°}\left(SV_{obs} - SV_{syn}\right)^2 \sin\theta d\theta d\phi + \int_0^{2\pi}\int_{150°}^{170°}\left(SV_{obs} - SV_{syn}\right)^2 \sin\theta d\theta d\phi, \tag{3.15}$$

where SV_{syn} is the synthetic SV as determined from the induction equation and SV_{obs} is the radial component of secular variation from the observational model. The synthetic SV is truncated to the same spherical harmonic degree as the observed SV. The global minimum is simple to find as the target residual $\mathcal{R}_{\mathcal{N}+\mathcal{S}}$ is quadratic in the $2M + 1$ unknown coefficients and the optimum choice is uniquely determined.

Fig. 3.20 shows the structure of the inferred jet in 2020 using CHAOS-7.8 defined with $M = 1$, which is described by just three unknown coefficients with $\delta = 0.12$.

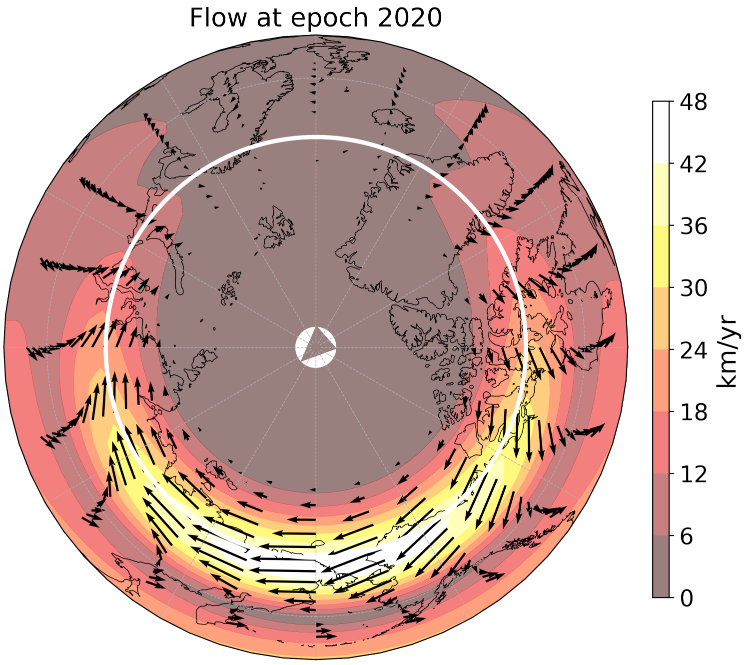

Figure 3.20: Snapshot of the fitted jet flow in 2020.0 based on the geomagnetic field model CHAOS-7.8.

Figure 3.21 shows the time-dependence of the best-fit jet (assuming $M = 1$ and $\delta = 0.12$) in terms of the longitudinal position and strength of the maximum flow, for different truncations of SV. All values of truncation shown $L = 13, 15, 16, 17$ show an increase in jet speed up to the present day, with maximum values of about 50 km/yr. Higher truncations give higher speeds. However, there is not a clear consensus in terms of the behaviour of the jet's central longitude. At $L = 17$ the model shows that the jet has been stationary at about 175°E over the last two decades, while the lower truncations show that the jet's centre has been moving westwards by about 1° per year. Because $L = 17$ is on the edge of what is resolvable in CHAOS-7, the model at $L = 16$ is the most trustworthy and agrees with the models at slightly lower truncation.

Conclusions

Changes in the magnetic field structure at high latitude led to the hypothesis of an accelerating westwards jet (2000-2016) around the projection of the tangent cylinder (Livermore et al, 2017). New geomagnetic field models, using Swarm data up to 2021, show that the recent changes are consistent with a continued acceleration of the jet up to 50 km/yr, whose centre is drifting westwards slowly at a rate of about 1° per year.

3.6 Analysis of jet features in numerical models

4DEarth_Swarm_Core ESA project deliverable R-H.2

P. Livermore
University of Leeds

Following the discussion about an observational signature of high-latitude jets, we now investigate numerical models for similar features. Of particular note is that the geodynamo models of Schaeffer et al (2017) have strong westward-directed flow near the north pole. Figure 3.22 shows two illustrative snapshots of the flow to degree 30, taken from models S1 and S2 of Schaeffer et al (2017) which have both been rescaled to dimensional velocities by the method of Lhuillier et al (2011). The flow is depicted just underneath the core-mantle-boundary as the models obey a non-slip condition at the boundary. The maximum values of the flow are about 100 km/yr, about double what is inferred for the Earth, and are generally focussed within, rather than on, the tangent cylinder. It is of interest to quantify the SV that such a flow would generate if it occurred in the Earth in the present day, for comparison to the observed SV.

The frozen-flux approximation to the induction equation is

$$\dot{B}_r = -\boldsymbol{\nabla}_H \cdot (\mathbf{u}_H \, B_r) \tag{3.16}$$

where $\mathbf{u}_H$ is the horizontal component of flow, and B_r is taken to be the structure of the field from CHAOS-7 from epoch 2015 (avoiding any possible end effects) as shown in figure 3.23.

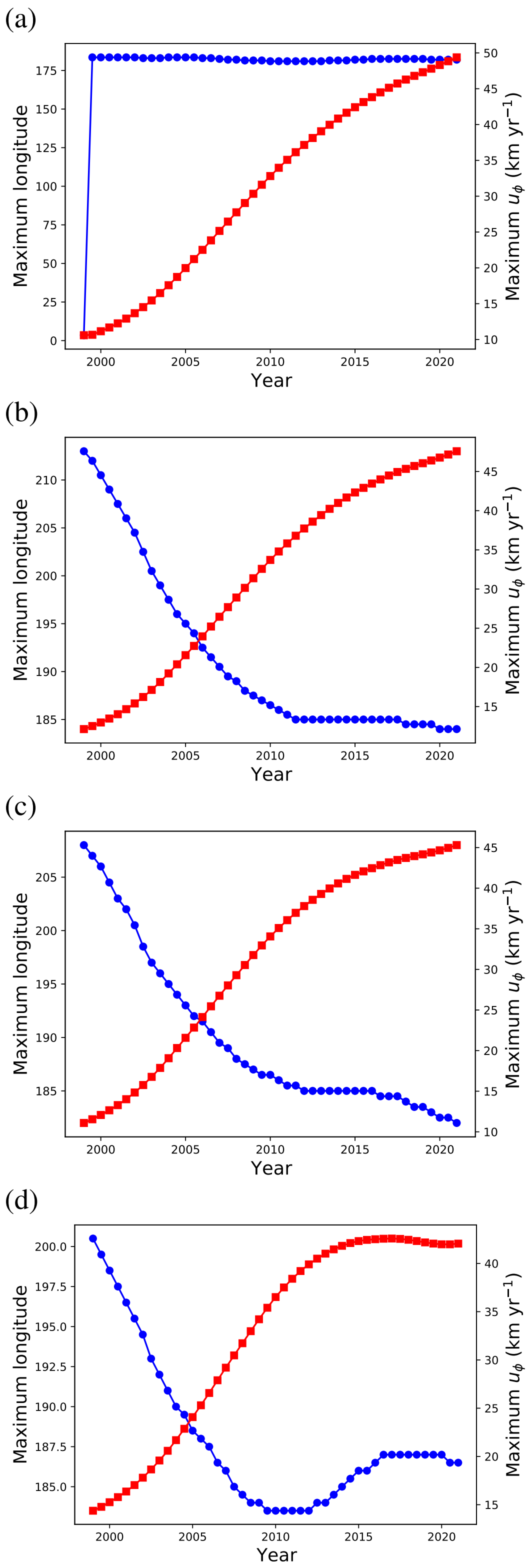

Figure 3.21: Time series of the jet maximum longitude and strength as a function of time, assuming CHAOS-7 using a main field at $L = 13$ and SV at (a) $L = 17$, (b) $L = 16$, (c) $L = 15$ and (d) $L = 13$.

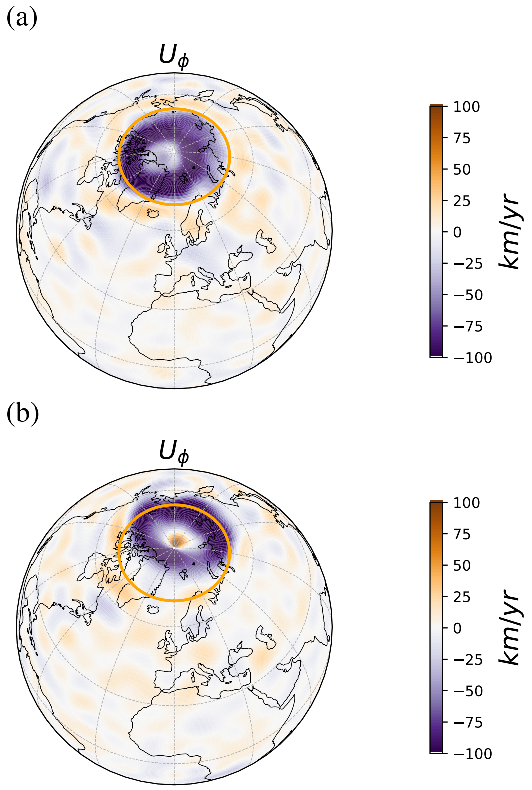

Figure 3.22: The azimuthal component of the flow from the S1 and S2 model. The orange circle shows the tangent cylinder.

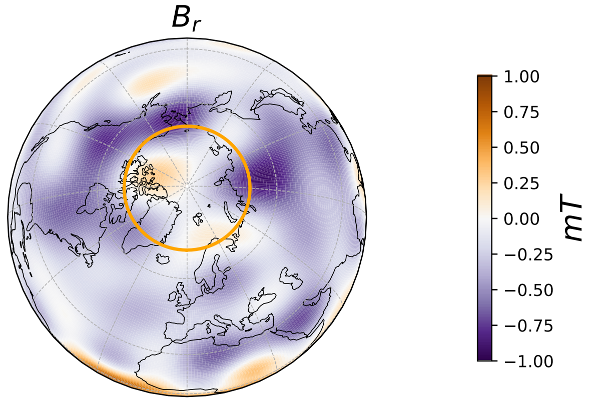

Figure 3.23: The radial field on the CMB in 2015 according to CHAOS-7. The orange circle shows the tangent cylinder.

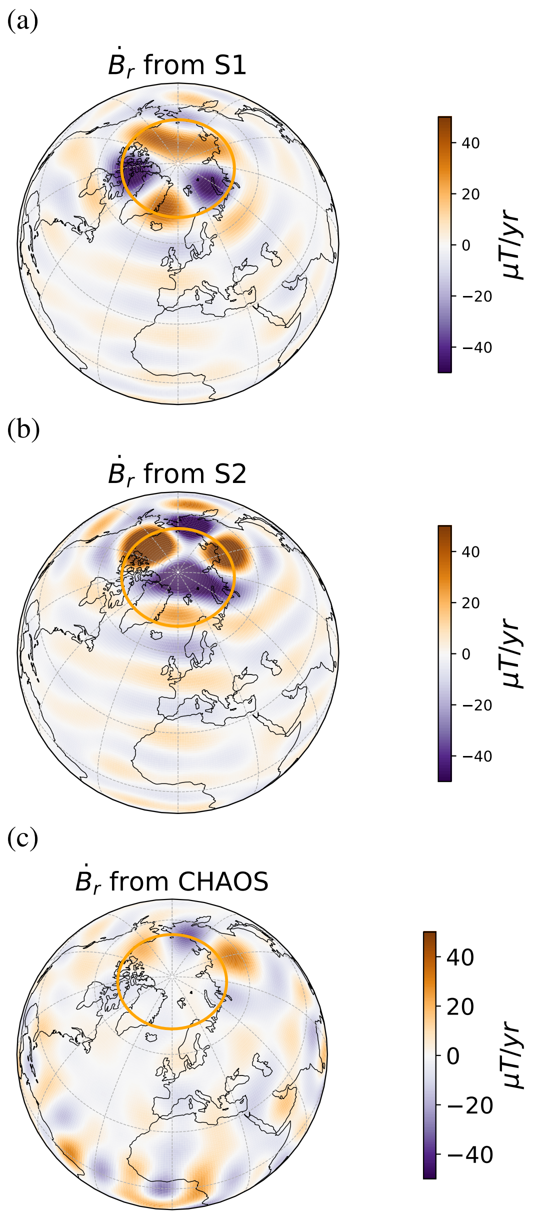

Figure 3.24: The instantaneous radial SV from models (a) S1 and (b) S2, assuming a magnetic field configuration taken from CHAOS-7 at epoch 2015 to degree 13. The observed SV in 2015 according to CHAOS-7 is shown in (c). All figure parts show the SV to degree 16.

Parts (a) and (b) of figure 3.24 show a strikingly different pattern of SV: both show patches of alternating positive and negative signal but offset to each other. This difference is caused by the fact that flows S1 and S2 used have maxima in slightly different places. Flow S1 is largely confined inside the tangent cylinder, and creates a pattern of SV by advecting the polar flux patches inside the tangent cylinder. Flow S2 is offset and has high speeds both on and slightly outside of the tangent cylinder at around 180°E. For this model, the high-latitude flux patches outside the tangent cylinder are advected, creating a similar signature to the present day-SV in this region. However, the flow S2 closes within the tangent cylinder, causing strong polar SV around 0°E which is not seen in the geomagnetic field.

The circumpolar structure of the westwards-directed flow S2 thus creates a signature comparable to the geodynamo around 180°E, but the stark difference around 0°E means that it is unable to explain the observed SV. The high-latitude structure in both models S1 and S2 is driven by thermal winds, so perhaps this mechanism is not that occurring in Earth to drive the observed pattern of SV. By comparison, the high-latitude jet of Livermore et al (2017) is not circumpolar and is localised in azimuth, and requires a return flow which is not confined to high-latitude.

3.7 Jet evolution of decadal timescales

4DEarth_Swarm_Core ESA project deliverable R-H.3

P. Livermore
University of Leeds

3.7.1 High latitude jets in core-flow inversions

The study of Livermore et al (2017) proposed a westwards-directed high latitude jet, based on a localised fit to geomagnetic field change. The jet they propose largely agrees with other studies of core-flow inversion, and forms part of a global gyre that circulates fluid across the core from polar to equatorial regions (Pais and Jault, 2008; Gillet et al, 2015; Baerenzung et al, 2016). It is of interest to focus however on the changes to the high-latitude core-flow over the last decade.

The study of Gillet et al (2019) proposed a new core-flow model and investigated the behaviour at high latitudes, and showed that the flow in the northern polar region attained strong values of up to 40 km/yr around 2010, similar to the proposed jet at 2016, although with only a small acceleration. Since 2010, the model shows a decline in high-latitude flow speed, which is not consistent with the localised analysis of deliverable R-H.1. Similar conclusions were reached by Bärenzung et al (2018), who showed in their flow model a decadal increase to about 25 km/yr at northern high-latitudes, but post 2010 a decrease.

Since all flow inversions are inferred from secular variation, it is therefore of interest to look in detail at the recent changes of high-latitude SV.

3.7.2 Current trends of high latitude secular variation

The northern high latitude region is the site of some of the largest secular variation on the core-mantle boundary (see figure 3.25) identifiable from global field models such as CHAOS-7.7 (Finlay et al, 2020). The SV forms a distinctive daisy-chain structure around the tangent cylinder, the imaginary cylinder coaxial with the Earth's rotation axis and tangent to the solid inner core (as marked in orange at a latitude of about 69° N on figure 3.25). Over the course of the last twenty years, the figure shows that the high latitude SV has strengthened, particularly in the band between 60-80°N, which according to the CHAOS-6 model between 1999 and 2016 may have been caused by an accelerating westwards jet (Livermore et al, 2017) localised to northern high-latitude. Part (d) of the figure shows that the trend of strengthening SV continues up to 2020, which suggests that high latitude flows may still be accelerating.

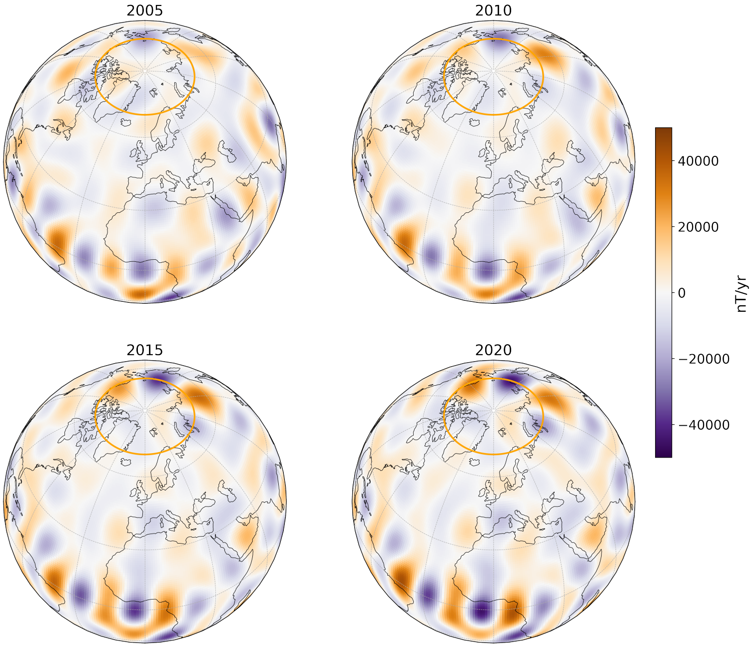

Figure 3.25: Snapshots of radial secular variation 2005-2020 on the core-mantle boundary at degree 17 according to CHAOS-7.7. The intersection of the tangent cylinder with the CMB is marked on in orange.

To investigate the structure of the high latitude SV over the last few years, restricting attention to 60-80°N (i.e. 10-30 degrees colatitude) and for all longitudes, figure 3.26(a) shows the maximum absolute radial secular variation for degrees 13

– 17, from the CHAOS-7.7 model. For the same magnetic field structure, higher values of SV would in general require a faster flow (assuming frozen-flux) to explain it, so the maximum value of SV is in this sense a proxy for the local flow speed. As expected, higher truncations (i.e. more structure) show higher maxima at any specific time, and for degrees 16 and 17 there is a monotonically increasing trend of SV from 1999 to 2021. For degree 13, the degree to which the main geomagnetic field can be imaged, the increasing trend 1999-2015 changes to one which is quasi-steady from 2015 onwards. Figure 3.26(b) shows the equivalent plot but for the southern polar region. Interestingly the general trend is decreasing with time, rather than increasing. Importantly, for the majority of the era 1999 onwards, the maxima are much smaller (about a quarter) compared to those in the north, suggesting that the local flow is much weaker in the southern polar region.

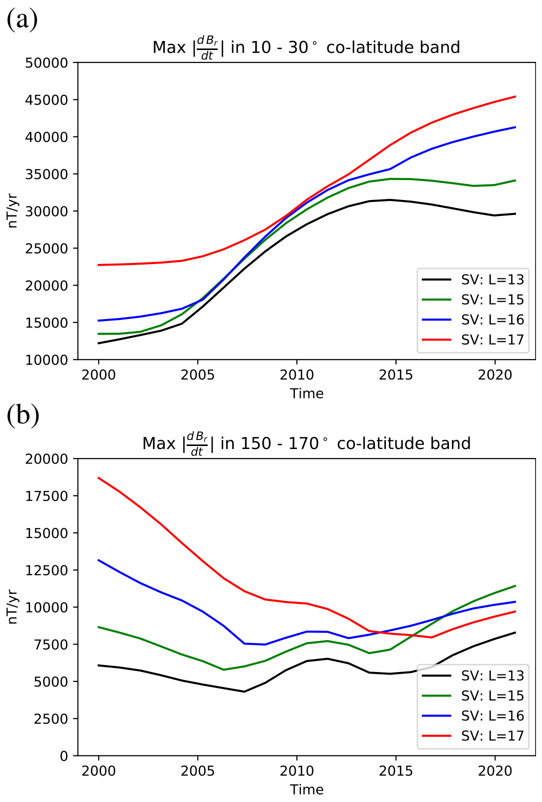

Figure 3.26: The variation of maximum absolute values of radial secular variation with time according to CHAOS-7.7, for different truncations, in the northern polar latitude band 60-80°N (a) and for the equivalent southern polar band (b).

To assess the robustness between models of the increasing trend of SV at high latitude, figure 3.27 presents a comparison between the CHAOS-7.7 model (Finlay et al, 2020) and Kalmag (Baerenzung et al, 2020), built using very different frameworks. Although CHAOS-7.7 has stable SV up to degree 17, Kalmag has stable SV only to degree 16, hence we have restricted both models to this resolution. The figure shows that both models agree well for the majority of 1999 onwards for degree 13. At degree 16, the two models largely agree until about 2016 when they begin to diverge: the Kalmag model showing a decrease in the maximum SV, compared with CHAOS-7.7 which shows a continual increase. Thus although based on comparable data, the two models do not agree on the trend of high latitude SV within the last few years at degree 16.

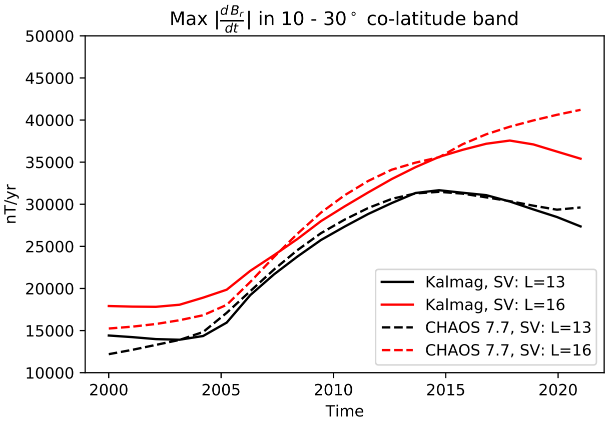

Figure 3.27: A comparison of the maximum absolute secular variation at high latitude (10-30° co latitude) for the Kalmag and CHAOS-7.7 models at degrees 13 and 16.

Compared to CHAOS-7.7, the Kalmag model produces more moderate SV towards the end of the model, particularly at high degree. This could be due to one of three reasons: (i) CHAOS-7.7 systematically overestimates, (ii) Kalmag systematically underestimates, or (iii) by chance: the specific structure of the raw dataset on which both models are based towards 2020 causes a one-off divergence in the models that is not due to any systematic bias. To investigate this, figure 3.28 shows the maximum absolute radial secular variation for Kalmag, CHAOS 7.7, and Kalmag model variants constructed by stopping the assimilation of data in 2018.0, 2019.0 and 2020.0 (courtesy J. Barenzung), defined respectively up to 2018, 2019 and 2020. All models show that an early truncation of the data causes lower values of the maximum SV; for example, the model constructed with data up to 2019 shows increased SV up to 2018 compared with the model constructed using data only up to 2018. Figure 3.29 shows the SV power up to degrees 13 and 16: again the absence of data has a significant effect on the power close to the end of the timeseries, particularly at $l = 16$.

The Kalmag model provides a distribution with associated error for each Gauss

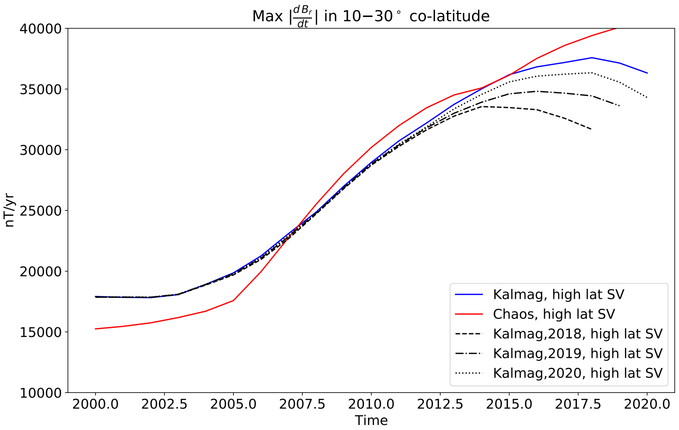

Figure 3.28: A comparison of the SV power up to degree $l = 16$ for CHAOS-7.7, Kalmag, and Kalmag variants constructed by stopping the assimilation of data in 2018.0, 2019.0 and 2020.0.

coefficient, and is constructed using a second order auto regressive methodology for the SV. Because there is nothing known a priori about the sign of any SV Gauss coefficient, in the model each coefficient is characterized by a zero mean in the absence of data. Because of the way the model is constructed, the model coefficients have a non-temporally-local dependence on the data. Towards the end points of the model when the data constraints are less, the model always reports values of SV closer to zero than it might otherwise, effectively under-estimating the SV. This end-effect apparently occurs about 4 years before the model end at $l = 13$ and about 8 years at $l = 16$. For example, the power in SV to degree 13 at 2015 might be estimated by any of the curves in figure 3.29, all of which contain data beyond 2015. Yet the curve obtained by including data to 2019 shows a higher value than that containing data only to 2018; the curve obtained by using data to 2020 is similar to that for 2019, suggesting that the value for 2015 is now converged: but requires data 4 years beyond the target date. Thus the Kalmag models (to degree 13) systematically appear to provide only lower bounds of maximum secular variation within 4 years of their end date: thus we cannot use Kalmag to estimate the maximum SV using data to 2020 from 2016 onwards.

To contrast this with the CHAOS models, figure 3.30 shows a variety of the CHAOS variants plotted over their defined time windows, along with CM6 (Sabaka et al, 2020). The models do not exactly agree because of the slightly different choices in model configuration and data selection, but they all show a consistent upwards trend with no decrease in recent years. In CHAOS-7.7 the model is fit using a penalised least-squares method, regularised by the 3rd time derivative of the field over the model duration, and by the second time derivative at the end points

(a)

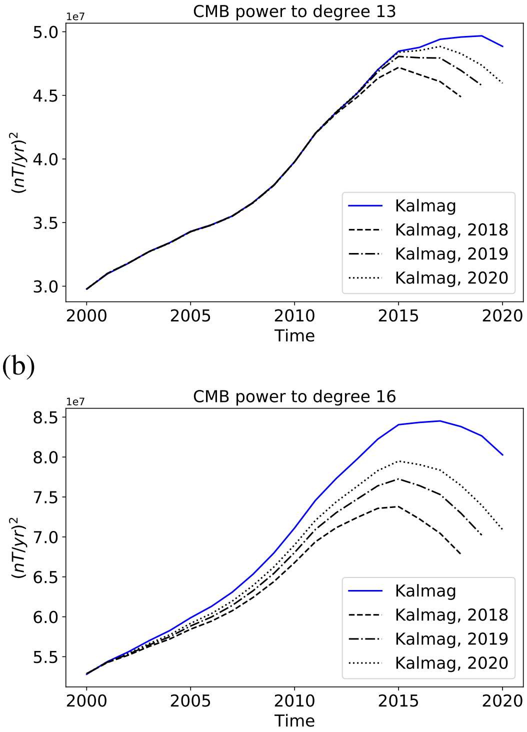

Figure 3.29: A comparison of the SV power up to degrees (a) $l = 13$ and (b) $l = 16$ for Kalmag, and Kalmag variants constructed by stopping the assimilation of data in 2018.0, 2019.0 and 2020.0.

at 1997.1 and 2020.1. Thus the SA is damped towards the end points meaning that the SV will favour constant values in the presence of fewer data. Evidence of smaller SA at 2020 can be seen in figure 3.31, although we note that the smaller values of SA at 2020 could be data-driven (there is no way to tell). Overall, any model bias of CHAOS-7.7 at the end points is towards constant SV, but even this appears to be slight and temporally localised (figure 3.30 shows no systematic end point effects). Kalmag biases models towards zero SV within a 5 year vicinity of the end points, and is therefore not a useful indicator of present-day SV.

In conclusion, end point affects can be very important when the core-flow model is sensitive to high values of SV. The Kalmag model cannot be used for localised high-latitude flow estimation within about 8 years of the end-point epoch.

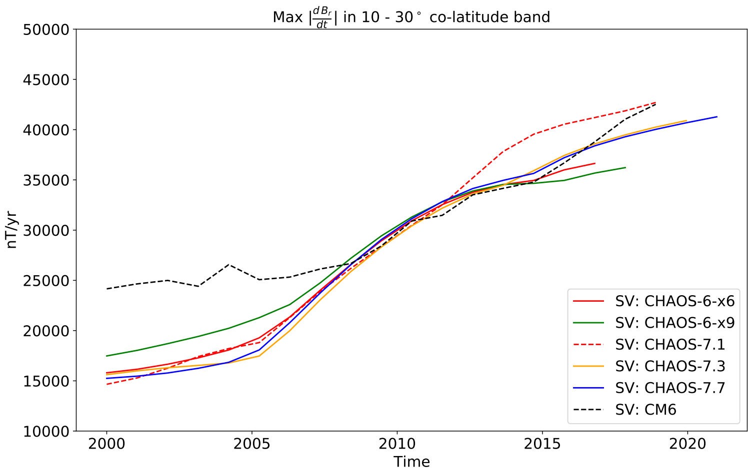

Figure 3.30: A comparison of the maximum radial secular variation in the CHAOS models compared with CM6.

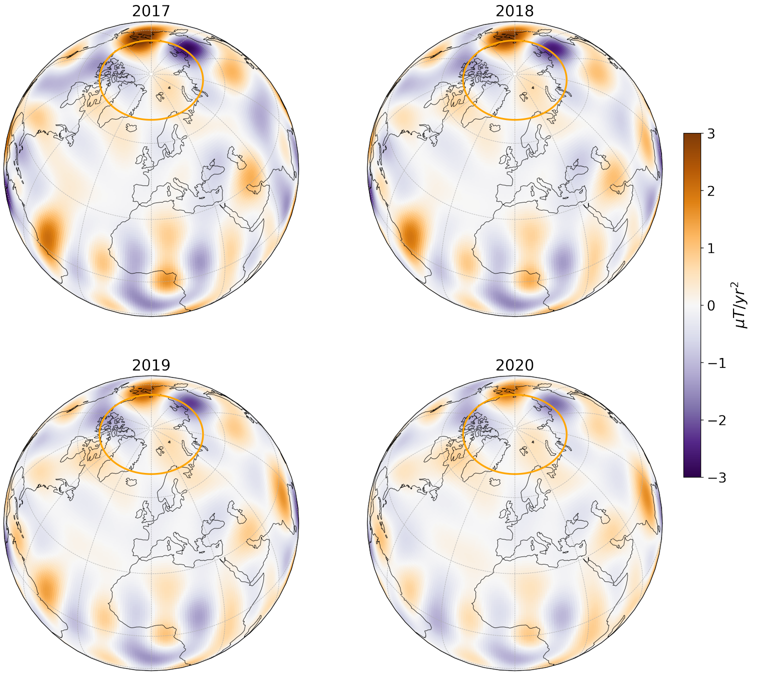

Figure 3.31: Snapshots of radial magnetic field acceleration 2017-2020 on the core-mantle boundary at degree 15 according to CHAOS-7.7. The intersection of the tangent cylinder with the CMB is marked on in orange.

Bibliography

Baerenzung J, Holschneider M, Lesur V (2016) The flow at the earth's core-mantle boundary under weak prior constraints. J Geophys Res: Solid Earth 121(3):1343–1364

Baerenzung J, Holschneider M, Wicht J, Lesur V, Sanchez S (2020) The kalmag model as a candidate for igrf-13. Earth, Planets and Space 72(1):1–13

Bärenzung J, Holschneider M, Wicht J, Sanchez S, Lesur V (2018) Modeling and predicting the short-term evolution of the geomagnetic field. Journal of Geophysical Research: Solid Earth 123(6):4539–4560

Finlay CC, Kloss C, Olsen N, Hammer MD, Tøffner-Clausen L, Grayver A, Kuvshinov A (2020) The chaos-7 geomagnetic field model and observed changes in the south atlantic anomaly. Earth, Planets and Space 72(1):1–31

Gillet N, Jault D, Finlay C (2015) Planetary gyre, time-dependent eddies, torsional waves, and equatorial jets at the earth's core surface. Journal of Geophysical Research: Solid Earth 120(6):3991–4013

Gillet N, Huder L, Aubert J (2019) A reduced stochastic model of core surface dynamics based on geodynamo simulations. Geophys J Int 219(1):522–539

Holme R (2015) Large scale flow in the core. In: Olson P, Schubert G (eds) Treatise in Geophysics, Core Dynamics, vol 8, Elsevier, chap 4, pp 91–113

Labbé F, Jault D, Gillet N (2015) On magnetostrophic inertia-less waves in quasi-geostrophic models of planetary cores. Geophys Astrophys Fluid Dyn 109(6):587–610

Lhuillier F, Fournier A, Hulot G, Aubert J (2011) The geomagnetic secular-variation timescale in observations and numerical dynamo models. Geophys Res Lett 38:L09,306

Livermore PW, Hollerbach R, Finlay CC (2017) An accelerating high-latitude jet in Earth's core. Nature Geoscience 10(1):62–68

Pais M, Jault D (2008) Quasi-geostrophic flows responsible for the secular variation of the Earth's magnetic field. Geophys J Int 173(2):421–443

Sabaka TJ, Tøffner-Clausen L, Olsen N, Finlay CC (2020) CM6: a comprehensive geomagnetic field model derived from both CHAMP and Swarm satellite observations. Earth, Planets and Space 72:1–24

Schaeffer N, Jault D, Nataf HC, Fournier A (2017) Turbulent geodynamo simulations: a leap towards Earth's core. Geophys J Int 211(1):1–29

Chapter 4

Quasi-geostrophic modeling

4.1 The QG model using the Lagrangian formalism

4DEarth_Swarm_Core ESA project deliverable R-F.1 and R-F.2

F. Gerick[1], D. Jault[1] and J. Noir[2]
[1]ISTerre Grenoble, [2]ETH Zurich

This deliverable is contained in the following publication: F. Gerick, D. Jault, J. Noir and J. Vidal, Pressure torque of torsional Alfvén modes acting on an ellipsoidal mantle, *Geophys. J. Int.*, 222(1), 2020, 338–351, https://doi.org/10.1093/gji/ggaa166

abstract:

We investigate the pressure torque between the fluid core and the solid mantle arising from magnetohydrodynamic modes in a rapidly rotating planetary core. A 2-D reduced model of the core fluid dynamics is developed to account for the non-spherical core–mantle boundary. The simplification of such a quasi-geostrophic model rests on the assumption of invariance of the equatorial components of the fluid velocity along the rotation axis. We use this model to investigate and quantify the axial torques of linear modes, focusing on the torsional Alfvén modes (TM) in an ellipsoid. We verify that the periods of these modes do not depend on the rotation frequency. Furthermore, they possess angular momentum resulting in a net pressure torque acting on the mantle. This torque scales linearly with the equatorial ellipticity. We estimate that for the TM calculated here topographic coupling to the mantle is too weak to account for the variations in the Earth's length-of-day.

4.2 Boundary conditions at the tangent cylinder for the quasi-geostrophic model

4DEarth_Swarm_Core ESA project deliverable R-G.1

L. CHEN[1], D. JAULT[1], P. W. LIVERMORE[2]
[1]ISTERRE GRENOBLE, [2]LEEDS UNIVERSITY

4.2.1 Introduction

Quasi-geostrophic (QG) motion describes the near balance between the pressure gradient and the Coriolis force when the inertia also contributes. In the Earth's outer core, the Alfvén torsional wave (TW) represents a type of axisymmetric QG motion that relates the fluctuation of the core flow to the background field (Jault and Finlay, 2015). Because TW has a period of approximately 6 years (Gillet et al, 2010), we can take advantage of the high-quality geomagnetic field data from satellite missions such as Swarm, and infer the core flow from there. An approximate solution for TW propagating in irregular domain can be derived assuming the change of cross section is gradual (Lighthill, 2001; Morse and Feshbach, 1953), and the amplitude of TW is given by

$$A(s,t) = \frac{C}{\sqrt{m V_A}} \exp\left[\pm i \int_{s_0}^{s} \frac{\omega}{V_A}\, \mathrm{d}s\right], \tag{4.1}$$

where s is the axial distance, $h = \sqrt{1 - s^2}$ is half-height of the geostrophic cylinder, $m = s^3 h$ is an auxiliary variable, ω is the frequency, and V_A is the Alfvén speed. One can easily see that this expression diverges when either $s \to 0$ or $h \to 0$. A less obvious location is the tangent cylinder (TC) where the geostrophic cylinder intersects with the inner core (IC). There are two related issues here: first, the profile of the IC causes the cross section to change so (4.1) may break down even if $s, h \neq 0$; second, the boundary condition at the tangent cylinder is not well understood. Since TC is not a solid barrier, (4.1) may not hold.

4.2.2 2D analytical model

We briefly considered 2D Cartesian models where the profile of the inner core can be ignored. The inner core is treated as a thin layer with negligible height, see Figure 4.1. However, QG flow is z invariant which means there is only one allowed TW solution on one side of TC ($x \geq b^+$), but there could be two separate solutions on the other side ($x \leq b^-$). This apparent discontinuity is difficult to overcome. One possible extension is to include the boundary layers. Even though previous studies have considered static shear layers (Livermore and Hollerbach, 2012), or simply a static boundary (Gillet et al, 2017), the boundary condition at TC remains

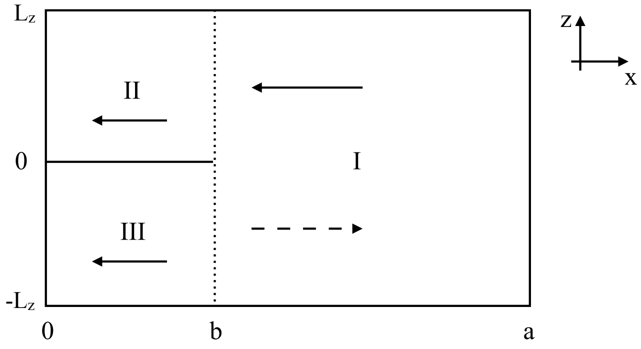

Figure 4.1: An illustration of 2D model with a thin flat inner core. Solution in region II and III are considered independent.

a bottleneck for travelling waves. As mentioned in the proposal for deliverable R-G, we switch to 3D numerical models for empirical data.

4.2.3 3D numerical models

We simulate the propagation of TW across TC in a spherical shell model with the fluid domain $[0.3509, 1]$ and the magnetic field domain $[0.05, 1.025]$. We use a Gaussian wave packet with rms width d. More details about the model set-up and main results are described in deliverable R-H. 4. We will only highlight the properties relevant to deliverable R-G.1 here. We find that actually 3D simulations do not support a localized boundary layer at TC. Instead, we find most wave energy has been transmitted, see Figure 4.4 for one example with a conducting inner core and a conducting lower mantle. When the background field has equatorial asymmetry, we could obtain two separate TW above and below the inner core, see Figure 4.5. The reflection remain weak for this case even though the rms width of the wave pulse is large. In general, we find thinner wave pulses are less reflected regardless of the magnetic diffusivity of the inner core or the mantle. For the complete data set, see Chen et al (in prep.).

4.2.4 Conclusion

We find through 3D numerical simulations (task overlaps with R-H. 4) that TW is mostly transmitted through TC. The reflection depends on the width of the wave pulse but remains weak for waves that are comparable or less wide than the inferred core flow (initial wave pulse has rms width $d \leq 0.2R$ where R is the core

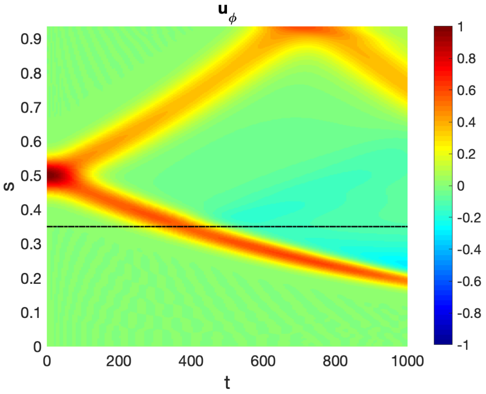

Figure 4.2: The u_ϕ profile at $z = 0.3509$ (just touches the top of the inner core) expressed in terms of the axial distance s and time t for run no.28, the inner core and the outer core magnetic diffusivity ratio $\eta_g/\eta = 1$, and the mantle and the outer core magnetic diffusivity ratio $\eta_m/\eta = 3.13 \times 10^{-5}$, $P_m = \nu/\eta = 0.04$, see deliverable R-H.4 for more details about the model set-up. Weak reflection is seen at TC (indicated by the dashed line) for this case.

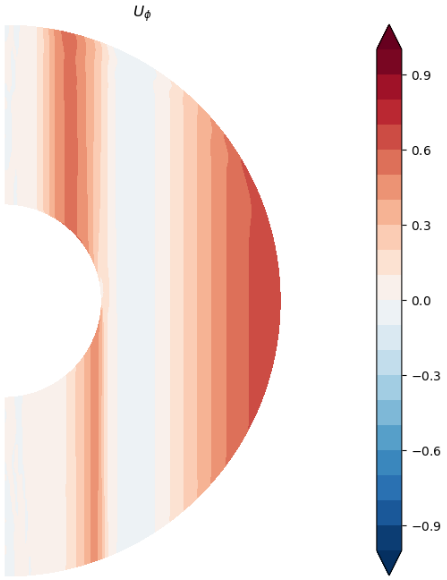

Figure 4.3: The u_ϕ profile at $t = 450$ for run no.36, $\eta_g/\eta = 1$, $\eta_m/\eta = 10^3$, $P_m = \nu/\eta = 0.04$, see section R-H.4 for more details about the model set-up. TW could split at TC under the influence of an equatorially asymmetric background field without an obvious static shear layer.

radius). The boundary condition at TC is not a localized "layer" as previously thought. Even though previous QG models did not address the inner core, we can still accept them as approximated solutions. There could be, however, hemispherical difference inside TC when the background field is equatorially asymmetric.

Bibliography

Chen L, Livermore PW, Jault D (in prep.) The effect of equatorially asymmetric background field on the torsional wave propagation in the Earth's core

Gillet N, Jault D, Canet E, Fournier A (2010) Fast torsional waves and strong magnetic field within the Earth's core. Nature 465(7294):74

Gillet N, Jault D, Canet E (2017) Excitation of travelling torsional normal modes in an earth's core model. Geophysical Journal International 210(3):1503–1516

Jault D, Finlay CC (2015) Waves in the core and mechanical core-mantle interactions. In: Schubert G, Olson P (eds) Treatise on Geophysics, Core Dynamics, 2nd edition, vol 8, Elsevier, Oxford, chap 8.09, pp 225–244

Lighthill J (2001) Waves in fluids. Cambridge Univ. Press

Livermore PW, Hollerbach R (2012) Successive elimination of shear layers by a hierarchy of constraints in inviscid spherical-shell flows. Journal of Mathematical Physics 53(7):073,104

Morse P, Feshbach H (1953) Methods of Theoretical Physics, no. v. 2 in International Series in Pure and Applied Physics. McGraw-Hill, Boston

4.3 QG Magneto-Coriolis modes matching a potential field at the core surface

4DEarth_Swarm_Core ESA project deliverable R-G.1

F. Gerick[1], D. Jault[1], J. Noir[2] and N. Gillet[1]
[1]ISTerre Grenoble, [2]ETH Zurich

This deliverable constitutes an extension to R-G.1. It concerns the discovery of QG Magneto-Coriolis modes on interannual periods, in a framework where the magnetic field satisfies the condition of a potential field at the core surface. It is contained in the following publication: F. Gerick, D. Jault and J. Noir, Fast Quasi-Geostrophic Magneto-Coriolis Modes in the Earth's Core , *Geophys. Res. Lett.*, 48, doi: https://doi.org/10.1029/2020GL090803 (2021)

abstract:

Fast changes of Earth's magnetic field could be explained by inviscid and diffusionless quasi-geostrophic (QG) Magneto-Coriolis modes. We present a hybrid QG model with columnar flows and three-dimensional magnetic fields and find modes with periods of a few years at parameters relevant to Earth's core. For the simple poloidal magnetic field that we consider here they show a localization of kinetic and magnetic energy in the equatorial region. This concentration of energy near the equator and the high frequency make them a plausible mechanism to explain similar features observed in recent geomagnetic field observations. Our model potentially opens a way to probe the otherwise inaccessible magnetic field structure in the Earth's outer core.

Furthermore, a discussion of QG MC modes, either solution to the eigenproblem or as retrieved in geodynamo simulations, can be found in the following review paper: N. Gillet, F. Gerick, R. Angappan and D. Jault, A dynamical prospective on interannual geomagnetic field changes, *Surveys in Geophysics* (accepted)

abstract:

Geomagnetic observations from satellites have highlighted interannual variations in the rate of change of the magnetic field originating from Earth's core. Downward continued to the core surface, these variations primarily show up in the equatorial belt. First, we recall the main characteristics of these patterns, addressing their spatio-temporal resolution, as seen from field models. We then review the several dynamical frameworks proposed so far to understand and model these observations, which populate the frequency spectrum on time-scales close to the Alfvén time $\tau_A \approx 2$ yr, much shorter than the vortex turn-over time $\tau_U \approx 150$ yr in Earth's core. Magnetic-Archimedes-Coriolis (MAC) waves in a stratified layer below the core surface constitute a first possibility in the case of a sub-adiabatic heat flux at the top of the core. Their period may reach the interannual range for a layer thickness less than ≈ 30 km, for a buoyancy frequency of the order of the Earth's rotation rate. An alternative has been proposed in a context where the Coriolis force dominates the momentum balance, rendering transient motions almost invariant along the rotation axis (quasi-geostrophy, QG). Torsional Alfvén waves, consisting of axisymmetric QG motions, operate at periods similar to the Alfvén time, but are not sufficient to explain the interannual field changes, that require non-axisymmetric motions. QG Alfvén waves (involving the Coriolis and magnetic forces) constitute another possibility, with inertia playing an important role. They have been detected in the latest generation of geodynamo simulations, propagating in an ubiquitous manner at a speed slightly less than the Alfvén velocity. They are localized in longitude and as a result their description requires high az-

imuthal wave number. But the branch of QG waves with large extent in azimuth is also worth considering, as it reaches interannual periods as their radial wavenumber is increased. The excitation of such high frequency dynamics is discussed with respect to the temporal spectrum of the core field, which presents a slope $\sim f^{-4}$ for periods approximately between τ_A and τ_U. We finally summarize the main geophysical implications of the existence of this interannual dynamics on core and lower mantle structure, properties, and dynamics.

4.4 On the use of the horizontal component of the induction equation in QG core flow reconstruction

4DEarth_Swarm_Core ESA project deliverable R-D.2

N. Gillet[1], D. Jault[1]
[1] ISTerre Grenoble

For recovering core surface flows, most studies so far have only considered the radial component of the induction equation at the core surface,

$$\frac{\partial B_r}{\partial t} = -\nabla_h \cdot (\mathbf{u}_h B_r) + \eta \nabla^2 B_r \,, \tag{4.2}$$

where $\mathbf{u}_h$ is the horizontal flow, B_r the radial field, and η the magnetic diffusivity (Holme, 2015). We use here spherical coordinates (r, θ, ϕ). The above equation is often considered as a linear problem, where the rate of change of B_r (or secular variation, SV) is stored in a vector $\mathsf{D}_r\dot{\mathbf{g}}$ (with D_r a radial derivation operator and $\dot{\mathbf{g}}$ SV Gauss coefficients), the flow is described by the vector of unknowns $\mathbf{x}^0$ (often toroidal and poloidal flow coefficients), so that equation (4.2) takes the form

$$\mathsf{D}_r\dot{\mathbf{g}} = \mathsf{A}_r^0\mathbf{x}^0 + \mathbf{e}_r \,, \tag{4.3}$$

with $\mathbf{e}_r$ an observation error vector (which may also account for diffusion and subgrid processes), and A_r a forward operator that depends on B_r, i.e. on the vector $\mathbf{g}$ that stores Gauss coefficients at the core surface. $\mathbf{g}$ and $\dot{\mathbf{g}}$ are considered as independent.

The main reason for neglecting the horizontal component is because, contrary to the radial component, it was thought to be discontinuous accross magnetic boundary layers below the core surface (Braginsky, 1984; Jault and Le Mouël, 1991). Furthermore, for an insulating mantle, all three components derive from the same potential above the core surface (of radius $r = c$), so that there is formally not more information contained in the entire field $\mathbf{B}$ than in its radial part B_r. Finally, it can be shown that the horizontal component of the magnetic field at the core surface is not only related to $\mathbf{u}_h$, but also to the radial shear $\partial_r\mathbf{u}_h$ below the core surface (Lloyd and Gubbins, 1990; Bloxham and Jackson, 1991). The horizontal induction equation takes the form

$$\mathsf{D}_h\dot{\mathbf{g}} = \mathsf{A}_h^0\mathbf{x}^0 + \mathsf{A}_h^1\mathbf{x}^1 + \mathbf{e}_h \,, \tag{4.4}$$

where the vector $\mathbf{x}^1$ stores coefficients for the radial shear below the surface, $\mathbf{e}_h$ is an error vector, operators A_h^1 and A_h^0 depend on $\mathbf{g}$, and D_h is the horizontal derivation operator. Then when adding a constraint from the horizontal induction equation, one also increases the number of unknowns.

However, the predominance of quasi-geostrophic (QG) flows in advanced geodynamo simulations (e.g., Aubert and Gillet, 2021) may lead to reconsider the situation. Indeed, QG motions being columnar, their description in the whole volume of the core is entirely set by their description either within the equatorial plane, or at the core surface. In the QG approximation, incompressible flow motions are defined by a stream function $\psi(s,\phi)$ that only depends on two spatial coordinates (Schaeffer and Cardin, 2005):

$$\mathbf{u}(s,\phi,z) = \nabla\psi \times \nabla\left(\frac{z}{H}\right) = \frac{1}{H}\nabla \times (\psi\mathbf{1}_z) + \frac{\beta z}{sH}\frac{\partial\psi}{\partial\phi}\mathbf{1}_z \,. \tag{4.5}$$

We use here cylindrical polar coordinates (s,ϕ,z). Then, knowing the flow at the surface, we also know its radial shear, and there exist a linear operator G such that

$$\mathbf{x}^1 = \mathsf{G}\mathbf{x}^0 \,, \tag{4.6}$$

so that Equation (4.4) can be formally re-written as

$$\mathsf{D}_h\dot{\mathbf{g}} = \left(\mathsf{A}_h^0 + \mathsf{A}_h^1\mathsf{G}\right)\mathbf{x}^0 + \mathbf{e}_h \,. \tag{4.7}$$

We end-up with a new constraint, but with the same number of unknowns as in the usual core flow inverse problem. This way we think it is possible to significantly improve the spatial resolution of core flow models. Implicitely, this approach assumes there is no magnetic boundary layer below the core surface, as suggested by the recent study of Magneto-Coriolis eigen-modes by Gerick et al (2021).

For an operational implementation, we nevertheless face several choices, that we list below.

1. A first alternative concerns the way one should use the information contained into (4.7). Either we consider it as an extra source of data (pretending we do not know that $\mathsf{D}_h\dot{\mathbf{g}}$ and $\mathsf{D}_r\dot{\mathbf{g}}$ come from the same Gauss coefficients), or we seek for the physical constraint to which (4.7) correspond. The latter appears more satisfying intellectually, and this is the one we would favor, as considering cross-covariances between the horizontal and radial components of the SV in $r = c$ would lead to a degenerated set of equations.

2. A second question should also be addressed: to which level shall we trust the constraints from (4.7)? Even though there has been an extensive research (e.g., Pais and Jault, 2008; Baerenzung et al, 2016; Gillet et al, 2019) concerning the relative importance of $\mathbf{e}_r$ in equation (4.3), the corresponding issue for $\mathbf{e}_h$ is an entirely open area.

3. A third issue that we must face is the choice of mathematical representation for the flow. A QG flow can be described through $\psi(s,\phi)$ in the equatorial plane, but the constraints due to the induction equation to be satisfied are naturally expressed at the spherical surface. The latter has been the most used so far, but the former (Maffei et al, 2017; Holdenried-Chernoff et al, 2020) presents the advantage to require one less spatial derivative (and this may be an advantage for numerical stability).

4. Last but not least, the absence of magnetic boundary layer would imply a single viscous layer for both **u** and **B**, carried by the flow. This may be justified in the limit where the magnetic Prandtl number $P_m = \nu/\eta \ll 1$ (with ν the kinematic viscosity), as the jump of **B** accross the layer evolves as $P_m^{1/2}$ for an insulating mantle (Schaeffer et al, 2012). However, this effect may bias interpretations based on dynamo simulations, where $\sqrt{P_m}$ is not so weak (≈ 0.09 in the 71%-path dynamo by Aubert and Gillet, 2021).

We have so far performed the numerical implementation and validation of the radial equation (4.3) while describing the unknowns in the equatorial plane. The implementation of the horizontal component is underway. This constitutes the PhD project of Ilya Firsov, who arrived at ISTerre in November 2020. Two scalars describe the field below the core surface (the toroidal T and poloidal S scalars), while only one is enough in $r = c$ (the potential field). Equation (4.7) is thus equivalent to two constraints:

1. a first one stating that there is no radial electrical current in $r = c$ (that impacts T);
2. a second one stating that the dynamo field must match a potential in $r = c$ (that impacts S).

This way we shall transform (4.7) into two constraints of the form

$$\begin{aligned} \mathsf{W}\dot{\mathbf{g}} &= \mathsf{Q}_S(\mathbf{g})\mathbf{x}^0 \,, \\ \mathbf{0} &= \mathsf{Q}_T(\mathbf{g})\mathbf{x}^0 \,. \end{aligned} \tag{4.8}$$

Once implemented numerically, while describing the flow through $\psi(s,\phi)$, it will be possible to invert (4.3) under the linear constraints (4.8). These shall be imposed using a weak formalism, in order to explore the impact of such constraints on the recovery of core motions. In principle, we foresee no technical difficulty. However, the recovered solutions might be very sensitive to the degree of satisfaction for the above constraints. This very issue might be tested and validated using outputs from geodynamo simulations the closer to Earth conditions.

Bibliography

Aubert J, Gillet N (2021) The interplay of fast waves and slow convection in geodynamo simulations nearing earth‚Äôs core conditions. Geophys J Int DOI https://doi.org/10.1093/gji/ggab054

Baerenzung J, Holschneider M, Lesur V (2016) The flow at the earth's core-mantle boundary under weak prior constraints. J Geophys Res: Solid Earth 121(3):1343–1364

Bloxham J, Jackson A (1991) Fluid flow near the surface of earth's outer core. Reviews of Geophysics 29(1):97–120

Braginsky S (1984) Short-period geomagnetic secular variation. Geophysical & Astrophysical Fluid Dynamics 30(1-2):1–78

Gerick F, Jault D, Noir J (2021) Fast quasi-geostrophic magneto-coriolis modes in the earth's core. Geophys Res Lett p 2020GL090803

Gillet N, Huder L, Aubert J (2019) A reduced stochastic model of core surface dynamics based on geodynamo simulations. Geophys J Int 219(1):522–539

Holdenried-Chernoff D, Maffei S, Jackson A (2020) The surface expression of deep columnar flows. Geochemistry, Geophysics, Geosystems 21(6):e2020GC009,039

Holme R (2015) Large scale flow in the core. In: Olson P, Schubert G (eds) Treatise in Geophysics, Core Dynamics, vol 8, Elsevier, chap 4, pp 91–113

Jault D, Le Mouël J (1991) Physical properties at the top of the core and core surface motions. Phys Earth Planet Int 68(1-2):76–84

Lloyd D, Gubbins D (1990) Toroidal fluid motion at the top of the earth's core. Geophysical Journal International 100(3):455–467

Maffei S, Jackson A, Livermore PW (2017) Characterization of columnar inertial modes in rapidly rotating spheres and spheroids. Proc R Soc A: Mathematical, Physical and Engineering Sciences 473(2204):20170,181

Pais M, Jault D (2008) Quasi-geostrophic flows responsible for the secular variation of the Earth's magnetic field. Geophys J Int 173(2):421–443

Schaeffer N, Cardin P (2005) Quasigeostrophic model of the instabilities of the Stewartson layer in flat and depth-varying containers. Physics of Fluids 17(10):104,111–104,111, DOI 10.1063/1.2073547

Schaeffer N, Jault D, Cardin P, Drouard M (2012) On the reflection of alfvén waves and its implication for earth's core modelling. Geophys J Int 191(2):508–516

4.5 Conductance of the lower mantle and reflection of torsional waves

4DEarth_Swarm_Core ESA project deliverable R-G.2

D. Jault
ISTerre Grenoble

Investigation of torsional waves and of their coupling with the electrically conducting mantle is rewarding by itself. We consider it equally as a necessary step before studying the influence of an electrically conducting mantle on the propagation of Magneto-Coriolis waves in the equatorial region of the fluid core. Hopefully, we will have more observational constraints on MC modes in the equatorial region than on torsional modes.

Non axially symmetric motions predominate indeed in the core surface velocities at subdecadal periods. In a recent work (Gillet et al, in rev.), we have interpreted these non-axisymmetric velocities as the signature of Magneto-Coriolis modes of low azimuthal wave numbers. The analysis rests on the CHAOS-7 field model based on satellite data for the last 20 years and the modes can be detected in the equatorial region of the core surface, where they have large latitudinal length scales. Similarly to the torsional waves, these modes consist of coupled velocities and magnetic fields. The velocities are quasi-geostrophic and the magnetic field matches with a potential field at the core mantle boundary, as appropriate for an insulating mantle (see also report R-F.1 and Gerick et al, 2021). The study gives an approximate dispersion relation for the Magneto-Coriolis modes that generalizes the dispersion relationship for torsional waves.

Torsional waves are special Alfvén waves. As such, they show equipartition of kinetic and of magnetic energy. The velocity component of a torsional wave is geostrophic and its amplitude depends only on the distance s to the rotation axis. According to 3D numerical simulations, the reflection of the wave at the equator depends on the magnetic Prandtl number $P_m = \nu/\eta$ (where ν is the kinematic viscosity and η the magnetic diffusivity) and on a parameter that we will denote Q and that is function of the electrical conductivity of the lower mantle:

$$Q = \sqrt{\frac{\mu_0}{\rho}} B_0 \int_{\text{mantle}} \sigma(r) \mathrm{d}r \tag{4.9}$$

where B_0 is the radial component of the magnetic field at the core-mantle boundary next to the equator and $\sigma(r)$ is the electrical conductivity of the mantle. Schaeffer et al (2012) and Schaeffer and Jault (2016) found an analogy between the reflection of Alfvén waves on a flat wall and the reflection of torsional waves in a spherical shell at the equator of the outer boundary. There is full absorption for either $P_m = 1$ of $Q = 1$. Above these values, the reflected wave has a different sign from the incoming wave. The influence of P_m is important inasmuch we are interested in numerical simulations of the geodynamo, for which P_m is often $O(1)$. Conversely, P_m is $O(10^{-6})$ in planetary cores and we do not expect this parameter to govern the reflection of torsional waves in the Earth's core. We can assume that the reflection of torsional waves is governed by the electrical conductivity of the mantle, as measured by the parameter Q. Gillet et al (2017) estimated it from the amplitude of the axisymmetric motions at the core surface and the value of the torque needed to account for the observed variations in the length of the day at subdecadal periods. They found $Q \sim 0.3$. Using this value of Q, they built time series of geostrophic motions that obey the 1D torsional wave equation and found that they compare well with the time series of axisymmetric motions inverted from geomagnetic data.

The analysis of Gillet et al (2017) relies on the validity of the 1D equation governing the torsional waves. They find that the reflection does not occur suddenly at the equator but progressively as the height of the tangent cylinder H vanishes, $H \to 0$ as $s \to 1$, where s is the distance to the rotation axis and the core radius is the unit of length. Gillet et al (2017) benchmarked the 1D simulations against the results of Schaeffer and Jault (2016). They found good agreement for $Q \leq 1$, including total absorption at $Q = 1$, but poor agreement for $Q \gtrsim 3$. This cast some doubt on the 1D-modelling. In addition, the 1D model did not capture well the change in the reflection coefficient as a function of P_m.

In this study, we first observe that $P_m^{1/2}$ and Q play exactly the same role in the 1-D equation. We also put forward an explanation for the ineffectiveness of the torsional wave model when Q or P_m are $O(1)$ or larger. The model leaves aside the mechanism by which the magnetic and velocity fields satisfy their respective boundary conditions at the fluid-solid interface. The difficulty can be circumvented when either $Q \ll 1$ or $Q \gg 1$ because then either the magnetic field is enslaved to the velocity field or vice-versa. When $Q \gg 1$, the boundary condition bears on the velocity $u_G(s)$, which has to vanish at the equator, $\lim_{s\to 1} u_G(s) = 0$. Because the velocity we invert from magnetic data does not satisfy this condition, we conclude $Q < 1$.

4.5.1 Hartmann layer, torsional wave equation as a function of P_m

Schaeffer et al (2012) used as reference case one-dimensional Alfvén waves transverse to a uniform magnetic field $\mathbf{B}_0$ reflecting on a plane perpendicular to the background field. Then, there is symmetry between the equations for the velocity and magnetic fields:

$$\begin{aligned}\frac{\partial u}{\partial t} &= \frac{\partial b}{\partial x} + \frac{P_m^{1/2}}{Ha}\frac{\partial^2 u}{\partial x^2}\\ \frac{\partial b}{\partial t} &= \frac{\partial u}{\partial x} + \frac{P_m^{-1/2}}{Ha}\frac{\partial^2 b}{\partial x^2}\end{aligned} \tag{4.10}$$

where the magnetic field has been scaled to Alfvén wave unit ($V_A = B_0/\sqrt{\mu_0\rho}$), Ha is the Hartmann number $Ha = B_0 L/\sqrt(\mu_0\rho\eta\nu)$ and L a typical length scale. Then, we can introduce the Elsasser variables $h_\pm = u \pm b$. We have

$$\frac{\partial h_\pm}{\partial t} = \pm\frac{\partial h_\pm}{\partial x} + \frac{P_m^{1/2} + P_m^{-1/2}}{2Ha}\frac{\partial^2 h_\pm}{\partial x^2} + \frac{P_m^{1/2} - P_m^{-1/2}}{2Ha}\frac{\partial^2 h_\mp}{\partial x^2} \tag{4.11}$$

We assume $S \gg 1$. Outside the boundary Hartmann layer, we obtain the d'Alembert equation

$$\frac{\partial h^\pm}{\partial t} = \pm\frac{\partial h^\pm}{\partial s} \tag{4.12}$$

with solution

$$h_\pm = h_0 \exp(\mathrm{i}k(x \pm t)) \tag{4.13}$$

If we consider the fluid domain $x \geq 0$, with the wall at $x = 0$, h_- represents the incoming wave and h_+ the reflected wave. For $P_m = 1$, the equations for h_+ and h_- are independent. There is no transformation from h_- into h_+ and the incoming wave is fully absorbed at $x = 0$. Schaeffer et al (2012) drew a parallel between the plane tangent to spherical core-mantle boundary and a flat wall. As a matter of fact, there is a nice agreement between the reflection coefficient predicted from the flat wall model and the coefficient estimated from numerical simulations in a spherical shell.

In order to calculate the reflection coefficient on a flat wall, we have to look at the solution within the boundary layer. There, we can neglect the spatial derivatives in comparison with the time derivative. Using L^{-1} as dimension for the wave number, we find

$$u, b \propto \exp\left(-Ha\, x\right), \qquad b = P_m^{1/2} u. \tag{4.14}$$

For $P_m \ll 1$, the jump in the magnetic field across the boundary layer is negligible in comparison with its value in the interior and the boundary layer accomodates only a change in the velocity. For $P_m \gg 1$, the situation is the opposite. From the expressions for the velocity and magnetic fields in the interior and in the boundary layer and the boundary conditions ($u = 0$, $b = 0$) at $x = 0$, we obtain:

$$u_1 = \frac{1 - P_m^{1/2}}{1 + P_m^{1/2}} u_0 \tag{4.15}$$

where u_0 is the amplitude of the incoming wave and u_1 the amplitude of the outgoing wave. There is a perfect symmetry between the velocity and the magnetic fields that is lost in the equation for the propagation of torsional wave.

We derive the equations for torsional waves assuming the magnetic field is enslaved to the velocity field. We shall use the values for the Earth's core as a guide for our model, allowing only for a change in P_m. Taking into account the actual value of the radial magnetic field and the Earth's rotation rate, the boundary layer away from the equator is an Ekman viscous boundary layer slightly modified in the presence of the magnetic field. Because the Earth's rotation rate $\boldsymbol{\Omega}$ enters this description through its component normal to the boundary, the Ekman Hartmann viscous boundary layer transforms into an ordinary Hartmann layer, next to $s = 1$, where s is the cylindrical radius. We choose the core radius as the unit of length and $s = 1$ at the equateur. The half-height of the geostrophic cylinder is denoted H with $s^2 + H^2 = 1$. It vanishes at the equator. Here, we restrict the study to the vicinity of $s = 1$.

Braginsky (1970) included a thin conducting layer at the bottom of the mantle in his study of torsional waves. Using dimensionless values, his expression for the magnetic field at the bottom of the mantle becomes

$$b_\phi(s, H) = -Q\,\mathrm{sgn}(B_r)u_\phi(s) \tag{4.16}$$

Similarly, the jump in the magnetic field is related to the jump in the velocity field as

$$b_\phi(s, H) = -P_m^{1/2}\,\mathrm{sgn}(B_r)u_\phi(s) \tag{4.17}$$

Thus, taking into account the finite value of $P_m^{1/2}$ or of Q modifies the torsional wave equation exactly in the same way.

4.5.2 Reflection of torsional waves in the sphere, analogy with Elsasser variables

The torsional wave equation is usually constructed using the geostrophic velocity $u(s)\mathbf{e}_\phi$ as primary variable. We can always transform this second-order wave equation into two coupled first-order equations. In the vicinity of $s = 1$, we can further simplify them by assuming that the magnetic field is uniform. Finally, we keep much of the interesting physics by considering only the axially-symmetric s-component $\mathbf{B} = B_s\mathbf{e}_s$ of the field, with B_s uniform. Then, we obtain

$$\begin{aligned} \frac{\partial u}{\partial t} &= \frac{1}{m}\frac{\partial (mb)}{\partial s} - \frac{Qu}{h^2} \\ \frac{\partial b}{\partial t} &= \frac{\partial u}{\partial s} \end{aligned} \tag{4.18}$$

with $m = s^3 h$ and $\{B_s^2\} = 1$. Here, b has been introduced as an auxiliary variable. The boundary term $-Qu/h^2$ accounts for all the variations of b_ϕ next to the core-mantle interface. Using $(1 - s) \ll 1$, the system of coupled equations can be transformed into

$$\begin{aligned} \frac{\partial u}{\partial t} &= \frac{\partial b}{\partial s} - \frac{b}{h^2} - \frac{Qu}{h^2} \\ \frac{\partial b}{\partial t} &= \frac{\partial u}{\partial s}. \end{aligned} \tag{4.19}$$

Gillet et al (2017) discussed the reflection of torsional waves at the equator using Elsasser variables, as introduced in the previous section

$$h^+ = u + b, \qquad h^- = u - b. \tag{4.20}$$

Using these variables, we have

$$\begin{aligned}\frac{\partial h^+}{\partial t} &= \frac{\partial h^+}{\partial s} - \frac{1}{2h^2}\left((1+Q)h^+ + (Q-1)h^-\right)\\ \frac{\partial h^-}{\partial t} &= -\frac{\partial h^-}{\partial s} - \frac{1}{2h^2}\left((1+Q)h^+ + (Q-1)h^-\right)\end{aligned} \tag{4.21}$$

or

$$\begin{aligned}\frac{\partial h^+}{\partial t} &= -\frac{\partial h^+}{\partial x} - \frac{1}{4x}\left((1+Q)h^+ + (Q-1)h^-\right)\\ \frac{\partial h^-}{\partial t} &= \frac{\partial h^-}{\partial x} - \frac{1}{4x}\left((1+Q)h^+ + (Q-1)h^-\right)\end{aligned} \tag{4.22}$$

with $x = 1 - s$. Again, the variable h^- represents the incoming wave $h^- \propto \exp(-\mathrm{i}k(x+t))$ and h^+ the reflected wave $h^+ \propto \exp(\mathrm{i}k(x-t))$. For $k \gg 1$ and $h = O(1)$ (away from the equator $h = 0$), h^+ and h^- evolve independently. As the wave nears $x = 0$, there is transformation of the incoming wave h^- into h^+ except if $Q = 1$. This explains the total absorption of the wave for $Q = 1$.

The transformation occurs progressively in the interior, not abruptly in the viscous layer attached to $x = 0$. The singularity disappears for

$$\lim_{x\to 0}\left(\frac{h^+}{h^-}\right) = \frac{1-Q}{1+Q}. \tag{4.23}$$

The coefficient is the same as for the reflection of plane waves on a flat wall, placed perpendicular to the direction of propagation.

The velocity and magnetic fields are prescribed by the torsional wave equation, independently of the boundary condition that relates this two fields. According to the classical approach, the velocity field is not affected by the boundary condition. As a result, the magnetic field at the core mantle boundary is enslaved to the velocity field. Although the exact mechanism by which the boundary condition is enforced is not well determined, the symmetry between the velocity and magnetic fields is broken.

In order to further illustrate this point, we can consider the case where P_m or Q for that matter is much larger than 1. Then, the discontinuity across the Hartmann layer is entirely magnetic. We discuss the equatorial region where we can take the background magnetic field as uniform. We allow for variation of the velocity field in the z-direction close to $z = \pm H$. As a result we redefine u as

$$u = \frac{1}{2H}\int_{-H}^{H} u_\phi \mathrm{d}z. \tag{4.24}$$

We further assume (in the equatorial region where the background field is uniform) that the magnetic field b_ϕ is function of s only, $b = b_\phi(s)$. Then, the coupled momentum and induction equations

$$\frac{\partial u}{\partial t} = B_s\frac{\partial b}{\partial s} \tag{4.25}$$

$$\frac{\partial b}{\partial t} = \frac{B_s}{H}\frac{\partial}{\partial s}(Hu) + \frac{1}{2H^2}\left(u_\phi(H) + u_\phi(-H)\right). \tag{4.26}$$

We end up with the same situation as before except that now $u_\phi(H)$ is prescribed by $b_\phi(s)$; we only have to replace Q by Q^{-1} and $P_m^{1/2}$ by $P_m^{-1/2}$. The reflection coefficient for the magnetic field, which is now our primary variable, is

$$\frac{1 - Q^{-1}}{1 + Q^{-1}} = -\frac{1 - Q}{1 + Q}. \tag{4.27}$$

This is the expected result as the reflection coefficient for the magnetic field is the opposite of the reflection coefficient for the velocity field.

4.5.3 Mantle electrical conductivity from time series of geostrophic and quasi-geostrophic motions

We have put the study of Gillet et al (2017) on a firmer ground but we have not revised the previous estimate of Q and of the mantle electrical conductivity:

$$Q = 0.3 \qquad 3 \times 10^7 \lesssim G \lesssim 10^8 S. \tag{4.28}$$

This gives a constraint on the maximum conductivity of the lowermost 100 km of the mantle, which is not much restricted by the mantle filter times (Jault and Finlay, 2015). Time changes of the core angular momentum estimated from the time series of the geostrophic velocity do balance the time changes of the mantle as inferred from length-of-day series. We would expect the agreement to be better still for the last 20 years when satellite data are available. As the time of writing this report, it is not yet the case (see Figure 10 in Gillet et al, 2019). As a result, we are not in a position to use the geostrophic motion time series to revise our estimate of Q.

Dumberry and More (2020) investigated the coupling between quasi-geostrophic motions in the Earth's core and lateral variations of the electrical conductivity in the lowermost mantle. They argued that the time changes in the magnetic field are the weakest next to the most conducting regions in the lower mantle. The interpretation is not direct as it relies on a quasi-geostrophic model defined in such a way that the radial component of the magnetic field is exactly zero at the core-mantle boundary (as in Labbé et al, 2015). Generalizing our study about the influence of the mantle conductivity on torsional waves to its effect on quasi-geostrophic Magneto-Coriolis modes may enable us to point at lateral variations in the conductivity next to the equator.

Bibliography

Braginsky S (1970) Torsional magnetohydrodynamics vibrations in the earth's core and variations in day length. Geomagn Aeron 10:3–12

Dumberry M, More C (2020) Weak magnetic field changes over the pacific due to high conductance in lowermost mantle. Nature Geoscience 13(7):516–520

Gerick F, Jault D, Noir J (2021) Fast quasi-geostrophic magneto-coriolis modes in the earth's core. Geophys Res Lett p 2020GL090803

Gillet N, Jault D, Canet E (2017) Excitation of travelling torsional normal modes in an earth's core model. Geophysical Journal International 210(3):1503–1516

Gillet N, Huder L, Aubert J (2019) A reduced stochastic model of core surface dynamics based on geodynamo simulations. Geophys J Int 219(1):522–539

Gillet N, Gerick F, Jault D, Schwaiger T, Aubert J, Istas M (in rev.) Satellite magnetic data reveal interannual modes in earth's core

Jault D, Finlay CC (2015) Waves in the core and mechanical core-mantle interactions. In: Schubert G, Olson P (eds) Treatise on Geophysics, Core Dynamics, 2nd edition, vol 8, Elsevier, Oxford, chap 8.09, pp 225–244

Labbé F, Jault D, Gillet N (2015) On magnetostrophic inertia-less waves in quasi-geostrophic models of planetary cores. Geophys Astrophys Fluid Dyn 109(6):587–610

Schaeffer N, Jault D (2016) Electrical conductivity of the lowermost mantle explains absorption of core torsional waves at the equator. Geophysical Research Letters 43(10):4922–4928

Schaeffer N, Jault D, Cardin P, Drouard M (2012) On the reflection of alfvén waves and its implication for earth's core modelling. Geophys J Int 191(2):508–516

4.6 The effect of equatorially asymmetric background field on the torsional wave propagation in the Earth's core

4DEarth_Swarm_Core ESA project deliverable R-H.4

L. Chen[1], P. W. Livermore[2] and D. Jault[1]
[1]ISTerre Grenoble, [2]Leeds University

4.6.1 Introduction

At decadal time scales, the fluid dynamics inside the Earth's core is strongly influenced by rotation. In this case, we can make quasi-geostrophic (QG) approximations where the flow is assumed to be invariant parallel to the rotational axis. The torsional wave (TW) describes the oscillations of a particular type of QG flow $\boldsymbol{u}$ and the perturbed magnetic field $\boldsymbol{b}$ as they interact with the background magnetic field $\boldsymbol{B}$ (Jault and Finlay, 2015). In cylindrical coordinates (s, z, ϕ), the TW equation is

$$\rho \frac{\partial^2 \omega_g}{\partial t^2} = \frac{1}{2\pi} \frac{1}{s^3 \mu_0} \frac{\partial}{\partial s} \left(s^3 \frac{\partial \omega_g}{\partial s} \{B_s^2\} \right), \tag{4.29}$$

where $u_\phi = s\omega_g$, and $\{B_s^2\} = (z_f - z_i)^{-1} \int_{z_i}^{z_f} \oint B_s^2 \,\mathrm{d}\phi \,\mathrm{d}z$ represents the averaged contribution from the background field to the geostrophic cylinder extends from z_i to z_f.

Across a special location called the tangent cylinder (TC) where the geostrophic cylinder intersects with the inner core, two types of core flows have been observed. Inside TC, high-latitude jets with a circular pattern (D-C.1) have been inferred using high-resolution geomagnetic observations from the Swarm satellite. The amplitude of the jets is much stronger than the typical inferred core flow. There is also a hemispherical difference where the Northern jet has a stronger signal. Outside TC, inversion models have shown TW propagates mostly outwardly towards the equator (Gillet et al, 2010, 2015). While it is possible for TW to be generated just outside TC (Teed et al, 2018)—hence explaining the outward flow pattern, it is also possible that TW has been generated elsewhere but gets strongly reflected at TC. Whether such a strong reflection occurs will undoubtedly constrain the fluid dynamics inside TC. Therefore, rather than directly studying the high-latitude jets, we focus on the propagation of TW across TC as a probe into the possible interaction between the core flow and the surrounding geomagnetic field.

4.6.2 3D simulations

Unlike previous models which studied TW reflection at the bottom of the mantle (Schaeffer et al, 2012; Schaeffer and Jault, 2016), at exactly TC we have just one point of contact with the solid inner core, and the rest is inside the fluid domain. This poses a challenge as the boundary condition becomes singular (see also R-G.1). We choose to run numerical simulations that allow boundary layers to form so the magnetic field can be kept continuous. We consider a forward axisymmetric model in a spherical shell using the XSHELLS code [1]. The fluid motion is controlled by the linearized Navier-Stokes equation and the induction equation given below:

$$\frac{\partial \boldsymbol{u}}{\partial t} + 2\Omega\hat{z}\times\boldsymbol{u} = -\nabla P + \nu\nabla^2\boldsymbol{u} + (\nabla\times\boldsymbol{b})\times\boldsymbol{B}, \tag{4.30}$$

$$\frac{\partial \boldsymbol{b}}{\partial t} = (\boldsymbol{u}\cdot\nabla)\boldsymbol{b} + \eta\nabla^2\boldsymbol{b}, \tag{4.31}$$

where Ω is the angular speed, P is the pressure, ν is the fluid viscosity, and η is the magnetic diffusivity. The solenoidal condition applies: $\nabla\cdot\boldsymbol{u} = \nabla\cdot\boldsymbol{b} = 0$. The fluid domain is $[0.3509, 1]$, and the magnetic field extends into the inner core and the mantle at $[0.05, 1.025]$. Most previous models about TW assumed an equatorially symmetric B_s. From various geomagnetic field models, e.g.Finlay et al (2020), it is clear that the B_s component is much more complex. Therefore, in this study, we also allow equatorial asymmetry from the background field. We use an externally sourced potential field,

$$\boldsymbol{B} = -\nabla V = -\sum_l C_l\nabla(r^lY_l^0), \tag{4.32}$$

where r is the radius, and Y_l^0 is the spherical harmonic function with degree l and order 0. We vary the coefficients of $l = 2$ and $l = 3$ modes to control the amount of asymmetry. The field component that contributes to TW is

$$B_s = -C_2\sqrt{\frac{5}{4\pi}}s - C_3\sqrt{\frac{7}{4\pi}}sz, \tag{4.33}$$

where C_2 and C_3 represent the equatorially symmetric and anti-symmetric part of B_s respectively, see Figure 4.4. The initial velocity is a Gaussian wave packet,

$$\boldsymbol{u}_\phi(t=0) = As^2(1-s)^2\exp\left[-\frac{(s-s_0)^2}{d^2}\right], \tag{4.34}$$

where A is adjusted such that the maximal amplitude of u_ϕ is normalized to 1 (Cox et al, 2013), and for most runs the initial perturbed magnetic field $b = 0$. The wave pulse is initially generated outside TC, and we run the simulation till the wave pulse has crossed TC if that is possible. The wave response inside TC would tell us about the possible link to the high-latitude jets, while the wave response outside TC would inform us about whether strong reflection is possible.

---

[1] https://www.bitbucket.org/nschaeff/xshells/

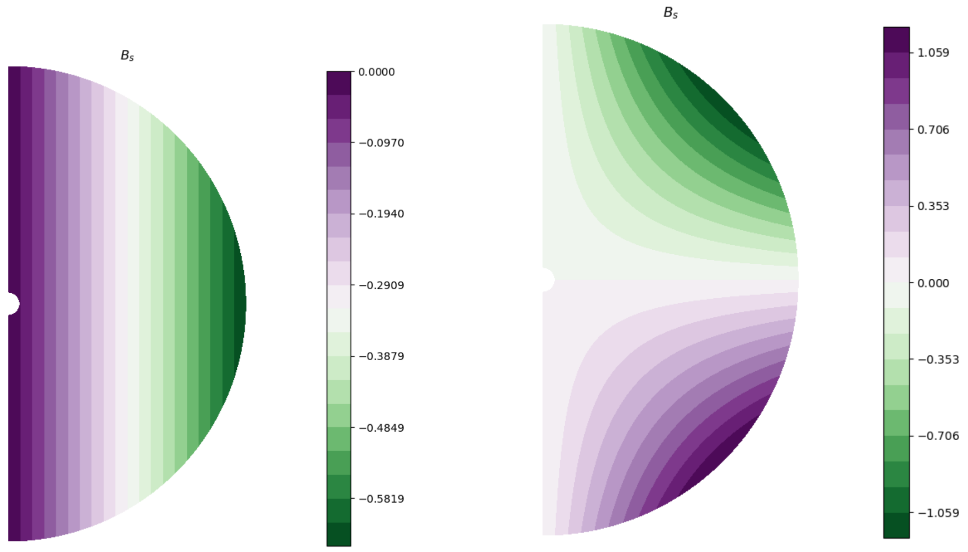

Figure 4.4: B_s component of the background field contains an equatorially symmetric part ($l = 2$) and an equatorially anti-symmetric part ($l = 3$). Left figure: $(C_2, C_3) = (1, 0)$ the quadrupole mode ($l = 2$). Right figure: $(C_2, C_3) = (0, 1)$ the octupole mode ($l = 3$).

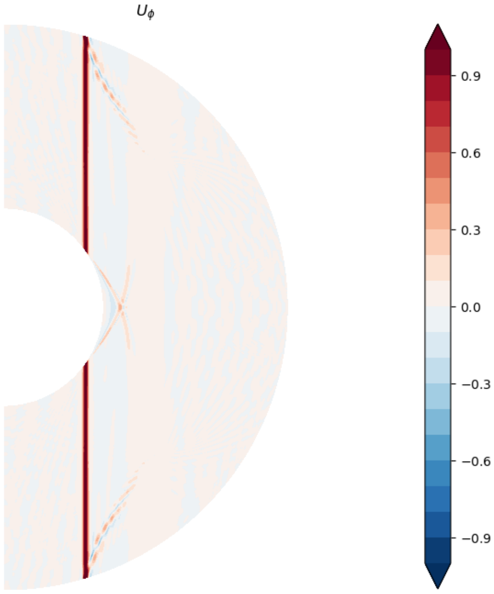

Figure 4.5: The u_ϕ profile at $t = 87.5$, run no.6 $(C_2, C_3) = (0.006, 0)$. The inner core magnetic diffusivity $\eta_g = \eta$, and the mantle magnetic diffusivity $\eta_m = 0$. We see the transient waves being emitted as TW passes by. The reflection at TC is weak for thin initial pulses.

4.6.3 Three types of background fields

In our simulations we have three cases based on the type of symmetry. The parameters for selected runs are given in Table 4.2. For the complete data set, see Chen et al (in prep.).

The equatorially symmetric case

Here we use just the $l = 2$ mode, i.e. $C_3 = 0$. The propagation of TW in this case is well understood in terms of Elsasser variables (Elsasser, 1946). However, the effect of boundary in a spherical shell is not clear as we demand the magnetic field to be continuous beyond the fluid domain. Previously it was thought that there could be a diffusion layer below the mantle to compensate for the discontinuity in TW. In contrary, we did not find such diffusive layer forming. We see a transient wave being emitted at the core mantle boundary, also at the equator when the TW pulse passes by, see Figure 4.5. We find weak reflection at TC that depends on the rms width of the wave packet, for example run no.5 and no.6, see Figure 4.6.

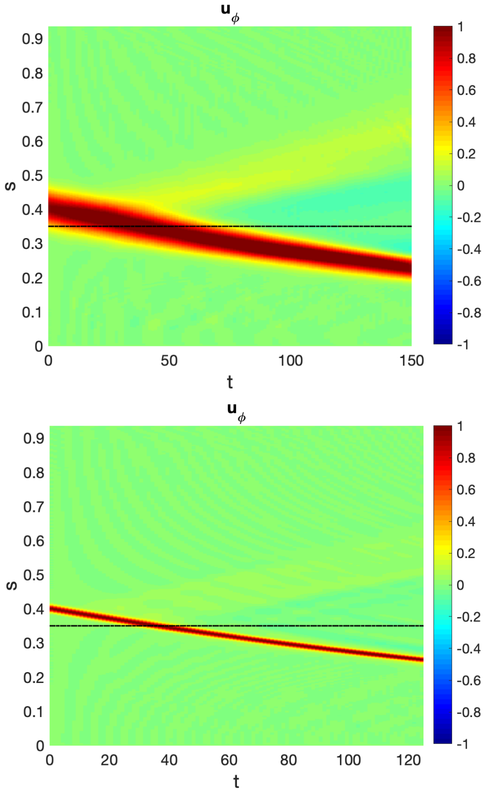

Figure 4.6: The u_ϕ profile at $z = 0.3509$ (just touches the top of the inner core) expressed in terms of the axial distance s and time t for run no.5 and no.6. Both have $(C_2, C_3) = (0.006, 0)$. The initial wave pulse has rms width $d = 0.05$ for no.5, but for no.6 $d = 0.01$. The reflection at TC (indicated by the dashed line) is weak but still differs in amplitude for these two runs.

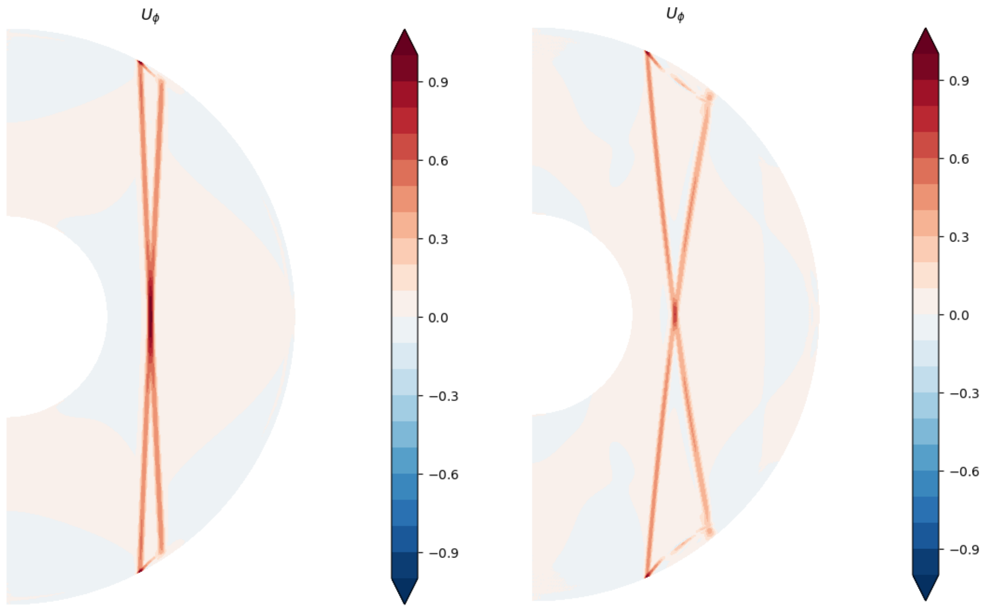

Figure 4.7: The u_ϕ profile for run no.9 with $(C_2, C_3) = (0, 0.016)$. The two arms open up as time goes by. Left figure: $t = 2.5$. Right figure: $t = 7.5$.

The equatorially anti-symmetric case

Here we use just the $l = 3$ mode, i.e. $C_2 = 0$. Interestingly, we observe two types of fluid regime. One exhibits TW as expected; the other produces a body wave that breaks down the QG assumption, which has not been studied before. The initial wave pulse splits into two crossing arms in the shape of an X, and then gradually open up, see Figure 4.7. When the arms open up, the center node is localized in space. If the initial pulse is generated inside TC, we still observe the opening up of the two arms without the center node, see Figure 4.8. The transition from TW to this X-shaped body wave depends on both the local length scale and the strength of the background field. Empirically we find the critical C_3/d ratio to be ~ 0.1 beyond which TW ceases to exist. In TW regime, very little reflection has been found for runs with $d \leq 0.02$.

The equatorially asymmetric case

Here we have both $l = 2$ and $l = 3$ modes. In our simulations, we find the amount of asymmetry and the local length scale matters for the QG assumption to hold. There is a transition point beyond which the z-invariance of the core flow breaks down, i.e. the perturbed velocity field $\boldsymbol{u}$ no longer aligns with the geostrophic cylinder, see Figure 4.9. The classic Lehnert number $\lambda = |B|/(\Omega \sqrt{\mu\rho}L)$ which

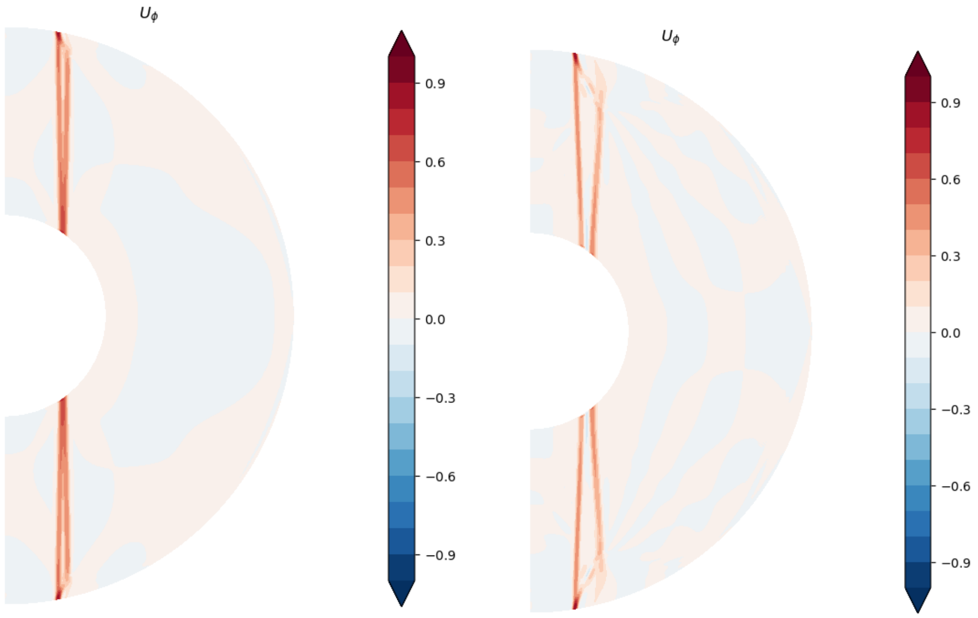

Figure 4.8: The u_ϕ profile for run no.13 with $(C_2, C_3) = (0, 0.008)$. Left figure: $t = 5$. Right figure: $t = 15$.

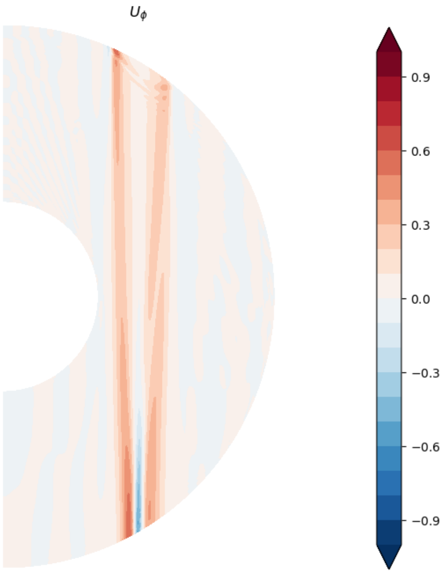

Figure 4.9: An example of non-QG flow. The u_ϕ profile at $t = 62.5$, run no.23 with $(C_2, C_3) = (3\times10^{-3}, 8\times10^{-4})$.

considers the overall background field strength $|B|$ and the size of the fluid domain L (the magnetic susceptibility μ and the density ρ are not relevant for this model), does not predict the QG approximation well. A modified Lehnert number which includes a measure of the equatorial asymmetry and the local length scale comes out as a better indicator:

$$\lambda_m = \frac{|\widetilde{B}|}{\Omega\sqrt{\mu\rho}d}, \tag{4.35}$$

where $|\widetilde{B}|$ is the volume weighted strength of the asymmetric part of the background field,

$$|\widetilde{B}| = \frac{\Delta\langle B_s^2\rangle}{\sqrt{\langle B_s^2\rangle}}, \tag{4.36}$$

where $\langle\cdots\rangle = V^{-1}\iiint\cdots dV$, and $\Delta\langle B_s^2\rangle$ is the difference between the northern and the southern hemisphere. We find the transition to non-QG flow to be $\lambda_m \sim 0.02$, see Table 4.1.

When the QG assumption is valid, we find weak reflection at TC (all cases have $d \le 0.2$). One example is shown in Figure 4.10. We notice a time delay as well as an amplitude difference for the propagation of TW in the two hemispheres inside TC, see Figure fig:7. Although most simulations run at $P_m = \nu/\eta = 1$, we also repeated a few TW simulations at lower values of P_m down to 10^{-3}. We still see a hemispherical difference inside TC and weak reflection outside TC, albeit with

no.	λ_m ($\times 10^{-3}$)	QG?
1	208.3	n
2	2.636	y
11	4.851	y
14	6.471	y
22	28.88	n
23	32.19	n
24	14.35	y†
25	5.787	y
26	6.511	y
30	2.713	y
31	31.71	n
32	2.713	y
33	2.713	y
34	7.176	y
35	3.391	y

Table 4.1: Modified Lehnert number and (yes/no) correspondence to the QG approximation as measured by z invariance of the u_ϕ component. †: no.24 is a borderline case where there is a weak wave signal propagating along z direction in u_ϕ.

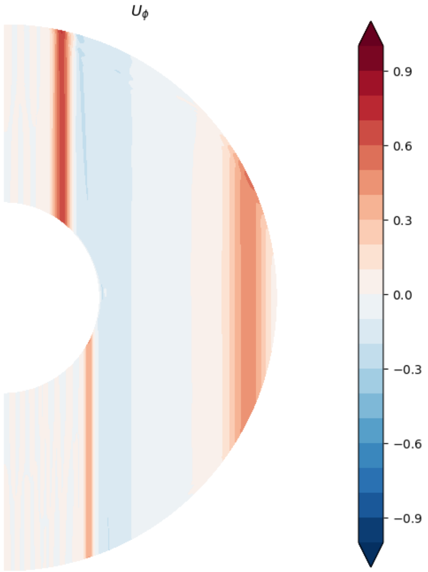

Figure 4.10: The u_ϕ profile at $t = 1350$, run no.25 with $(C_2, C_3) = (4.79 \times 10^{-4}, 3.72 \times 10^{-4})$. When the backgroud field has equatorial asymmetry and the QG assumption is valid, we see the hemispherical difference of TW inside TC, and weak reflection outside TC.

a weaker signature. However, because TW is much more diffusive at a lower P_m, the transient waves at the edge of the outer core and at the equator are no longer visible.

4.6.4 Conclusion

As proposed for the deliverable R-H. 4, we tested a forward model in a spherical shell using a particular type of QG flow that couples the fluctuation of the core flow with the background magnetic field $\boldsymbol{B}$. We have tested three cases with equatorially symmetric $\boldsymbol{B}$, equatorially anti-symmetric $\boldsymbol{B}$ and equatorially asymmetric $\boldsymbol{B}$. Regardless of the case, no strong reflection is seen outside TC. Therefore, these 3D numerical simulations do not support the hypothesis that the observed outwardly propagating TW is due to strong reflection at TC. We also find that transient waves can accommodate the continuous boundary condition for the magnetic field and the discontinuity in TW.

Inside TC, we notice a hemispherical difference in both wave speed and the amplitude of TW that is affected by the equatorial asymmetry of the background field. Additionally, such hemispherical difference is not strongly influenced by the magnetic Prandtl number P_m, so we can reasonably expect some difference in

TW to remain even at Earth's core-like values. However, since the inferred high-latitude jets have a distinct pattern, future studies may be needed to verify whether the velocity difference of TW we see here are still applicable to other types of QG flows .

Among these numerical simulations, we also found the transition point in terms of the modified Lehnert number λ_m which will break the QG assumption. Given that TW has been observed inside the core using inverse field models, our study suggests an upper bound on the amount of equatorial asymmetry inside the large-scale geomagnetic field. Note that our study is limited to an axisymmetric background field with the first non-zero symmetric and antisymmetric mode in B_s. Computationally more intensive simulations are probably required if we want to match B_s with the known power spectra of the geomagnetic field.

Bibliography

Chen L, Livermore PW, Jault D (in prep.) The effect of equatorially asymmetric background field on the torsional wave propagation in the Earth's core

Cox GA, Livermore PW, Mound JE (2013) Forward models of torsional waves: dispersion and geometric effects. Geophysical Journal International 196(3):1311–1329

Elsasser WM (1946) Induction effects in terrestrial magnetism part i. theory. Phys Rev 69:106–116

Finlay CC, Kloss C, Olsen N, Hammer MD, Tøffner-Clausen L, Grayver A, Kuvshinov A (2020) The chaos-7 geomagnetic field model and observed changes in the south atlantic anomaly. Earth, Planets and Space 72(1):1–31

Gillet N, Jault D, Canet E, Fournier A (2010) Fast torsional waves and strong magnetic field within the Earth's core. Nature 465(7294):74

Gillet N, Jault D, Finlay C (2015) Planetary gyre, time-dependent eddies, torsional waves, and equatorial jets at the earth's core surface. Journal of Geophysical Research: Solid Earth 120(6):3991–4013

Jault D, Finlay CC (2015) Waves in the core and mechanical core-mantle interactions. In: Schubert G, Olson P (eds) Treatise on Geophysics, Core Dynamics, 2nd edition, vol 8, Elsevier, Oxford, chap 8.09, pp 225–244

Schaeffer N, Jault D (2016) Electrical conductivity of the lowermost mantle explains absorption of core torsional waves at the equator. Geophysical Research Letters 43(10):4922–4928

Schaeffer N, Jault D, Cardin P, Drouard M (2012) On the reflection of alfvén waves and its implication for earth's core modelling. Geophys J Int 191(2):508–516

no.	P_m	η_g/η	η_m/η	λ ($\times 10^{-3}$)	d	$C_2, C_3(\times 10^{-3})$	C_2/C_3	s_0	QG?
1	1	1	0	54.0	0.05	19.17, 13.32	1.44	0.5	n
2	1	1	0	0.609	0.05	0.17, 0.17	0.99	0.5	y
5	1	1	0	7.57	0.05	6, 0	∞	0.4	y
6	1	1	0	7.57	0.01	6, 0	∞	0.4	y
8	1	1	0	17.9	0.15	0, 8	0	0.5	y
9	1	1	0	35.8	0.01	0, 16	0	0.5	n
10	1	1	0	4.48	0.01	0, 2	0	0.5	n
11	1	1	0	1.22	0.05	0.15, 0.46	0.33	0.5	y
13	1	1	0	17.9	0.01	0, 8	0	0.2	n
14	1	1	0	7.75	0.01	6, 0.08	75	0.4	y
18	1	1	0	4.48	0.02	0, 2.0	0	0.4	y
19	1	1	0	2.69	0.01	0, 1.2	0	0.4	y
22	1	1	0	2.55	0.02	0.6, 0.8	0.75	0.5	n
23	1	1	0	5.58	0.02	3, 0.8	3.75	0.5	n
24	1	1	0	1.98	0.02	0.15, 0.8	0.19	0.5	y
25	1	1	0	1.44	0.05	0.48, 0.37	1.29	0.5	y
26	1	1	0	0.675	0.02	0.24, 0.17	1.44	0.5	y
28	0.04	1	3.13×10^{-5}	1.89	0.05	1.5, 0	∞	0.5	y
30	1	1	0	0.681	0.05	0.23, 0.17	1.32	0.5	y
31	1	1	0	3.68	0.02	1.5, 0.8	1.88	0.5	n
32	0.01	1	0	0.681	0.05	0.23, 0.17	1.32	0.5	y
33	10^{-3}	1	0	0.681	0.05	0.23, 0.17	1.32	0.5	y
34	10^{-3}	1	0	0.990	0.02	0.075, 0.4	0.19	0.5	y
35	1	1	0	0.681	0.2	1.15, 0.87	1.32	0.5	y
36	0.04	1	10^{3}	0.681	0.2	1.15, 0.87	1.32	0.5	y

Table 4.2: Parameters for the 3D simulations. $\Omega = 1$, $\sqrt{\mu\rho} = 1$, $\lambda = |B|/(\Omega\sqrt{\mu\rho}L)$ is the Lehnert numer, $\nu = 10^{-8}$, $P_m = \nu/\eta$ is the magnetic Prandtl number, η_g is the magnetic diffusivity of the inner core, and η_m is the magntic diffusivity of the mantle. For run no.1 we use a prescribed non-zero initial b_ϕ, run no.5-6 start with $b_\phi = -u_\phi$, the rest starts with $b_\phi = 0$.

Teed RJ, Jones CA, Tobias SM (2018) Torsional waves driven by convection and jets in Earth‚Äôs liquid core. Geophysical Journal International 216(1):123–129

Chapter 5

Scientific roadmap for the future

4DEarth_Swarm_Core ESA project deliverable R-I.1

P. Livermore[1], N. Gillet[2] and C. C. Finlay[3]
[1] University of Leeds, [2] ISTerre, [3] DTU Space

The main objective of the 'Swarm 4D Earth core' project, started in September 2019, was to further the understanding of rapid (interannual) changes in the geomagnetic field, as probed by the Swarm mission. During the project we have achieved many important breakthroughs on this topic. Here we outline the future challenges in satellite geomagnetism, focusing in particular where we can build on our recent advances.

5.1 Summary of scientific advances

Before setting out our vision for the future, we briefly recall the important advances achieved through Swarm 4D Earth core. Sudden changes in the rate of change of the geomagnetic field (or 'jerks', see Mandea et al, 2010, for a review) had been first detected some 50 years ago in ground-based records. Over the satellite era they have been associated with pulses in the second time derivative of the field or 'secular acceleration' (Chulliat and Maus, 2014; Finlay et al, 2016). Prior to our project, these dynamics had largely remained unexplained. The work carried out by our consortium has allowed us to design a general framework that provides a physical understanding of rapid geomagnetic field changes. One of the key advances which underpinned this new understanding was the '71%-path' dynamo simulation run at extreme parameters (Aubert and Gillet, 2021), which showed many occurrences of magnetic acceleration events (see the catalog provided with Task E). An analysis of these events showed common signatures, and because the events were computationally simulated, for the first time we were able to investigate in-depth their controlling physics, for example, by assessing the relative importance of advection by the flow and wave propagation (Aubert et al, 2022). In parallel, a new analysis of recent geomagnetic data along with new eigenmode computational tools have made possible the discovery of QG MC waves with interannual periods in the geomagnetic signal recorded by Swarm and earlier satellites. On the large length-scales that are accessible with magnetic records ($\sim$ 800 km at the core surface), MC waves were previously believed to occur on centennial and longer periods (Hide, 1966). However, the eigenmode study by Gerick et al (2021) shows that QG MC modes do also exist on interannual periods, with a magnetic signature strongest close to the equator. Such a mode was detected, with period 7 yr, in core surface flows inverted from satellite magnetic data (Gillet et al, 2022). These present stronger patterns in the equatorial belt (of amplitude up to 5 km/yr), and travel westward at the equator, at a phase speed 1500 km/yr. This revised understanding of rapid core dynamics paves the way to a deterministic modelling of subdecadal geomagnetic field changes.

5.2 Using rapid dynamics to probe the basic state of the core

Despite the many recent advances in constructing observation-based models based on measurements of the geomagnetic field from space, there remains the fundamental physical limitation that these models do not allow us to directly image the geomagnetic field inside the Earth's fluid core, but only the large-scale field external to the core. Knowledge of the complete state of the core: the structure of the internal magnetic field, the pattern of core convection and the distribution of temperature (or light element) that drives motion in the fluid is crucial to a full understanding of the geodynamo. Our improved knowledge of the rapid time dynamics of the field external to the core provides a new opportunity to probe the basic state of the geodynamo. Assuming that the core dynamics is separable into slow (e.g. convection on centennial timescales) and fast dynamics (on interannual timescales, e.g. waves), then observations of the changing geomagnetic field over the fast timescale then provides constraints on the quasi-steady state that the waves ride upon. Below we make several specific suggestions to use Swarm observations of sub-decadal core field variations to obtain the structure of magnetic field and fluid flow within the core, which we suggest to be undertaken in parallel with advancing geomagnetic data algorithms and the improvement of physical understanding of rapid SV changes.

- **Geomagnetic data:** upgrade and extend the geomagnetic datasets, in a manner that is suited for incorporation into core dynamics analysis tools, including adapted information on data error covariances.

- **Understanding geomagnetic jerks:** despite the greatly improved understanding of the physics that describe geomagnetic jerks in numerical models, there remains a need to link this new understanding to observations of jerks from both ground and space. In particular, a detailed analysis is required in order to assess whether all rapid changes numerically computed so far share the same observational and dynamical properties, and how they compare with those recorded from ground or space. A characterization of jerks inside the Earth in terms of their causal mechanism would then be a significant advance. Because of our improved understanding of wave-driven jerk events, the signature and distribution of jerks might be used to constrain the background state of the core.

- **Waves in the core:** To date, the main information on the field deep in the core has been obtained through the detection of torsional Alfvén waves in magnetic observations (Gillet et al, 2010). This knowledge is however restricted to a one dimensional profile of the cylindrical radial component of magnetic field, B_s. In principle, the ability to detect QG MC modes will give access to a two dimensional map of the z-averaged r.m.s. B_s (as a function of s and ϕ). To more fully understand these exciting new modes and the constrains they provide studies are required to explore further their sensitivity to the background field with dedicated direct numerical simulations and eigenmode studies.

- **New 3D computational models of waves:** The scientific advances made possible through the 71% path model has shown the importance of high resolution forward models of the core. We suggest that through appropriately chosen forward models it will be possible to better characterize the propagation of QG MC and QG Alfvén waves.

- **Data assimilation:** with the possibility now of accurately computing forward models at Earth-like conditions, it may be possible to assimilate geomagnetic data into the model and thus create a dynamically consistent estimate of the background field within the core.

- **Improved core-flow reconstructions:** A deeper understanding from 3D computations of the magnetic field and flow structure near the edge of the core, relevant for the interannual dynamics, may lead to improved spatial constraints on the core flow recovery. Of course, not all the magnetic signal recorded by Swarm is accounted for by such dynamics; unresolved processes also account for a significant fraction of interannual field changes (about one half according to our recent work). These two sources of signal are covariant, and it may be that the small-scale components of QG MC modes are related to the unresolved subgrid-scale processes. A better understanding of this should allow a reduction in the uncertainties on core flows, and thus enhance the recovery of the field deep in the core.

- **Modelling the internal field and mantle conductivity:** the characteristics of QG MC mode propagation depends on the structure of the background magnetic field within the core and the conductivity of the mantle. Using geomagnetically observed QG MC waves, it may then be possible to infer certain averages of the magnetic field inside the core alongside the lower-mantle conductivity, thus constraining the structure of the internal field.

5.3 Changed deliverables in Swarm 4D Earth core

During the course of the project, several deliverables were altered because the research effort was better spent in following unpredicted and very promising avenues of investigation.

- The original deliverable R-H.4 was a report on the viability of a quasi-geostrophic model at high latitude, inside and across the tangent cylinder. This was designed to help explain the physics of the recently discovered high-latitude jet (Livermore et al, 2017). In place of this deliverable was a report on a new Bayesian method for jerk identification, which was important for constructing the catalogue of jerks. The original deliverable remains a promising angle of investigation, but in addition to originally proposed theoretical study, it might be useful to use the new 3D numerical simulations to better understand the nature of the quasi-geostrophic dynamics on the tangent cylinder.

- The original deliverable R-D.2 was a technical note on the feasibility of 3D reduced stochastic models. We had already begun a study on the use of the information carried by the horizontal component of the induction equation (in absence of magnetic boundary layers). This development was related to Task G (QG boundary conditions), and we foresee a potential for strongly increasing the amount of constraints when inverting core surface flows from magnetic data. We thus considered it as a new priority, and decided to change the initial plan for R-D.2, which now contains a technical note on ‘use of the horizontal induction for the kinematic recovery of surface core flows’. The original deliverable may still be useful in the future, although we do not foresee it as a major goal, at least as initially formulated – similar products may in principle be obtained in a sequential manner, starting first from an estimate of the core surface state, next coupled with a 3D estimate using the information carried by geodynamo simulations.

5.4 Long term vision

Over the next decade, the extension of satellite and ground-based geomagnetic datasets will provide increasingly powerful observational constraints on timescales relevant to core dynamics and the geodynamo. Crucial in this regard will be a continuation of the unique high quality magnetic data provided by the Swarm mission. Further improvements in spatial and temporal resolution are also on the horizon through presently proposed missions such as ‘NanoMagsat’ (Hulot, 2021) and ‘MacauSat’ (Zhang, 2021). In our opinion the key to fully exploiting this data and learning more about the deep Earth is parallel advances in numerical simulations of the geodynamo process, geomagnetic data assimilation schemes, simpler idealized models, and theory. By combining these tools with the unique observational constraints from high quality satellite magnetic data covering several decades we expect to obtain fundamental new insights on:

- **field changes on longer time-scales:** better understanding of rapid dynamics will improve our knowledge of the background state (for example the pattern of core-convection) and how it varies over centennial (or longer) timescales. Ultimately the pattern of convection underpins our knowledge of how the planetary-scale geodynamo operates.

- **Insights for better understanding the global Earth dynamics:** improved understanding of magnetic field change will allow us to better constrain the structure of the liquid core including the possible existence (or not) of a stratified layer, and the structure of the interface between the core and the overlying solid mantle (topography of the core surface, electrical conductivity of the lowermost mantle, etc.).

- **Prediction of the geomagnetic field:** present-day predictions of the geomagnetic field are limited by incomplete understanding of the geodynamo and the frequent (and currently unpredictable) occurrence of jerks. A better understanding of the processes governing rapid field change, along with geomagnetic jerks, may allow the accurate prediction of the geomagnetic field on interannual to centennial timescales.

- **Insights for better understanding other planetary bodies:** Earth is only one of the planets in our solar system with a magnetic field. Improved understanding of Earth will allow much better understanding of the general conditions that permit magnetic field generation. Because the structure of a planetary magnetic field is an important constraint on its interior structure, these improvements in understanding will feed into the design of future missions in order to maximise scientific return.

Bibliography

Aubert J, Gillet N (2021) The interplay of fast waves and slow convection in geodynamo simulations nearing earth's core conditions. Geophys J Int DOI https://doi.org/10.1093/gji/ggab054

Aubert J, Livermore PW, Finlay CC, Fournier A, Gillet N (2022) A taxonomy of simulated geomagnetic jerks

Chulliat A, Maus S (2014) Geomagnetic secular acceleration, jerks, and a localized standing wave at the core surface from 2000 to 2010. J Geophys Res: Solid Earth 119(3):1531–1543

Finlay CC, Olsen N, Kotsiaros S, Gillet N, Tøffner-Clausen L (2016) Recent geomagnetic secular variation from Swarm. Earth, Planets and Space 68(1):1–18

Gerick F, Jault D, Noir J (2021) Fast quasi-geostrophic magneto-coriolis modes in the earth's core. Geophys Res Lett p 2020GL090803

Gillet N, Jault D, Canet E, Fournier A (2010) Fast torsional waves and strong magnetic field within the Earth's core. Nature 465(7294):74

Gillet N, Gerick F, Jault D, Schwaiger T, Aubert J, Istas M (2022) Satellite magnetic data reveal interannual modes in earth's core

Hide R (1966) Free hydromagnetic oscillations of the earth's core and the theory of the geomagnetic secular variation. Phil Trans R Soc London Series A, Mathematical and Physical Sciences 259(1107):615–647

Hulot G (2021) The nanomagsat project

Livermore PW, Hollerbach R, Finlay CC (2017) An accelerating high-latitude jet in Earth's core. Nature Geoscience 10(1):62–68

Mandea M, Holme R, Pais A, Pinheiro K, Jackson A, Verbanac G (2010) Geomagnetic jerks: rapid core field variations and core dynamics. Space science reviews 155(1):147–175

Zhang K (2021) A high-precision and highly-elliptical-orbit geomagnetic constellation